

Spectroscopy and the Path to Laser Cooling of Zinc

Dissertation
zur
Erlangung des Doktorgrades (Dr. rer. nat.)
der
Mathematisch-Naturwissenschaftlichen Fakultät
der
Rheinischen Friedrich-Wilhelms-Universität Bonn

von
David Röser
aus
Bonn

Bonn, 2024

Angefertigt mit Genehmigung der Mathematisch-Naturwissenschaftlichen Fakultät der Rheinischen
Friedrich-Wilhelms-Universität Bonn

Gutachter/Betreuer: Prof. Dr. Simon Stellmer
Gutachterin: PD Dr. Elisabeth Soergel
Tag der Promotion: 05.03.2025
Erscheinungsjahr: 2025

Abstract

To enable laser cooling of zinc, a deep UV laser system for the main cooling transition at 214 nm has been developed. The system relies on frequency-quadrupling a titanium-sapphire laser in two consecutive frequency-doubling resonators, delivering up to 10 mW power from 4.3 W at the fundamental frequency. For interrogating the clock transition at 310 nm, a laser system has been constructed by frequency-quintupling of 1548 nm light, taking advantage of the possibility to distribute the clock signal through the existing telecom fiber networks. The system relies on one frequency-doubling and two sum frequency generation processes, eventually yielding 0.5 mW UV light.

A spectroscopic characterization of the 214 nm transition has been performed in collaboration with the *Cold Molecule Group* at the *Fritz-Haber-Institut* in Berlin. A beam of zinc atoms, cooled by collisions with He at 3 K, is excited with linearly polarized laser light whose frequency is stabilized to a stable ULE reference cavity. By measuring the fluorescence, isotope shift measurements on all stable isotopes have been performed improving literature values by more than one order of magnitude. Furthermore, the absolute frequencies of ^{64}Zn and the isotopic center-of-mass have been determined using a wavemeter. The hyperfine structure coefficients A and B of ^{67}Zn , the only isotope with non-zero nuclear spin, have been determined considering the lineshape modification due to quantum interference. A King plot analysis exhibits the expected linearity proving consistency with literature values on the 308 nm line.

For establishing a high-resolution spectroscopy setup in Bonn, isotope shifts on the 423 nm transition of $^{40,42,44,48}\text{Ca}$ have been measured with saturated absorption spectroscopy, improving literature values by a factor of 3. A lock-in technique is employed by sinusoidally modulating the intensity of the pump beam. Possible sources of systematic errors, *e.g.*, buffer gas collisions and radiation pressure-induced distortions of the velocity distribution, are analyzed and either addressed in the experimental design or corrected for during data analysis. For narrow lines, self-collisions appear additionally so that future spectroscopy on intercombination lines should be performed on atomic beams. An optical setup including a ULE cavity to stabilize the laser frequency for the zinc intercombination line at 308 nm has been developed.

For future demonstration of the first laser cooling on zinc, an experimental setup for a magneto-optical trap has been constructed. The design includes the vacuum system, a thermal atom source and the coil system providing the magnetic field gradient. For clock experiments, the “magic” wavelength, at which the AC Stark shift cancels for the clock transition, is calculated to be 410 nm, at which confinement in the sideband-resolved Lamb-Dicke regime with suitable trap lifetimes appears possible.

List of Publications

This thesis contains two chapters based on articles published in a peer-reviewed journal. They are considered as the main results and their citation reads:

David Röser, J. Eduardo Padilla-Castillo, Ben Ohayon, Russell Thomas, Stefan Truppe, Gerard Meijer, Simon Stellmer, and Sid C. Wright,

Hyperfine structure and isotope shifts of the $(4s^2) ^1S_0 \rightarrow (4s4p) ^1P_1$ transition in atomic zinc,
Phys. Rev. A **109** (2024) 012806.

DOI: <https://doi.org/10.1103/PhysRevA.109.012806>

David Röser, Lukas Möller, Hans Keßler, and Simon Stellmer

Isotope-shift measurement of the 423-nm line in Ca,
Phys. Rev. A **110** (2024) 032809.

DOI: <https://doi.org/10.1103/PhysRevA.110.032809>

Furthermore, the author of this thesis contributed to one more publication. This publication is not considered for cumulative writing, as it contains preparatory work for future experiments. Its content is briefly summarized, including a description of the author's contribution, in the respective section.

Maya Büki, David Röser, and Simon Stellmer,

Frequency-quintupled laser at 308 nm for atomic physics applications,
Appl. Opt. **60** (2021), 9915-9918.

DOI: <https://doi.org/10.1364/AO.438793>

Contents

1	Introduction	1
2	Zinc as a possible element for future frequency standards	5
2.1	Frequency standards	5
2.2	Isotopic, electronic, and chemical properties of zinc	6
2.2.1	Level scheme	7
2.2.2	Vapor pressure and chemical reactions	7
2.3	Potential of zinc in frequency standards	9
2.3.1	Frequency and linewidth for fermionic and bosonic isotopes	9
2.3.2	Blackbody radiation shift	10
2.3.3	Clock light distribution via fiber network	12
2.4	Laser systems	12
2.4.1	214-nm laser	13
2.4.2	308-nm laser	17
2.4.3	310-nm clock laser	17
3	Nuclear features in atomic spectra	21
3.1	Origin and contributions to isotope shifts	21
3.1.1	Mass shift	21
3.1.2	Field shift	22
3.2	King plots	23
3.3	Hyperfine structure and quantum interference	24
3.3.1	Hyperfine structure	24
3.3.2	Quantum interference	25
4	Hyperfine structure and isotope shifts of the $^1S_0 \rightarrow ^1P_1$ transition in zinc	29
4.1	Atomic beam preparation and spectroscopy	30
4.2	UV laser system and Pound-Drever-Hall lock	31
4.3	Measurements and results	33
5	Isotope shift measurement of the $^1S_0 \rightarrow ^1P_1$ transition in calcium	37
5.1	Experimental apparatus	38
5.2	Measurements	40
5.3	Results	42

6	Outlook: Spectroscopy of the $^1S_0 \rightarrow ^3P_1$ transition and towards laser cooling of zinc	45
6.1	Hyperfine structure and isotope shifts on the $^1S_0 \rightarrow ^3P_1$ transition in zinc	45
6.1.1	Design and construction of a frequency reference cavity	46
6.1.2	Fluorescence spectroscopy setup	50
6.2	Towards magneto-optical trapping of zinc	52
6.2.1	Vacuum System	52
6.2.2	Atom source and dump	54
6.2.3	Magneto-optical trap and magnetic field coils	54
6.3	Calculation of the magic wavelength	57
7	Conclusion	59
A	Publication: Hyperfine structure and isotope shifts of the $(4s^2) ^1S_0 \rightarrow (4s4p) ^1P_1$ transition in atomic zinc	61
A.1	I. Introduction	62
A.2	II. Experimental Setup	62
A.3	III. Analysis of Spectral Line Shapes	64
A.4	IV. Results	65
A.5	V. Discussion	67
A.6	VI. Summary and Outlook	68
B	Publication: Isotope shift measurement of the 423-nm transition in neutral Ca	71
B.1	I. Introduction	72
B.2	II. Experimental Apparatus	72
B.3	III. Measurements	74
B.4	IV. Conclusions and Outlook	76
	Bibliography	81
	List of Figures	99
	List of Tables	103
	Acknowledgements	105

Introduction

Ever since ancient times, timekeeping has been of great importance for human civilization. While the day-night cycle structures people's daily life, astronomical observations have guided agriculture and religious habits or rituals within a year.

Since the second half of the 20th century, timekeeping has revolutionized, as atomic cesium clocks have been invented, offering exceptional precision [1]. The international definition of the second is currently based on the unperturbed ground state hyperfine transition in ^{133}Cs , whose frequency at around 9.2 GHz is measured with microwave spectroscopy [2]. However, the progress in metrology led to optical clocks based on atoms confined in 'magic' lattices or ions kept in Paul traps. These types of clocks offer a fractional precision at the 10^{-18} level, far beyond any cesium clock [3, 4]. This low uncertainty makes time the quantity in nature that can be determined most precisely [5].

Today, atomic clocks are a key component in everybody's daily life, *e.g.* in the synchronization of the telecommunication system, or global navigation satellite systems, such as the global positioning system (GPS). These systems operate on accurately measuring the time a signal takes to be transmitted from an emitter at a known location to a receiver. Satellite based systems provide information about the receiver's location and enable navigation independently of the position on Earth [6].

Beyond navigation and with successful realization of transportability, atomic optical clocks have become a valuable tool in geodesy. By determining the gravitational red-shift in the clock transition with transportable optical clocks, the Earth's gravitational potential can be characterized. Thus, clock-based measurements provide additional insights into the characterization of Earth's surface height [7, 8]. Improvements on the application of clocks go hand in hand with enhanced precision and accuracy.

The lowest ever reported uncertainty of a clock has been reported by Ref. [3], in a lattice clock operating on strontium. Their limiting contribution to the uncertainty stems from the frequency shift due to ambient blackbody radiation. As zinc offers a reduced sensitivity to blackbody radiation shifts [9], it has emerged as a promising candidate for future optical lattice clocks [10], as it might overcome the current limitation. Hence, a zinc clock might operate with competitive uncertainty one day (Section 2.3.2). A further advantage is that laser light for interrogation of the clock transition can be derived as the fifth harmonic of a telecom wavelength laser. As its frequency lies right within the telecom c band, the distribution of the clock signal via fiber links might be possible without the need for a frequency comb (Section 2.3.3). While the vast majority of group 2 and 12 elements have been used in cold atom or ion experiments [3, 11–18], zinc has remained rather unexplored

experimentally. A possible explanation might be that important optical transitions lie within the UV range (see Section 2.2.1), significantly complicating laser technology, and lasers with suitable powers may not be commercially available.

Over the past decades, the advancement in spectroscopy led to a significant increase of its spectral resolution. While early discharge experiments were limited by the resolution of the spectrometer on the 10 MHz scale [19, 20], modern laser spectroscopy can locate a resonance frequency typically to a few percent of the natural linewidth. State-of-the-art experiments on clock transitions even reach uncertainties at the Hz level in isotope shift and hyperfine structure measurements [21–23]. The term isotope shift refers to the variation in energy of atomic levels within different isotopes, while the hyperfine structure splitting arises from the coupling of angular momenta between the atomic nucleus and its surrounding electrons [24]. The measurement of isotope shifts and hyperfine structure provides a valuable tool for characterizing the nuclear structure and gives insights into the nuclear size and shape, as discussed in Chapter 3 [22, 23, 25, 26]. They may also be used to explore potential physics beyond the Standard Model, such as temporal variation in fundamental constants [27], a possible new gauge boson [26, 28], CPT violation [29] or violations of local Lorentz invariance [29, 30].

This thesis intends to provide groundwork for precision spectroscopy and laser cooling of zinc atoms. In the course of this work, two UV laser systems have been developed, one for driving the main cooling transition of zinc at 214 nm and one for interrogation of the clock transition at 310 nm. Both their performance is confirmed by absorption spectroscopy [31–33]. These laser systems are presented in Sections 2.4.1 and 2.4.3, respectively.

In collaboration with the *Cold Molecule Group* at the *Fritz-Haber-Institut* in Berlin, laser spectroscopy on the 214 nm transition has been performed, measuring fluorescence on a cryogenic buffer gas cooled atomic beam. During the campaign, the hyperfine structure coefficients A and B for ^{67}Zn , the only Zn isotope with nuclear spin, have been determined, taking into account quantum interference in the lineshape model. Referencing the laser frequency to a stable ULE cavity, isotope shifts are measured with a precision improving literature values by more than one order of magnitude. The absolute frequencies of the ^{64}Zn transition and the isotopic center-of-mass have been determined by a wavemeter. The results are presented in Chapter 4 and published in the article reprinted in Appendix A [34].

To further support high-resolution spectroscopic experiments in Bonn, a setup for saturated absorption spectroscopy was constructed. This setup incorporates lock-in detection to achieve a higher signal-to-noise ratio and a magnetic field compensation over the entire vapor cell. Systematic shifts and lineshape changes, including the Doppler shift, buffer gas collisions, light pressure induced velocity distribution modification, and power dependent shifts have been studied and corrected for. Hence, the isotope shifts for $^{40,42,44,48}\text{Ca}$ were measured with a precision at the parts-per-thousand level relative to the natural linewidth, representing a threefold improvement over existing values in the literature. The measurements are presented in Chapter 5 and published in the article reprinted in Appendix B [35].

Based on the gained experience, it appears more reasonable to perform spectroscopy on kHz-linewidth transitions by fluorescence measurements of atomic beams. This technique benefits from a lower atom density, the absence of buffer gas and a significantly lower shot noise limit [36]. An experimental setup has been designed and a measurement plan has been developed, applying this technique to the 397.6 nm transition in zinc. The setup includes a beam source and an experiment chamber, based on an estimation of the magnitude of the expected signal. The parts and the calculation are introduced in Section 6.1.2. To provide a sufficiently narrow laser linewidth over the measurement

time, a frequency reference cavity has been constructed and the support points have been modeled to ensure minimal vibration sensitivity. However, the resonator's temperature stability has to be improved in the future, as it is discussed in Section 6.1.1.

As spectroscopy on transitions with linewidths below the Hz level is typically performed in cold atom experiments [37], a setup for magneto-optical trapping of zinc has been constructed. Its design is shown and discussed in Section 6.2. With this setup, the laser cooling and magneto-optical trapping of zinc could be possible, as soon as sufficient laser power is available at 214 nm. To the best of our knowledge, this would be the first demonstration of laser cooling of zinc. The setup includes the vacuum system (Section 6.2.1), an atom source and dump (Section 6.2.2) as well as an Anti-Helmholtz coil pair (Section 6.2.3) providing the magnetic field gradient necessary to operate the trap. Further, looking ahead, the magic wavelength for a lattice of cooled zinc atoms is calculated and its applicability is shown for the operation of a zinc lattice clock in Section 6.3.

Zinc as a possible element for future frequency standards

This chapter introduces zinc as a potential candidate for frequency standards. First, an overview of optical frequency standards is given. Afterwards, electronic, isotopic and chemical properties of zinc are presented and its level scheme is discussed. The chapter is concluded by discussing benefits and drawbacks of using zinc for clock applications and metrology and introducing the laser systems used throughout this work.

2.1 Frequency standards

In general, clocks or frequency standards consist of a stable oscillator, whose oscillations are counted. While early clocks utilized the Earth's rotation around itself, the development has progressed over centuries to mechanical oscillators, such as pendulums and quartz crystals, and eventually to microwave and visible light fields. The so-called optical frequency standards feature three main components:

1. Local oscillator: The oscillator is given by the light field of the clock laser. Its short-term stability can be achieved by locking the laser frequency to a resonance of a high finesse ultra-low expansion (ULE) cavity. By doing so, linewidths of less than 10 mHz have been achieved on a time period of 170 s [38]. The short-term stability is a prerequisite for precisely probing the narrow atomic clock transitions.
2. Long-term stable reference: As the resonance frequency of the cavity might drift over time, a long-term stable reference is needed. By agreement on a common reference, clocks operate on the same frequency or on frequencies comparable to each other. This reference can be provided by clock transitions in neutral atoms or ions with linewidths between the nanohertz range ($^2S_{1/2} \rightarrow ^2F_{7/2}$ in Yb^+ [39]) and several 100 Hz ($^1S_0 \rightarrow ^3P_1$ in Ca [40]). A clock instability measure is the Allan deviation [41–43], which can be expressed for Ramsey interrogation [44, 45] as

$$\sigma(\tau) = \frac{1}{2\pi \nu_0 \sqrt{NT_m \tau}} \quad (2.1)$$

with τ being the averaging time, ν_0 the clock transition frequency, N the number of probed atoms and T_m the free-precession time. It should be noted that Eq. (2.1) is derived by assuming that $\pi/2$ -pulse durations are short compared to T_m , the state detection efficiency is on the order of unity, relaxation times are long compared to T_m , the time for state preparation and dead times are negligible and that the noise is dominated by quantum projection noise [5]. As evident from Eq. (2.1), the clock operation benefits from a high number of atoms as \sqrt{N} , a narrow clock transition linewidth as $T_m \approx 1/(2\pi\Delta\nu)$ and a large clock transition frequency ν_0 .

3. Counting mechanism: For operating a frequency standard, the clock laser has to be referenced to the definition of the SI unit system. This can be realized with the means of a high-bandwidth frequency comb, as the frequency of the clock laser can be related through the comb mode spacing to a cesium clock directly or a different atomic transition that has been measured against the SI definition. A further possibility is to compare the clock laser to multiple comb modes and observe their beating [46].

One approach for state-of-the-art frequency standards is the lattice clock, in which atoms are captured and cooled in magneto-optical traps (MOTs) and held in an optical lattice. For capturing a large number of atoms, a strong cooling transition is beneficial to maximize the number of scattered photons. The drawback is a high Doppler temperature that can be overcome by loading the atoms into a second stage MOT. This MOT is based on narrow transitions with sub-100 kHz-linewidth. Typically, the minimal temperature is limited by the atomic recoil, as the recoil temperature is larger than the Doppler temperature. Subsequently, the atoms are loaded into an optical lattice, before the clock transition is probed [46].

For relative frequency uncertainties on the 10^{-18} scale, as it has been reached with ^{88}Sr lattice clocks [3, 47], multiple systematic line shifting effects have to be taken into account, *e.g.*, Zeeman-, Stark-, blackbody radiation- and collisional shifts, as well as Doppler- and gravitational effects [3, 5].

2.2 Isotopic, electronic, and chemical properties of zinc

Like cadmium (Cd), mercury (Hg), and copernicium (Cn), zinc (Zn) belongs to the element group 12 of the periodic table. It features an atomic number of 30 and a mass of (65.38 ± 0.02) u [48]. In total, there are five different stable isotopes, ^{64}Zn , ^{66}Zn , ^{67}Zn , ^{68}Zn , and ^{70}Zn , whose respective masses and abundances are given in Table 2.1. All even-mass isotopes have a nuclear spin of $F = 0$, resulting in an absence of hyperfine structure, while for the only fermionic isotope $F = 5/2$ holds.

Table 2.1: Atomic mass [49], mass excess and abundance of the different Zn isotopes [50]. The mass excess gives the difference between the actual mass of the isotope with mass number i and $i \cdot 1$ u.

isotope	mass [μu]	mass excess [keV/c^2]	natural abundance [%]	nuclear spin
^{64}Zn	$63\,929\,141.8 \pm 0.7$	$-66\,004.0 \pm 0.6$	49.1775	0
^{66}Zn	$65\,926\,033.6 \pm 0.8$	$-68\,899.2 \pm 0.7$	27.7398	0
^{67}Zn	$66\,927\,127.4 \pm 0.8$	$-67\,880.4 \pm 0.8$	4.0416	5/2
^{68}Zn	$67\,924\,844.2 \pm 0.8$	$-70\,007.2 \pm 0.8$	18.4563	0
^{70}Zn	$69\,925\,319.2 \pm 2.1$	$-69\,564.7 \pm 1.9$	0.6110	0

2.2.1 Level scheme

Similar to alkaline-earth metals, Zn possesses two valent s-electrons, but the underlying 3*d*-shell is completely filled, as in other group 12 elements. This results in a $4s^2\ ^1S_0$ ground state and an alkaline-earth-like level scheme which is depicted in Fig. 2.1 and is comparable to the one of Cd. The first excited states are the $4s4p\ ^3P_J$, $J = 0, 1, 2$, spin triplet states and the $4s4p\ ^1P_1$ singlet state.

The wavelength of the singlet transition is 214 nm, placing it in the deep UV range. While pulsed lasers are commercially available, cw laser sources are limited to the milliwatt power range¹. To obtain several 100 mW power for laser cooling, the laser has to be self-built. Optics have to be made of KrF excimer grade fused silica² to withstand UV damage. The transition linewidth $\Delta\nu = \Gamma/(2\pi)$ is measured to be around 111 MHz during this work (see Chapter 4 and Appendix A). This large linewidth and the UV wavelength are ideal for capturing atoms and laser cooling applications, as it allows for high photon scattering rates and efficient momentum transfer to the atoms. However, the saturation intensity of approx. 1.5 W/cm^2 makes it difficult to saturate the transition. Hence, magneto-optical trapping requires precise power balancing between counterpropagating trapping beams. The Doppler temperature of 2.7 mK can be overcome by utilizing the intercombination line to the 3P_1 state of the spin triplet.

This line is at 308 nm and features a linewidth of $\Delta\nu = 4.7\text{ kHz}$ [10] and a saturation intensity of $27\ \mu\text{W/cm}^2$. A magneto-optical trap operating on this transition is limited by the recoil temperature of 3 μK . Furthermore, this line might be used for beam clocks with Ramsey-Bordé spectroscopy schemes [51, 52]. Here, high power lasers can be bought commercially and optics can be fabricated from standard UV fused silica.

The transition to the 3P_0 state is doubly forbidden. As it is a $J = 0 \rightarrow J = 0$ transition, the transition matrix element equals zero for the even-mass isotopes. In ^{67}Zn , the transition linewidth is calculated to be 2.5 mHz, as the electrons are affected by the magnetic field from the nucleus [10]. The magnetic field couples the 3P_0 to the 3P_1 state and causes a line mixing, through which the transition becomes weakly allowed [53]. By imposing this mixing with an external magnetic field, this transition may be used as a clock transition in lattice clocks [10], similarly to approaches with strontium [54]. Further, Fig. 2.1 shows excited states of the 1P_1 and 3P_1 transition, as this is relevant for the calculation of the magic wavelength, presented in Section 6.3.

2.2.2 Vapor pressure and chemical reactions

In comparison to alkaline-earth metals, zinc features a relatively low melting temperature of around $420\text{ }^\circ\text{C}$. Its vapor pressure curve below the melting point in vacuum is given by [10]

$$\log(P) = -6850/T - 0.755 \log(T) + 11.24, \quad (2.2)$$

where the pressure P is given in torr and the temperature T in K. The corresponding plot is shown in Fig. 2.2. As temperatures of up to $700\text{ }^\circ\text{C}$ can be reached with commercially available heating tapes and cartridges, high absorption vapor cells or high flux atom sources for cold atom experiments are technically easier to maintain than for, *e.g.*, strontium [56].

Zinc is chemically classified as medium reactive at room temperature. Its reaction with atmospheric

¹ *e.g.*, 15 mW from a Toptica DLC TA-FHG pro

² *e.g.*, Corning 7980 KrF, Suprasil 1 KrF or Suprasil 2 KrF

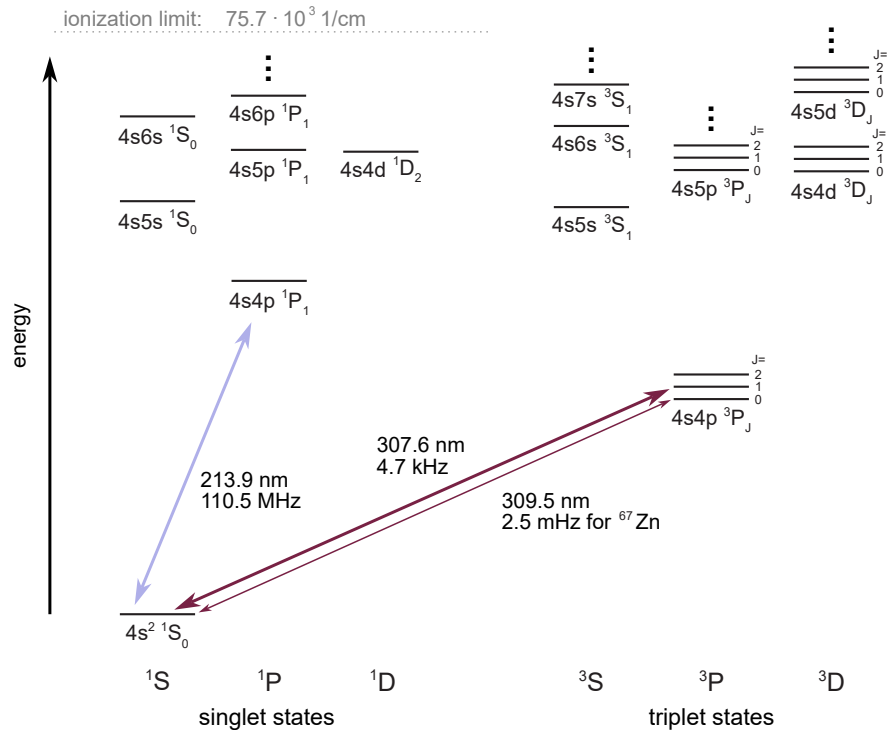


Figure 2.1: Level scheme for Zn. The transition wavelengths and linewidths in natural frequencies are given for the most relevant transitions [10, 34, 55]. Other transitions are used for calculating the magic wavelength (see Section 6.3).

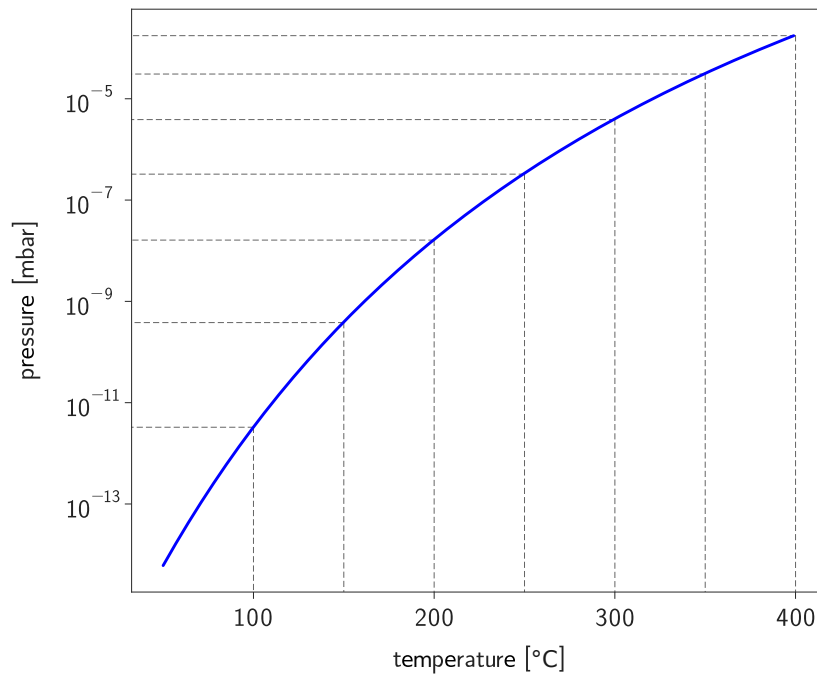
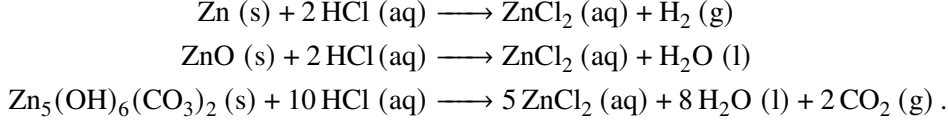


Figure 2.2: Vapor pressure curve for Zn. The underlying formula is given in Ref. [10].

CO₂ forms a passivating layer of Zn₅(OH)₆(CO₃)₂ protecting the zinc from oxidizing [57]. Reactions with H₂O typically happen at much higher temperature [58, 59]. Hence, zinc does not need to be stored under noble gas or nitrogen atmosphere.

Hydrochloric acid dissolves zinc as well as its oxide ZnO and Zn₅(OH)₆(CO₃)₂, leaving only aqueous and gaseous end products



These reactions can be exploited, *e.g.*, to remove Zn deposited on vacuum windows. However, small contamination can be wiped off with lens cleaning tissues and isopropanol.

2.3 Potential of zinc in frequency standards

In the following, factors influencing the performance of lattice clocks are discussed and Zn is introduced as a potential clock element. During the time of this work and to the very best of my knowledge, the best clock performance has been obtained by a Sr lattice clock [3]. Hence, these factors are compared for Zn and Sr.

2.3.1 Frequency and linewidth for fermionic and bosonic isotopes

As it is shown in Section 2.1, atomic references for frequency standards benefit from a large frequency and a narrow linewidth of the clock transition, as this lowers the Allan deviation. Comparing these quantities in fermionic isotopes, Zn with 2.5 mHz / 310 nm is on par with Sr, which features 1 mHz / 698 nm.

For bosonic isotopes, the clock transition cannot be probed without further difficulty. In Refs. [10, 60], different methods are introduced, which are briefly discussed in the following and illustrated in Fig. 2.3.

One way of partly allowing the clock transition is applying an external magnetic field, as the ³P₁ and the ³P₀ clock state are coupled by a magnetic dipole operator [53]. Thus, the ³P₁ state is mixed into the ³P₀ state [53]. For this process, four constants, α , β , κ and ξ are defined: $\alpha = \Omega_R / (\sqrt{I}B \cos(\Theta))$ describes the magnitude of the induced Rabi frequency Ω_R with respect to the clock light power I , the magnetic field amplitude B and the angle between light polarization and magnetic field Θ . Limiting factors may be the quadratic Zeeman shift and the light shift. The sensitivity to the quadratic Zeeman shift is described by $\beta = \Delta_B / B^2$, and $\kappa = \Delta_L / I$ describes the sensitivity to light shifts. Hence, the factor $\xi = \alpha / \sqrt{\beta\kappa}$ serves as an indication for the applicability for magnetic field induced spectroscopy, as it relates the obtained Rabi frequency to the induced shifts. Refs. [10, 53] calculate these coefficients for different elements including Zn and their results for Zn and Sr are given in Table 2.2. To obtain the same Rabi frequency as in Sr, the shifts in Zn are three times larger. Nevertheless, as bosonic clocks with 3×10^{-18} instability and 2×10^{-17} accuracy have been realized with Sr [54, 61], Zn is also a candidate for bosonic clocks at the instability level below the 10^{-17} level.

Table 2.2: Coefficients for magnetic field-induced spectroscopy [10].

Element	α $\left[\frac{\text{Hz}}{\text{T}\sqrt{\text{mW}/\text{cm}^2}} \right]$	β $\left[\frac{\text{MHz}}{\text{T}^2} \right]$	κ $\left[\frac{\text{mHz}}{\text{mW}/\text{cm}^2} \right]$	ξ
Zn	45.9	-22.9	10.4	0.094
Sr	198.0	-23.3	-18.0	0.300

As an alternative to magnetic field induced spectroscopy, a stimulated Raman adiabatic passage (STIRAP)³ might be used utilizing a dressing laser acting on the $^3\text{P}_0 \rightarrow ^1\text{P}_1$ and a probe laser acting on the $^1\text{S}_0 \rightarrow ^1\text{P}_1$ transition. When the detuning of the probe Δ_p is close to the detuning of the dressing field Δ_d , the electron can be excited to the clock state without populating the intermediate state [62]. For a desired line width of 0.1 mHz, Ref. [10] has calculated intensities of approx. 5.35 mW/cm² for the dressing laser and less than 1 pW/cm² for the probe laser. Using this excitation scheme, the largest influence on line shifts stems from the AC Stark shift of the dressing laser, approx. 11 mHz. This is more promising for Sr: To achieve a similar linewidth and excitation efficiency as in Sr, the AC Stark shift is one order of magnitude larger in Zn [62].

In lattice clocks, atoms are captured in optical lattices operating at an AC Stark shift compensating “magic” wavelength (see Section 6.3). In Ref. [60], it has been shown that a small circularly polarized part of the lattice light induces a second-order dipole-dipole mixing of the $^3\text{P}_1$ state into the $^3\text{P}_0$ state. It weakly allows the direct excitation of the clock state without the need of additional fields. The remaining Stark shift contribution is dominated by higher-order AC Stark shift terms proportional to the clock laser intensity $\kappa^{(1)}(\omega_c) \cdot I_c$ and the lattice laser intensity squared $\kappa^{(2)}(\omega_m) \cdot I_m^2$. Compared to Sr, their respective coefficients are one and two orders of magnitude lower and $\kappa^{(1)}(\omega_c)$ and $\kappa^{(2)}(\omega_m)$ possess opposite signs. The Rabi frequency depends linearly on the lattice-laser intensity multiplied with the square-root of the clock-laser intensity and the coefficient ζ . The values of the coefficients are shown in Table 2.3. In Zn, this excitation scheme suffers from the shift due to the lattice light: To obtain a similar Rabi frequency as in Sr, the Stark shift contribution is one order of magnitude larger.

In conclusion, there are multiple excitation schemes for the clock transition in bosonic Zn isotopes. The additional fields contribute to line shifts, which are larger compared to Sr. However, bosonic clocks in Zn might be achieved with relative uncertainties at the 10^{-17} level, but a more detailed investigation of the shifts and their uncertainties appears necessary.

2.3.2 Blackbody radiation shift

The largest line shift $\delta\nu_{\text{BBR}}$ and uncertainty contribution to Sr lattice clocks stems from ambient blackbody radiation (BBR), when the clock is operated at room temperature [3, 63, 64, and Refs. therein]. The leading order of the fractional shift can be expressed as

$$\frac{\delta\nu_{\text{BBR}}}{\nu_0} \propto \left(\frac{T}{300 \text{ K}} \right)^4, \quad (2.3)$$

³ In literature, this excitation scheme is also called a Λ electromagnetically induced transparency (EIT) scheme [10, 62].

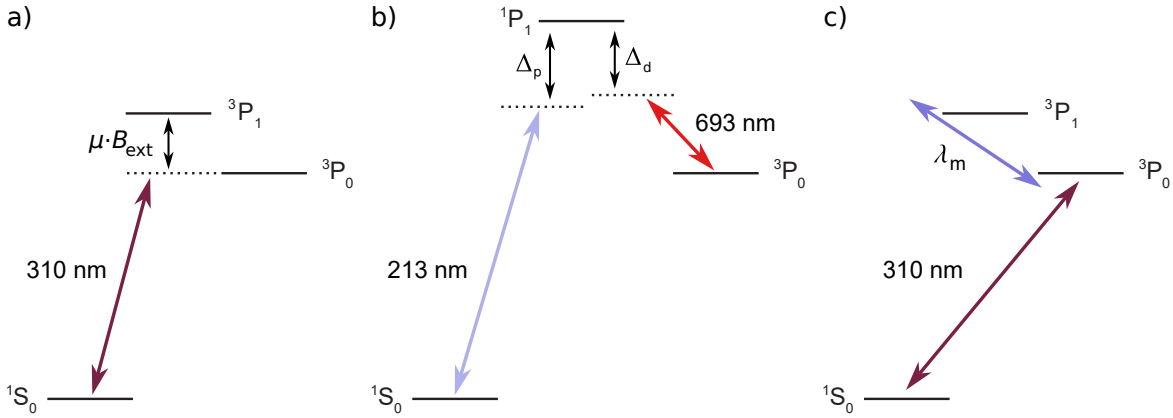


Figure 2.3: Different methods for populating the 3P_0 state in bosonic Zn isotopes. a) An external magnetic field B_{ext} is applied to couple the 3P_1 and 3P_0 states with a magnetic dipole interaction. Then the clock state might be directly excited. b) A STIRAP scheme is applied. If the Δ_p is in the vicinity of Δ_d , the population might be transferred into the 3P_0 state. c) A small portion of clock lattice light at the “magic” wavelength λ_m can be circularly polarized. This couples the 3P_1 and 3P_0 states thus allowing direct excitation of the 3P_0 state.

Table 2.3: Second order clock laser-induced AC Stark shift coefficient $\kappa^{(1)}(\omega_c)$, fourth order lattice laser-induced AC Stark shift coefficient $\kappa^{(2)}(\omega_m)$ [60] and the sensitivity of the Rabi frequency to the clock- and lattice laser intensity for Zn and Sr.

Element	$\kappa^{(1)}(\omega_c)$ $\left[\frac{\text{mHz}}{\text{mW/cm}^2} \right]$	$\kappa^{(2)}(\omega_m)$ $\left[\frac{\text{Hz}}{(\text{MW/cm}^2)^2} \right]$	$ \zeta $ $\left[\frac{\text{mHz}}{(\text{MW/cm}^2)\sqrt{\text{mW/cm}^2}} \right]$
Zn	0.816	-6.96	15.2
Sr	-44.2	-61.5	176.9

where T is the temperature of the thermal bath and the proportionality constant depends on the atomic species [9]. For the current Sr lattice clock with the lowest uncertainty [3], the shift is a factor of approx. 60 larger than the second largest term arising from the second-order Zeeman shift. The uncertainty contribution is a factor of approx. two larger than the second largest term, namely the lattice light shift. For further improvement, either β has to be determined more precisely or the temperature of the thermal bath has to be reduced, *e.g.*, in a cryostat. However, fluctuations of the ambient temperature might still limit the clock operation. Hence, atoms or ions with lower sensitivity on BBR shifts are preferable. Ref. [9] has calculated the BBR shift for Zn at room temperature. The value for Zn is shown in Table 2.4 together with the values of Sr and Hg, as Hg is the lattice clock candidate with the lowest BBR shift known so far. Compared to Sr, the fractional BBR shift $\delta\nu_{\text{BBR}}/\nu_0$ of Zn is a factor of approx. 20 lower. Due to the fact that the BBR shift in Sr is extensively investigated [63, 64], the errors are two orders of magnitude lower than in Zn. However, with further research, a similar fractional uncertainty might be reached for Zn. This might allow superior clock performance for possible Zn lattice clocks.

Table 2.4: Absolute and relative Blackbody radiation shifts, $\delta\nu_{\text{BBR}}$ and $\delta\nu_{\text{BBR}}/\nu_0$ for Zn [9], Sr [63, 65, 66] and Hg [67] at a temperature 300 K. For these numbers, the temperature is considered to be error-free.

Element	$\delta\nu_{\text{BBR}}$ [Hz]	$\delta\nu_{\text{BBR}}/\nu_0$	$\Delta(\delta\nu_{\text{BBR}}/\nu_0)$
Zn	-0.244 ± 0.010	-2.5×10^{-16}	1×10^{-17}
Sr	-2.28074 ± 0.00043	-5.3×10^{-15}	1×10^{-18}
Hg	-0.181	-1.5×10^{-16}	

2.3.3 Clock light distribution via fiber network

One major application of clocks is the synchronization of different nodes located around the globe. Large scale experiments like very long baseline interferometry [68, 69] or tests of general relativity [70] rely on precise synchronization of atomic clocks [71]. Further, progress on the clocks' performance might be enhanced by direct comparison, as their mismatch reveals the accuracy and possible uncertainties [72]. This can be also used to measure frequency ratios of different transitions and observe variations in time [73].

Today's most promising way of distributing a clock signal over long distance are fiber links, which allow comparisons with an uncertainty level down to 10^{-20} over distances larger than 1000 km [74, 75].

However, optical fibers introduce a phase instability on the guided light broadening its linewidth towards the kHz regime. To face this issue, the phase noise cancellation techniques have been developed and are successfully applied [76]. Further, optical fibers suffer from transmission losses, as displayed in Fig. 2.4. Pure fused silica glass intrinsically absorbs light in the mid- and far infrared as well as in the UV range. Mechanisms like Rayleigh scattering limit the transmission at lower wavelengths and overtones of hydroxide ion resonances appear around 720 nm, 950 nm and 1380 nm [77]. The losses lead to the need of phase-coherent amplification of the clock light, demanding extensive technical adjustments of existing fiber networks [72]. The lower the losses are the less effort on amplification is needed.

The fourth and fifth sub-harmonic of the Zn clock transition wavelength, 1240 nm and 1550 nm, fall into the spectral regions of minimal absorption. As the telecommunication fiber network operates around 1550 nm, the clock laser might be directly distributed by an established network.

Hence, a laser system has been developed in this research group deriving light by frequency quintupling a laser at around 1550 nm. This has been performed by the master student Maya Büki and has been published in [33]. A further description can be found in Section 2.4.3 and in Refs. [32, 33].

2.4 Laser systems

For slowing and cooling atoms, efficient transfer of momentum from the light on the atoms is essential. Achieving a large scattering rate is the key for increasing the number of captured atoms [78, 79]. A typical approach for lattice clocks is slowing and capturing atoms in a MOT operating on the broad singlet state, which is at 214 nm in Zn. Afterwards, the atoms are transferred to a MOT operating on the triplet transition, which lies at 308 nm in Zn. Here, the atoms are cooled to the recoil limit, as the Doppler temperature is lower than the recoil temperature [5]. Thus, (at least) two laser systems

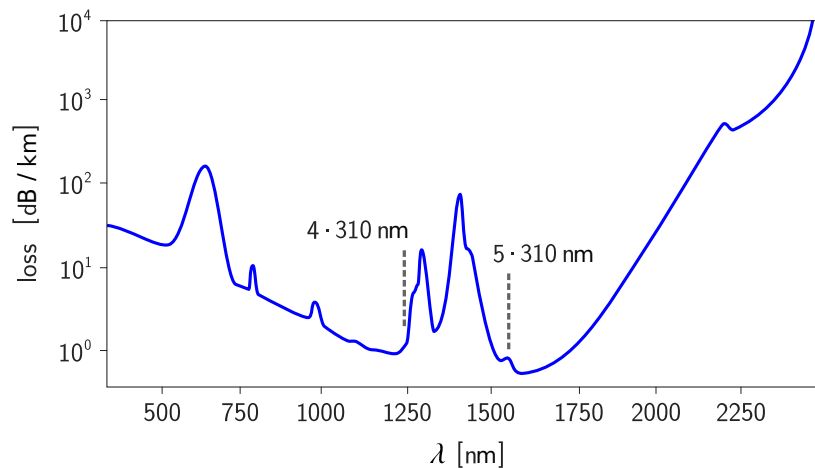


Figure 2.4: The figure demonstrates a typical example of transmission losses in optical fibers. Specifically, this loss spectrum corresponds to a fiber with low OH-concentration. The specific spectral shape of each fiber varies, as the OH-concentration might be different and impurities add further absorption peaks. The fourth and fifth harmonic of the clock transition at 310 nm falls into the regions of minimal absorption and are marked. The figure is adapted from Ref. [24].

are required, before transferring the atoms into an optical lattice. For probing the clock transition, a third laser system is needed. The three mentioned laser systems are set up in the laboratory and in the upcoming sections, their construction and operability are discussed.

2.4.1 214-nm laser

One promising way to obtain high power UV laser light is frequency quadrupling of a high power infrared laser in two consecutive frequency doubling cavities. By doing so, different research groups obtained more than 2 W at 261 nm [80], more than 1 W for 243 nm [81, 82], but less than 200 mW at 229 nm on time scales significantly longer than 100 h [83]. Lasers at 205 nm reach up to 15 mW, but rely on sum-frequency generation [84].

The most challenging aspect for deep UV light generation is the degradation of beta barium borate crystals (BBO), which are used for second harmonic generation (SHG) to the UV [83, 85, 86]. The degradation originates from the formation of absorption centers in the crystal, decreasing the intra-cavity power and deteriorating the mode profile of the UV [85].

This issue can be overcome in two different ways: The crystal can be heated to temperatures above 70 °C [85], which might lead to outgassing in the cavity, unwanted heat convection and temperature isolation issues. The alternative, used here, are SHG cavities with an elliptical focus of the fundamental beam in the crystal reducing intensity without loss of SHG output power [87, 88].

In the following, the laser, which was built together with the master student Marc Vöhringer [31], is discussed. The setup is depicted in Fig. 2.5 and its components will be explained in the following.

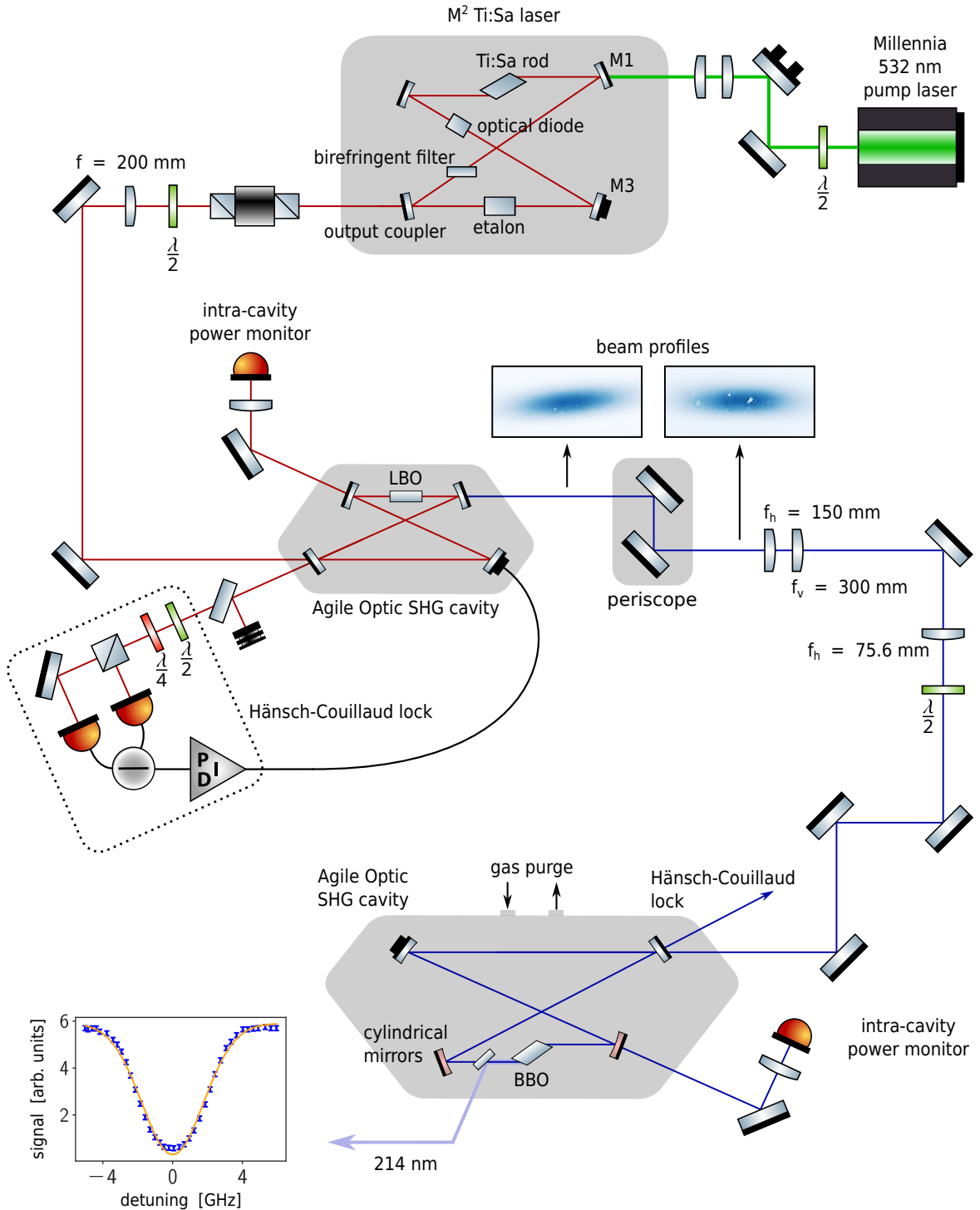


Figure 2.5: Sketch of the 214 nm laser. The beam profiles have been recorded with a USB camera. The circular interference patterns are created by dust on optical attenuators that are mounted to the camera. f_h and f_v denote focal lengths of cylindrical lenses oriented horizontally or vertically, respectively. The laser's operability is confirmed by measuring Doppler broadened absorption in a Zn vapor cell. The measurement has been conducted by Marc Vöhringer and the illustration of the beam profiles before and after the periscope is adapted from Ref. [31].

Laser source

Laser light is derived from a continuous wave titanium-sapphire laser (Ti:Sa)⁴, delivering 4.3 W light power at 856 nm with a short-term linewidth (100 μ s) smaller than 100 kHz⁵. The titanium-sapphire crystal provides a large gain spectrum and thus, the laser can be operated between 700 nm and 1000 nm. It is pumped by a frequency doubled, diode pumped yttrium orthovanadate (Nd:YVO₄) laser at 532 nm⁶. The pump laser emits maximum 18 W light with vertical polarization, which is adjusted to horizontal by a waveplate. The light is coupled into the crystal through mirror M1 with the M^2 beam steering stage, providing a set of lenses and two mirrors. One of these mirrors can be piezo tuned in both axes for fine adjustment. The crystal is placed within a bow tie cavity operating on the converted light enforcing stimulated emission. The cavity length is adjusted by mirror M3, which is mounted on a piezo crystal. Further frequency selection takes place with a built-in birefringent filter. Additionally, an in-built etalon can be locked to the light frequency minimizing the occurrence of mode jumps. Light propagating the wrong way in the cavity significantly disturbs the operation of the system and is inhibited by an optical diode. Nevertheless, a small part of the emitted laser light is retro-reflected by the SHG crystal of the consecutive frequency doubling cavity and introduced mode-jumps. Hence, the laser is protected additionally by a 60 dB optical isolator.

During operation, a degradation of the laser's output power was observed on time scales of one to several weeks. The power could temporarily and partly be restored by re-coupling of the pump laser. Over time, the optimal angle, from which the pump laser enters the laser housing, has grown exceptionally large. At this angle, the beam steering mirrors would not be hit anymore. Thus, the loss in power was not avoidable. A photograph of the beam impinging on the second steering mirror is shown in Fig. 2.6. A protection aperture, fixed on the steering stage, had to be removed as well to enable any coupling of the pump laser into the titanium-sapphire laser. For future optimization of the setup, the degradation of the output power should be eliminated. During the writing process of this thesis, the laser has been sent for repair, as its cavity mirror positions have to be rearranged by resoldering their mounts to the baseplate.

SHG cavity for 856 nm to 428 nm conversion

The infrared light passes through a waveplate to adjust the polarization of the light and an $f = 200$ mm lens for mode matching the first SHG cavity⁷ operating on the fundamental light. This allows a coupling efficiency of 95%. An angle phase matched lithium triborate (LBO) crystal stabilized at 43 °C enables the SHG process to 428 nm. The cavity alignment has been optimized by alternatively positioning the cavity mirrors in their mirror mounts and the crystal on a five-axis stage. The cavity finesse \mathcal{F} has been measured by scanning the cavity length over multiple TEM₀₀ resonances and comparing their linewidth to their separation. Performing the measurement in this way, $\mathcal{F} \approx 330$ has been obtained for low input power with negligible conversion. The result is well within the region of optimal performance⁸. The conversion efficiency η is defined as the ratio of power of the converted

⁴ M² SolsTiS 4000 PSX-XF

⁵ Information from the M² test sheet

⁶ Spectra-Physics Millennia eV

⁷ Agile Optic SHG resonator from IR to VIS

⁸ According to the communication with Agile Optic, piezo non-linearities can be neglected. Further, we have been told that the optimum finesse should be around 300.



Figure 2.6: The figure shows a photograph of the pump laser beam impinging on the second steering mirror. At this stage, the power degradation has progressed to the point where the beam hits the top of the mirror. During the system's operation, the spot continued to rise even further. During the writing process of this thesis, the laser was sent for repair.

light $P_{428\text{ nm}} = 2.1\text{ W}$ to the power of the fundamental light $P_{856\text{ nm}} = 3.0\text{ W}$. $\eta = 70\%$ has been obtained in this work.

Given that the conversion process in LBO is polarization selective, the cavity resonance is stabilized on the fundamental laser frequency with the Hänsch-Couillaud locking scheme [89] utilizing the reflected light from the cavity. p-polarized light is coupled into the cavity and experiences a varying phase shift near resonance. s-polarized light does not enter the cavity and serves as a constant phase reference. With the help of one half- and one quarter-waveplate as well as a differential photodiode, a dispersion shaped error signal is generated. This method is advantageous compared to the Pound-Drever-Hall technique, as it does not rely on sidebands, which might be transmitted through the SHG cavity.

Due to the walk-off in LBO [90], the output beam has the profile of a tilted ellipse (see Fig. 2.5) with an axis ratio of about 4 and a tilt angle of 5° . It has been observed that the tilt inhibits proper beam shaping with elliptical lenses, as the axes of lenses and light do not match. Thus, a periscope has been constructed to rotate the ellipse.

SHG cavity for 428 nm to 214 nm conversion

The output beam of the first doubling stage is focused by cylindrical lenses to match the elliptical waist in the second frequency doubling cavity⁹. All cylindrical lenses are glued to fixed height posts, as they feature a lower tilt as typical variable height posts. Already a mismatch of lens axis and elliptical beam axis around 0.3° significantly deteriorates the mode matching. Further, a half-waveplate is used to adjust the polarization to the cavity's requirement. A coupling efficiency of 70% is obtained¹⁰. The cavity is equipped with a 1 cm long BBO crystal, which is cut in Brewster's angle, as the performance of anti-reflection coatings decreases towards lower wavelengths. A dichroic mirror at Brewster's angle

⁹ Agile Optic Custom SHG-resonator from VIS to UV

¹⁰ 70% is a comparable performance to other groups have reached with elliptical cavities. The information is obtained by personal communication.

serves as an outcoupler, as it reflects the generated 214 nm, but transmits the fundamental light. This prevents UV light penetration into the mirror coatings and thus possible damage from the mirrors. The alignment procedure involves 15 degrees of freedom, from which six originate from tilting three mirrors, two from axes match of two cylindrical mirrors, five from the crystal alignment and two from the Brewster outcoupler. The obtained finesse has been around 270 and is slightly lower than the optimum value of 300. The maximum output power has been 10 mW at $P_{428\text{ nm}} = 2\text{ W}$. The laser's functionality has been tested by an absorption measurement in a Zn vapor cell (Fig. 2.5). However, the obtained power does not meet the requirement for laser cooling of Zn. A cavity identical in construction is used in other research groups, obtaining more than 200 mW at 229 nm¹¹. According to their experience, the crystal's performance can vary largely.

For further optimization of the SHG process, tests have to be performed on the cavity optics to check their performance and identify unwanted loss channels of UV light and intra-cavity power. This especially concerns the crystal, the Brewster outcoupler and the transmission of the output window for UV wavelengths.

Particular effort has to be given to avoid moisture and air humidity in the cavity, as the BBO crystal degrades while reacting with water. Thus, during operation the cavity is purged with synthetic air¹², in which the H₂O contamination is below 0.5 ppm-mol. To keep the purity of the air, all pipes are from PTFE and were cleaned with silicone remover in an ultrasonic bath to avoid hydrocarbon contamination. Additionally, the lid is air tightly closed and sealed with indium. The crystal temperature is stabilized to a temperature slightly above room temperature to minimize condensation even further.

2.4.2 308-nm laser

To address the ³P₁ intercombination transition in Zn, a commercial laser at 308 nm has been purchased¹³, which is similar to systems used in Refs. [91–93]. The laser is constructed by deriving the output from a diode laser in Littrow configuration at 1232 nm [94]. The light power is enhanced by the use of a tapered amplifier chip [95] to 450 mW.

Modulating the laser current generates 5 MHz sidebands on the laser light, which are used to lock two consecutive frequency doubling cavities with the Pound-Drever-Hall method. The first SHG cavity features approx. 55 % conversion efficiency and outputs 250 mW of 616 nm light. The second conversion stage emits up to 60 mW at 308 nm.

The SHG crystal's angle within the last doubling stage limits the tunability of the system, as the stage is near at its end of range for larger wavelengths. Nevertheless, the wavelength can be tuned to 310 nm, the wavelength of the clock transition. Here, around 35 mW of light can be obtained. This laser has been used by the master student Marc Vöhringer trying to measure direct absorption on this line [31].

2.4.3 310-nm clock laser

The subsequent section briefly summarizes Ref. [33]. The work has been performed together with the master student Maya Büki. The author of this thesis acted as a supervisor and participated in the practical work. The spectroscopy setup has been developed and constructed by the author. More

¹¹ Personal communication

¹² Air Liquide ALPHAGAZ II LUFT

¹³ Toptica DLC TA FHG pro

detailed information on the system can be found in Refs. [32, 33].

To fulfill the demand of a fiber network compatible clock laser (see Section 2.3.3), a fiber laser at 1547.5 nm serves as the fundamental laser¹⁴. It emits 40 mW with an intrinsically low linewidth of below 100 Hz¹⁵. The frequency tuning range is specified to approx. 1 nm and limits the tuning range of the entire system. The light power is increased by a fiber amplifier, delivering up to 16.5 W of infrared light.

Calculations have shown that obtaining the highest UV light yield is achieved by one frequency doubling stage and two sum frequency generation stages, which is introduced in more detail in the following:

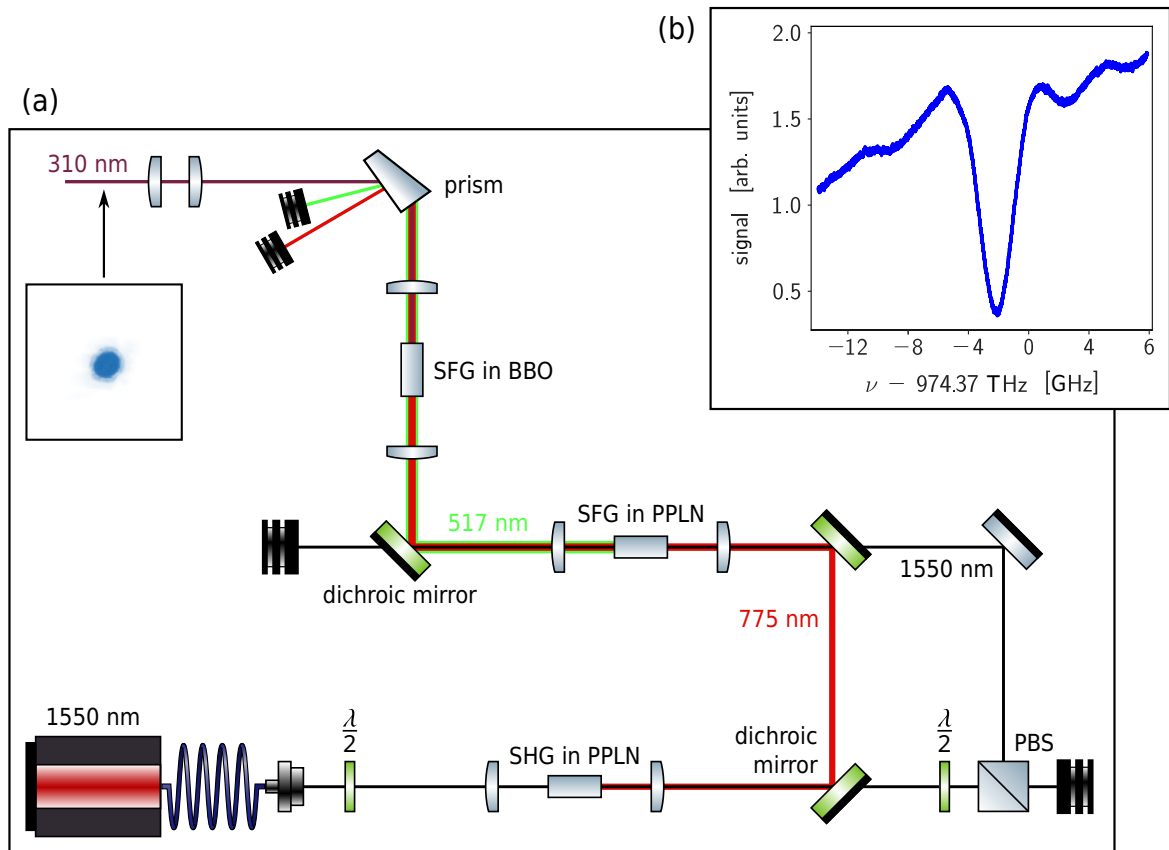


Figure 2.7: (a): Setup and beam profile of the 310 nm laser. (b): A Doppler broadened absorption profile of the 3P_1 intercombination line at 308 nm acquired by a linear spectroscopy in a Zn vapor cell. A wavemeter (High Finesse WS-8-5) served as frequency reference. The measurement data has been taken by Maya Büki. Both figures are adapted from Ref. [33].

After adjustment of the fundamental polarization and focusing according to the Boyd-Kleinman theory [90, 96], the light is frequency doubled in single-pass in a 4 cm long MgO-doped periodically poled lithium niobate crystal, 5 %MgO:PPLN. By utilizing quasi-phase matching, 3 W of 775 nm

¹⁴ NKT Photonics ADJUSTIK E15

¹⁵ This information is obtained from the datasheet. The linewidth has not been measured by ourselves.

light are generated from 15 W fundamental light. The doubled light is split of by a dichroic mirror to be able to reduce the power of the fundamental for the second conversion stage. In this stage, 517 nm light is generated by sum frequency generation of 775 nm and 1550 nm. As the green light causes the GRIIRA effect, green-induced infrared absorption [97, 98], in MgO:PPLN, the conversion efficiency decreases for input powers exceeding 10 W of the fundamental light. Hence, the maximum achieved power for 517 nm light is 500 mW. The last conversion stage relies on sum frequency generation of the green and the 775 nm to obtain 310 nm light. As it is technically too challenging to produce the narrow poling period in PPLN for these wavelengths, a type I phase-matching BBO crystal is used. As the conversion efficiency of BBO is limited for this process, the output power at 310 nm is 0.5 mW. Comparing this power at a conveniently achieved beam diameter of 100 μm , a saturation parameter $s = I/I_{\text{sat}}$ of about 10^{13} is obtained for the clock transition. To compensate the walk-off in BBO, beam shaping is performed with cylindrical lenses. The output beam profile as well as a sketch of the entire setup is shown in Fig. 2.7 (a).

As the setup relies on a fiber amplifier with broad gain spectrum, different laser sources can be used, *e.g.*, a distributed-feedback laser diode laser source has been used at 1538 nm to generate light for the $^3\text{P}_1$ intercombination transition in Zn. To test the performance, a linear absorption spectroscopy has been performed in a vapor cell. One measurement trace is depicted in Fig. 2.7 (b).

Nuclear features in atomic spectra

The following chapter offers a theoretical overview about two nuclear characteristics in atomic spectra, namely isotope shifts and hyperfine interaction. Furthermore, the effect of quantum interference in optical spectra is introduced. This is of interest for Chapters 4 and 5 and the publications reprinted in Appendices A and B.

3.1 Origin and contributions to isotope shifts

The term isotope shift refers to the energy difference of an electronic state among different isotopes. The difference in resonance frequency of two isotopes with mass numbers A and A' can be written as

$$\delta\nu^{A,A'} = \nu^A - \nu^{A'}. \quad (3.1)$$

In a simplified approach, $\delta\nu^{A,A'}$ can be decomposed into two main contributions [99, 100], which are called the mass shift $\delta\nu_{\text{MS}}^{A,A'}$ and the field shift $\delta\nu_{\text{FS}}^{A,A'}$

$$\delta\nu^{A,A'} = \delta\nu_{\text{MS}}^{A,A'} + \delta\nu_{\text{FS}}^{A,A'}. \quad (3.2)$$

These contributions are explained in more detail in the upcoming sections.

3.1.1 Mass shift

In general, the mass shift is the largest contribution for isotope shifts in lighter elements. This term arises because of the finite nuclear mass and because the mass differs for different isotopes [101]. In non-relativistic calculations, the nuclear kinetic energy operator can be written as $\mathbf{P}_{\text{N}}^2/(2M_{\text{A}})$ with \mathbf{P}_{N} the nuclear momentum and M_{A} the nuclear mass of isotope A . In the atom's rest frame, the difference of this operator is expressed for isotopes A and A' as

$$\Delta H_{\text{mass}}^{A,A'} = \left(\frac{1}{M^{A'}} - \frac{1}{M^A} \right) \left(\frac{1}{2} \sum_i p_i^2 + \frac{1}{2} \sum_{i \neq j} \mathbf{p}_i \cdot \mathbf{p}_j \right), \quad (3.3)$$

with the sums taken over the momenta of the electrons. Eq. (3.3) consists of one-body and two-body terms, corresponding to the normal and the specific mass shift [102].

In the calculation of the isotope shift, both contributions are summarized in an effective mass shift coefficient K with

$$\delta v_{\text{MS}}^{A,A'} = K \left(\frac{1}{M^{A'}} - \frac{1}{M^A} \right). \quad (3.4)$$

A relation between the mass shift parameters of different transitions may be found in a King plot analysis (see Section 3.2).

3.1.2 Field shift

The field shift is the dominant contribution in case of heavy atoms [103]. As the neutron number is different among the isotopes, the nuclear charge distribution is rearranged for each isotope. This leads to a change in the nuclear potential, causing a shift of the isotope's energy levels. For the following discussion, the nuclear charge distribution $\rho(\mathbf{r})$ depends solely on a well-defined isotope dependent charge radius [104]

$$\langle r^2 \rangle = \frac{\int_0^\infty \rho(\mathbf{r}) r^2 d\mathbf{r}^3}{\int_0^\infty \rho(\mathbf{r}) d\mathbf{r}^3}. \quad (3.5)$$

Thereby, $\rho(\mathbf{r})$ is assumed to be non-deformed so that higher order corrections on isotope shifts can be neglected. In theoretical calculations, the potential difference $\Delta V_{A,A'}$ with respect to the difference of the squared charge radii $\Delta \langle r^2 \rangle_{A,A'}$ can be expressed as

$$\Delta V_{A,A'} = \left(\frac{\partial V}{\partial \langle r^2 \rangle} \right) \Delta \langle r^2 \rangle_{A,A'} + \left[\frac{\Delta V_{A,A'}}{\Delta \langle r^2 \rangle_{A,A'}} - \left(\frac{\partial V}{\partial \langle r^2 \rangle} \right) \right] \Delta \langle r^2 \rangle_{A,A'} \quad (3.6)$$

$$\approx \left(\frac{\partial V}{\partial \langle r^2 \rangle} \right) \Delta \langle r^2 \rangle_{A,A'}. \quad (3.7)$$

The term within the square brackets in Eq. (3.6) gives rise to small correction terms, which can be neglected here. Applying first-order perturbation theory, an effective field shift parameter F can be introduced

$$F = \langle \psi_A | \left(\frac{\partial V}{\partial \langle r^2 \rangle} \right) | \psi_A \rangle / h \quad (3.8)$$

through which the field shift can be described as

$$\delta v_{\text{FS}}^{A,A'} = F \Delta \langle r^2 \rangle_{A,A'}. \quad (3.9)$$

Similarly to the mass shift parameter, the field shift parameters are related to each other in a King plot analysis (see Section 3.2). However, a few points should be noted:

- Applying second-order perturbation theory yields the second-order field shift, which can be treated similarly as $\delta v_{2\text{nd order FS}}^{A,A'} = G \Delta \langle r^2 \rangle_{A,A'}^2$.
- There are a large number of corrections to the shown derivation, *e.g.*, from the approximation in Eq. (3.7). Furthermore, especially large nuclei distort from a spherical shape. For an axially symmetric, static quadrupole deformation, the charge radius is replaced by $\langle r \rangle = \langle r_0 \rangle \left(1 + \frac{5}{4\pi} \beta_2\right)$ in the lowest order with β_2 being a quadrupole deformation parameter [105]. *E.g.*, for Yb this results in terms scaling with $\Delta \langle r^4 \rangle_{A,A'}$ or even higher powers [106].
- The previously shown terms originate from a non-relativistic calculation. In relativistic calculations, the exponent of r in Eq. (3.9) depends on the quantum number j of the respective electronic state and deviates from 2. These corrections are not considered as relevant for this work, but are highly important for isotope shift measurements with single Hz precision [25].

3.2 King plots

A useful tool to compare measured isotope shifts to each other is given by so-called King plots [99, 107]. To simplify their introduction, it is assumed that the mass and the field shift are the only contributions to isotope shifts and higher order terms are negligibly small. Then,

$$\delta v^{A,A'} = K \left(\frac{1}{M^{A'}} - \frac{1}{M^A} \right) + F \Delta \langle r^2 \rangle_{A,A'} \quad (3.10)$$

holds true. The further analysis takes place by introducing modified isotope shifts $\delta m^{A,A'}$, where $\delta v^{A,A'}$ is scaled by

$$\mu = \frac{M^{A'} M^A}{M^{A'} - M^A} \quad (3.11)$$

to remove the mass dependence from the mass shift term

$$m\delta^{A,A'} = K + \mu F \Delta \langle r^2 \rangle_{A,A'}. \quad (3.12)$$

If the nuclear masses and the squared charge radii differences are known for a set of isotopes, F and K can be obtained for the respective transition from Eq. (3.12). As the uncertainties of $\Delta \langle r^2 \rangle_{A,A'}$ are typically larger than the ones of the isotope shifts, this term is eliminated for a King plot. Therefore, the modified isotope shift on a different transition of the same atomic species¹ can be substituted into Eq. (3.12). Then, the equation reads for transitions i and j

$$m\delta_i^{A,A'} = K_i - K_j \frac{F_i}{F_j} + \frac{F_i}{F_j} m\delta_j^{A,A'}. \quad (3.13)$$

¹ Also, isotope shifts of transitions in neutral atoms can be compared with transitions in ions.

Eq. (3.13) gives a linear relation between modified isotope shifts between different transitions. Plotting $m\delta_1^{A,A'}$ against $m\delta_j^{A,A'}$ and fitting a linear function, a relation between the field and mass shift coefficients of different transitions can be obtained.

Isotope shift measurements in atoms with non-deformed nuclei can be cross-checked for consistency with other measurements, as the King plot of both measurements needs to show linearity. Non-linearities may become apparent in isotope shift measurements with precision at the kilohertz scale in Yb [106] or below the 10 Hz scale in Ca [21, 25]. Here, second-order field shifts and nuclear deformation effects become significant in Yb. These correction terms can be eliminated with isotope shift measurements on additional transitions in generalized King plots [108]. Then, or if the correction terms are known with sufficient precision, it may even be possible to identify new physics phenomena, such as a new gauge boson mediating an interaction between electrons and neutrons. The search for new physics is a topic of large research efforts [21, 22, 28, 106, 109–112]. Isotopes with zero nuclear spin are preferred for these measurements, as the absence of hyperfine structure circumvents center of gravity determination and thus have a higher precision.

3.3 Hyperfine structure and quantum interference

This section discusses the hyperfine structure arising from the interaction between electrons and the nucleus. Following this, quantum interference is introduced, which must be considered when studying atomic transitions with linewidths that are comparable to their energy separations.

3.3.1 Hyperfine structure

Nuclei with a non-vanishing nuclear spin I possess a magnetic dipole moment, which interacts with the surrounding electrons. This lifts the degeneracy of the magnetic sublevels of the atomic fine structure states. To describe the interaction, the total angular momentum operator F is introduced as,

$$F = I + J \quad (3.14)$$

with J being the total electron angular momentum. The respective quantum number F takes values of

$$|I - J| \leq F \leq |I + J| . \quad (3.15)$$

The energy shift between the hyperfine states can then be written as

$$\Delta\nu_{\text{HFS}, A} = \frac{A}{2h} C \quad (3.16)$$

where A denotes the hyperfine constant and

$$C = F(F + 1) - I(I + 1) - J(J + 1) . \quad (3.17)$$

The average electric field gradient of the electrons at the site of the nucleus and a non-spherical nuclear charge distribution give rise to an electric quadrupole interaction. This interaction contributes to the total hyperfine splitting, which is then written as

$$\Delta\nu_{\text{HFS}} = \frac{A}{2}C + \frac{\frac{3}{4}C(C+1) - I(I+1) - J(J+1)}{2I(I+1)J(J+1)}. \quad (3.18)$$

Hyperfine splittings in Zn are smaller than one linewidth on the $^1\text{P}_1$ transition (Chapter 4) and several GHz on the $^3\text{P}_1$ transition [113].

3.3.2 Quantum interference

For fluorescence spectroscopy on states, whose the energy difference is on the same order of magnitude as their linewidths, the effect of quantum interference may significantly alter the lineshape of the states. A theoretical lineshape model has been developed by Brown *et al.* [114], for laser-induced fluorescence (LIF) experiments, as performed during this work (see Chapter 4 and Appendix A). The following section summarizes their findings to provide the theoretical background for the lineshape observed in the measurement shown in Chapter 4 and Appendix A.

In LIF spectroscopy, laser light excites an atom from an initial state i to an excited state e , which decays into a final state f . The differential scattering rate into solid angle Ω_s is written as

$$\frac{dR_{i \rightarrow f}}{d\Omega_s} = \frac{\pi E_L^2 \omega_s^3}{h^3 c^3 \epsilon_0} \left| \sum_e \frac{(\hat{\epsilon}_s^* \cdot \mathbf{D}_{fe})(\mathbf{D}_{ei} \cdot \hat{\epsilon}_L)}{\Delta_{ei} - i\Gamma_e/2} \right|^2, \quad (3.19)$$

which depends on the frequency, wave vector and polarization of the incident light ($\omega_L, \mathbf{k}_L, \hat{\epsilon}_L$) and the scattered light ($\omega_s, \mathbf{k}_s, \hat{\epsilon}_s$), the laser detuning $\Delta_{ei}/(2\pi) = \nu_L - (\nu_e - \nu_i)$ and the electric field amplitude E_L . \mathbf{D}_{ij} denotes the atomic dipole matrix element. Using a vector basis with $q = 1, 0, -1$ for σ^+, π and σ^- light, the dipole matrix element can be written as

$$\left[D_{F^i m^i}^{F^e m^e} \right]_q = \frac{\langle F^e || \mathbf{D} || F^i \rangle}{\sqrt{2F^e + 1}} \langle F^i m^i; 1q | F^e m^e \rangle, \quad (3.20)$$

where \mathbf{D} denotes the dipole operator. $\langle F^i m^i; 1q | F^e m^e \rangle$ represents the Clebsch-Gordan coefficient for adding $|F^i m^i\rangle$ and $|1q\rangle$ to obtain $|F^e m^e\rangle$ and is given by

$$\langle F^i m^i; 1q | F^e m^e \rangle = (-1)^{F^e - m^e} \sqrt{2F^e + 1} \begin{pmatrix} F^e & 1 & F^i \\ -m^e & q & m^i \end{pmatrix} \quad (3.21)$$

with the brackets denoting the 3-j symbol. With the 6-j symbol written in curly brackets, the angular momentum relation

$$\langle F^e || \mathbf{D} || F^i \rangle = \langle J^e || \mathbf{D} || J^i \rangle (-1)^{F^i + I + J^e + 1} \sqrt{(2F^i + 1)(2F^e + 1)} \begin{Bmatrix} J^e & F^e & I \\ F^i & J^i & 1 \end{Bmatrix} \quad (3.22)$$

can be used to reduce the matrix element. Then, Eq. (3.20) can be written as

$$\begin{aligned}
 \left[D_{F^i m^i}^{F^e m^e} \right]_q &\propto (-1)^{J^i+S+L^e+1} \sqrt{(2J^i+1)(2J^e+1)} \begin{Bmatrix} L^e & J^e & S \\ J^i & L^i & 1 \end{Bmatrix} \times \\
 &(-1)^{F^i+I+J^e+1} \sqrt{(2F^i+1)(2F^e+1)} \begin{Bmatrix} J^e & F^e & I \\ F^i & J^i & 1 \end{Bmatrix} \times \\
 &(-1)^{F^e-m^e} \begin{pmatrix} F^e & 1 & F^i \\ -m^e & q & m^i \end{pmatrix}.
 \end{aligned} \tag{3.23}$$

Using Eq. (3.23) and assuming that the atom is excited with light linearly polarized along the \hat{z} axis (with a k -vector pointing in \hat{x} direction), the corresponding excitation matrix elements are given by

$$D_{ei} = \left[D_{F^i m^i}^{F^e m^e} \right]_{q=0}. \tag{3.24}$$

For the calculation of the spatial radiation pattern, decay matrix elements are given as

$$D_{fe} = \sum_{q=-1}^1 \left[D_{F^e m^e}^{F^f m^f} \right]_q \epsilon_q. \tag{3.25}$$

In the following, the specific case is considered that the fluorescence power is measured with two orthogonal detectors. They are oriented along \hat{y} and \hat{z} , as it is the case in the measurements shown in Chapter 4 and Appendix A. Thus, the fluorescence's polarization vector at the detector reads

$$\hat{\epsilon} = \left(\frac{1 + \cos(\theta)}{\sqrt{2}}, \sin(\theta), \frac{1 - \cos(\theta)}{\sqrt{2}} \right)^T, \tag{3.26}$$

which equals $\epsilon = \hat{x} + i \cos(\theta) \hat{y} + \sin(\theta) \hat{z}$ in Cartesian coordinates with θ being the angle between the laser's polarization and the direction of detection. This parametrization allows for polarization components along \hat{x} and \hat{y} measured by the detector oriented along \hat{z} and polarization components along \hat{x} and \hat{z} for the detector oriented along \hat{y} .

Using Eqs. (3.25) and (3.26), the hyperfine transition spectrum including quantum interference is finally obtained by calculating

$$S = \sum_{i,f} \left| \left(\sum_e \frac{D_{ei} D_{fe}}{\Delta_{ei} - i\frac{\Gamma}{2}} \right) \right|^2. \tag{3.27}$$

The result is of the form

$$S = \frac{\Gamma^2}{4} \{ \mathcal{A} + [\mathcal{B} + C] P_2(\cos(\theta)) g(\theta_C) \}, \tag{3.28}$$

where $P_2(\cos(\theta))$ is the second Legendre polynomial and $g(\theta_C) = \cos(\theta_C) \cos^2(\theta_C/2)$ a correction factor accounting for the solid angle θ_C of the fluorescence detector. Eq. (3.28) is separated in an angle dependent and an angle independent component: The independent part is given by \mathcal{A} , which contains one Lorentzian function for each hyperfine state. \mathcal{B} and C contribute to the angle dependent part. For each hyperfine state, \mathcal{B} contains one Lorentzian function, providing small correction to the amplitudes of the Lorentzians in \mathcal{A} . C consists of cross terms between the hyperfine states, which cause the

modification of the observed lineshape. Far from resonance, these terms decay as $1/(\Delta_{F1}\Delta_{F2})$, where Δ_F denotes the laser's detuning to the hyperfine state F . Thus, these terms are significant, if the hyperfine splitting and the linewidth are comparably large. As this is the case for the $^1S_0 \rightarrow ^1P_1$ transition in ^{67}Zn , quantum interference has been taken into account in the spectroscopy experiment shown in Chapter 4 and Appendix A.

Hyperfine structure and isotope shifts of the $^1S_0 \rightarrow ^1P_1$ transition in zinc

The development of cold atom experiments relies on detailed spectroscopic information on the cooling transitions of the respective atomic species. Before such experiments are designed and constructed to the specific needs for Zn, it is helpful to accurately characterize the $(4s^2)^1S_0 \rightarrow (4s4p)^1P_1$ transition at 214 nm, which acts as the main cooling transition. In this regard, the hyperfine structure of ^{67}Zn as well as the isotope shifts of all stable isotopes of Zn are of particular interest [115, 116].

Previously reported isotope shift measurements on the main cooling transition in Zn have been performed using more traditional methods. For example, light emitted from hollow cathode or discharge lamps, or the fluorescence from an atomic beam has been analyzed with spectrometers [19, 20, 55]. These techniques provided valuable data on the isotope shifts and hyperfine structure of Zn, but the achieved precision has been limited by the resolution of the spectrometers and the broad spectral lines produced by the sources. For the isotope shifts, this has led to uncertainties significantly larger than 50 MHz. This uncertainty corresponds to approximately 10 % of the shift itself and to more than half the natural linewidth.

Progress in laser technology and precision experiments has enabled laser spectroscopy on transitions in the deep UV range. Nowadays, frequency tunable, narrow line, continuous-wave laser systems can be constructed, addressing transitions that occur below 220 nm and delivering several mW of power (for example, see Section 2.4.1).

During this work, laser spectroscopy has been performed on the $(4s^2)^1S_0 \rightarrow (4s4p)^1P_1$ transition in Zn at 214 nm, by measuring the fluorescence of a cold atomic beam. The excited state's hyperfine coupling constants A and B of ^{67}Zn have been determined, considering the lineshape altering due to quantum interference (see Section 3.3.2). Additionally, the isotope shifts have been determined for all stable isotopes. The precision achieved for the isotope shifts is below 5 MHz, providing a significant improvement over previously reported values.

The measurements have been performed at the Department of Molecular Physics of the *Fritz-Haber-Institut* of the *Max-Planck-Gesellschaft* in Berlin, in collaboration with the *Cold Molecule Group*. During previous studies on molecules in this group, a cryogenic buffer gas beam source has been developed and constructed [117, 118] based on the design in Ref. [119]. This atomic source allows to create cold atomic beams with a large variety of elements and has been successfully utilized to perform high resolution isotope shift measurements on various transitions in Cd [120, 121]. A similar

experimental approach has been applied for Zn in this study.

Furthermore, these measurements may contribute nuclear structure studies and to determine differences in nuclear charge radii among the isotopes. Zn nuclei have two protons above the $Z = 28$ shell closure and thus exhibit cumulative effects of single particle structure, shell closure, correlations and deformations near the proposed doubly magic nuclei, ^{68}Ni and ^{78}Ni . These effects have been studied in measurements of transitions between excited states [122–124]. Data with MHz precision on transitions from the ground state of neutral Zn is limited to a measurement of the $(4s^2)^1S_0 \rightarrow (4s4p)^3P_1$ transition¹ [113].

The content of this chapter has been published in Ref. [34]. The full citation reads

Hyperfine structure and isotope shifts of the $(4s^2)^1S_0 \rightarrow (4s4p)^1P_1$ transition in atomic zinc,
David Röser, J. Eduardo Padilla-Castillo, Ben Ohayon, Russell Thomas, Stefan Truppe, Gerard Meijer,
Simon Stellmer, and Sid C. Wright
Phys. Rev. A **109** (2024) 012806.

This chapter summarizes the publication, which is reprinted in Appendix A. **The author of this thesis contributed to the publication by transporting a stable ULE frequency reference cavity to Berlin and implementing the Pound-Drever-Hall method to stabilize an M^2 SolsTiS Ti:Sa laser to the cavity. The corresponding RF-circuit, which maintains the tunability by a carrier shift modulation with a voltage-controlled oscillator, as well as the optical setup were newly constructed. The cavity characterization, especially a high precision measurement of the free spectral range, has been performed by the author. Further, he was involved in taking the spectra and participated in operating and maintenance of the setup during the measurements².**

In the following, the measurement procedure is summarized by introducing the experimental setup and the laser system. The results are presented subsequently.

4.1 Atomic beam preparation and spectroscopy

The atom source, as depicted in Fig. 4.1 (a), contains a cell, which is used to generate the atomic beam and placed within heat shields in a high-vacuum. The cell contains a Zn target, which is ablated by a pulsed Nd:YAG laser at 1064 nm with a pulse repetition rate of 1 Hz. Initially, the vaporized atoms have a temperature of several 1000 K. They are cooled by collisions with helium (He) at a temperature of 3 K, which constantly flows through the cell. Finally, the Zn atoms reach a forward velocity of approximately 140 m s^{-1} limited by the velocity of the He. Detailed reviews of the dynamics within such a buffer gas cell and the atomic beam generation can be found in Refs. [125–127]. The remaining He is adsorbed by a charcoal layer on the inner heat shield and the exiting atomic beam is shaped by apertures. Hence, the transverse velocity distribution is narrowed to 2 m s^{-1} , ultimately leading to a Doppler broadening in the experiment of around 7 MHz, which is insignificant compared to the natural linewidth of about 111 MHz.

¹ To the very best of our knowledge

² All co-authors have agreed to the description of my personal contribution.

Spectroscopy is performed by guiding a laser beam at 214 nm orthogonally through the atomic beam, see Fig. 4.1 (a). A Glan-Thompson polarizer is used for polarization cleaning and a subsequent halfwave-plate for alignment of the polarization axis. Before each ablation pulse, the 214 nm-laser's frequency is tuned and the frequency is measured by a wavemeter. The fluorescence signal is recorded 5 ms to 8 ms after each ablation pulse, corresponding to the time the atoms need to reach the detection area. To collect the fluorescence, two photomultipliers are used, oriented along orthogonal directions to the propagation of the laser beam, see Fig. 4.1 (b). The two-orthogonal-detector method is advantageous, as the spatial emission pattern of the bosonic isotopes follows the one of a classical Hertzian dipole [121]: Choosing the angle θ between laser polarization and detection direction (see Fig. 4.1(c)), the fluorescence from bosonic isotopes is maximized or suppressed for $\theta = 90^\circ$ and $\theta = 0$, respectively. Hence, the visibility of the fermionic isotope can be increased in the acquired signals. Simultaneously, the fermionic lineshape is altered by quantum interference (see Section 3.3.2).

4.2 UV laser system and Pound-Drever-Hall lock

For these measurements, a laser system has been used, which is available at the *Fritz-Haber-Institut*. This laser has been utilized to drive transitions in AlF molecules and Cd atoms, but its frequency can be tuned to the respective transition in Zn [118, 121]. Similarly to the system built in Bonn (see Section 2.4.1), the light is derived from a titanium-sapphire laser, which is frequency quadrupled using two consecutive frequency doubling cavities³. However, the last doubling stage relies on a spherical mode for UV light generation, accelerating the degradation of the output power. To minimize the degradation, the frequency doubling cavities are driven with reduced laser power, to generate a few mW at 214 nm. The UV power at the position of the atomic beam is constantly monitored and the fluorescence yield is related to the measured power.

For a high resolution measurement on isotope shifts, the laser undergoes a carrier shift modulation, where one sideband is stabilized to a ULE cavity⁴ with a Pound-Drever-Hall locking scheme [128]. The laser's frequency is precisely referenced to the cavity by measuring the carrier shift frequency at a time close to the ablation pulse. After each measurement, the frequency is tuned by modifying the carrier shift frequency, while the stabilization is active. A sketch of the lock setup is depicted in Fig. 4.2.

This locking method fails, when the carrier shift frequency equals half of the cavity's free spectral range $\Delta\nu_{\text{FSR}}$. To reference the laser frequency to the cavity over a wider range, the laser is locked to different cavity modes. Therefore, the cavity's free spectral range has been measured by scanning the unlocked laser over the midpoint between two cavity modes, while sidebands have been applied with an EOM at different frequencies. The resulting cavity spectrum reveals two peaks, if the sideband frequency is far away from $\Delta\nu_{\text{FSR}}/2$, while it shows a single Lorentzian peak near $\Delta\nu_{\text{FSR}}/2$. By analyzing its amplitude for different sideband frequencies and fitting the data to find the position of maximum amplitude, the FSR it measured to be $(2\,992\,184 \pm 30)$ kHz.

³ M² SolsTiS ECD-X

⁴ Menlo ORS-Cubic

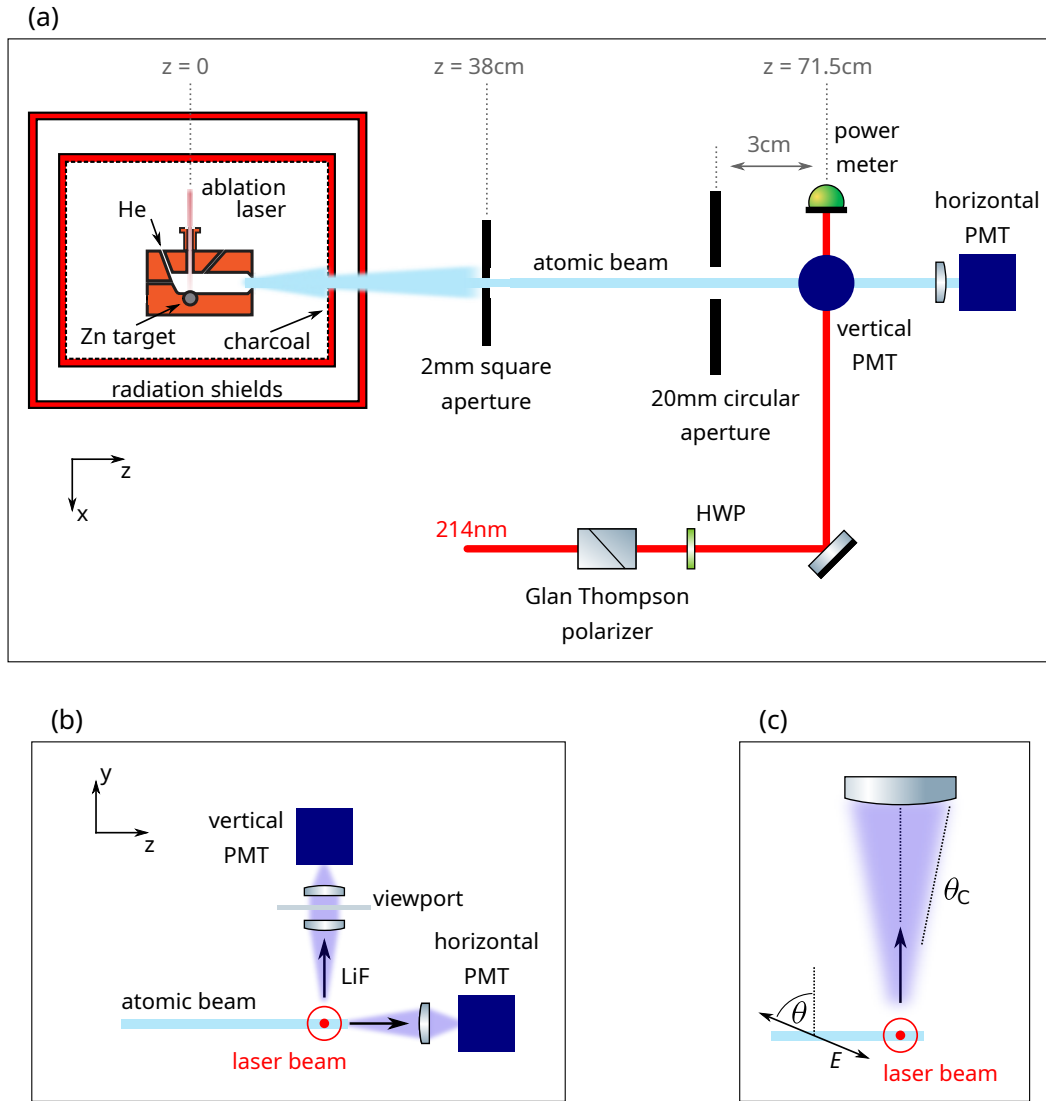


Figure 4.1: (a): Sketch of the buffer gas cooled beam source. The Zn atomic beam is generated by an ablation laser pulse in the buffer gas cell and depicted in light cyan, while the laser beam is shown in red. The laser induced fluorescence (LiF) is collected with photomultipliers (PMT) in two orthogonal directions to the laser beam. (b): LiF collection apparatus including the lens systems. (c): θ denotes the angle between detection direction and laser polarization, while θ_C denotes the solid angle of LiF collection. The figures are adapted from Refs. [34, 117, 118] and Sid C. Wright.

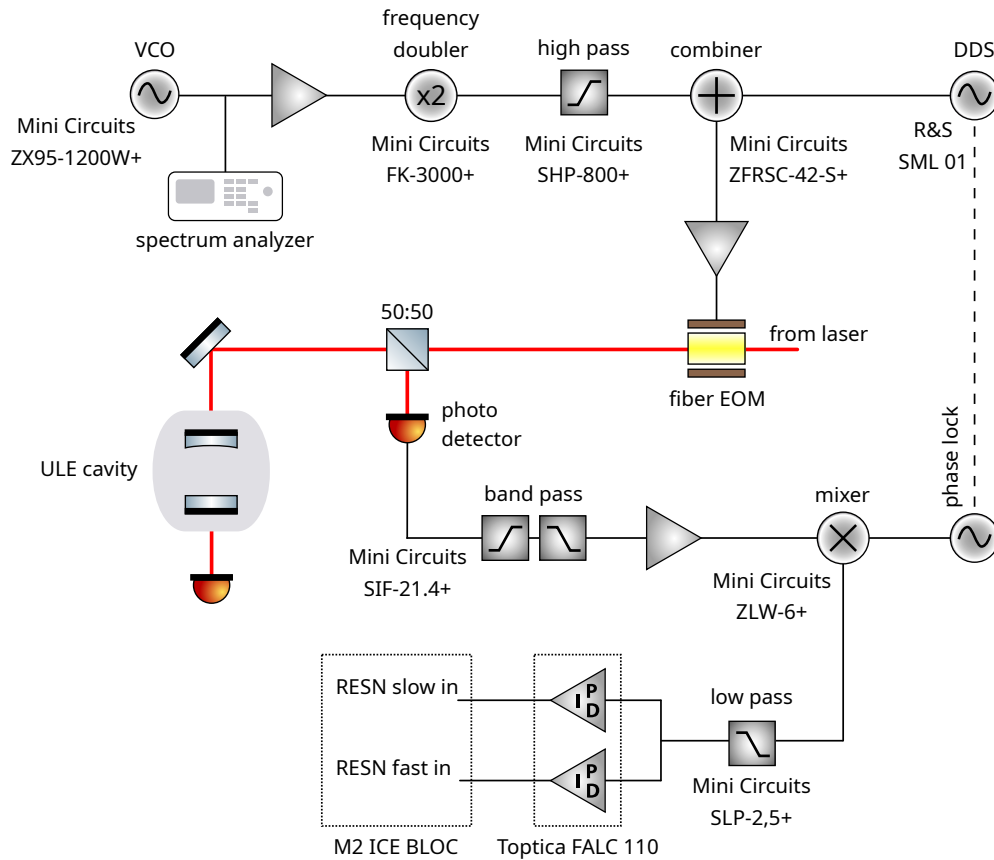


Figure 4.2: Laser frequency stabilization setup. A frequency-doubled, voltage-controlled oscillator (VCO) generates the carrier shift frequency for scanning the laser with respect to the ULE cavity. A direct digital synthesis (DDS) generator provides the locking sidebands for the Pound-Drever-Hall lock. An identical generator, phase-locked to the latter one, is used for demodulation of the photo detector (PD) signal. The signal is filtered by a servo-controller and split into a fast and a slow feedback circuit, which is applied to the respective inputs of the laser controller.

4.3 Measurements and results

During the measurement campaign, several traces of the entire Zn spectrum have been obtained. One scan with horizontal and one with vertical polarization have been performed with a wavemeter serving as the frequency reference⁵. This data has been used to determine the absolute frequency of ^{64}Zn as well as the hyperfine coefficients of ^{67}Zn to $A = (20 \pm 2)$ MHz and $B = (10 \pm 5)$ MHz. Further, the solid angles of the PMT detection are extracted by the lineshape of the fermionic isotope (see Eq. (3.28)). These wavemeter traces are depicted in Fig. 4.3, illustrating the different spatial emission pattern of bosonic and fermionic isotopes and the quantum interference of ^{67}Zn .

To determine the isotope shifts with high accuracy, one trace has been taken with the laser locked to the ULE cavity. The resonance of ^{66}Zn is located at a carrier shift frequency corresponding to $\Delta\nu_{\text{FSR}}/2$, where the locking method fails. Thus, a separate trace for ^{66}Zn has been acquired with an

⁵ High Finesse WS8-10, specified to 20 MHz accuracy and 0.4 MHz measurement resolution [117]

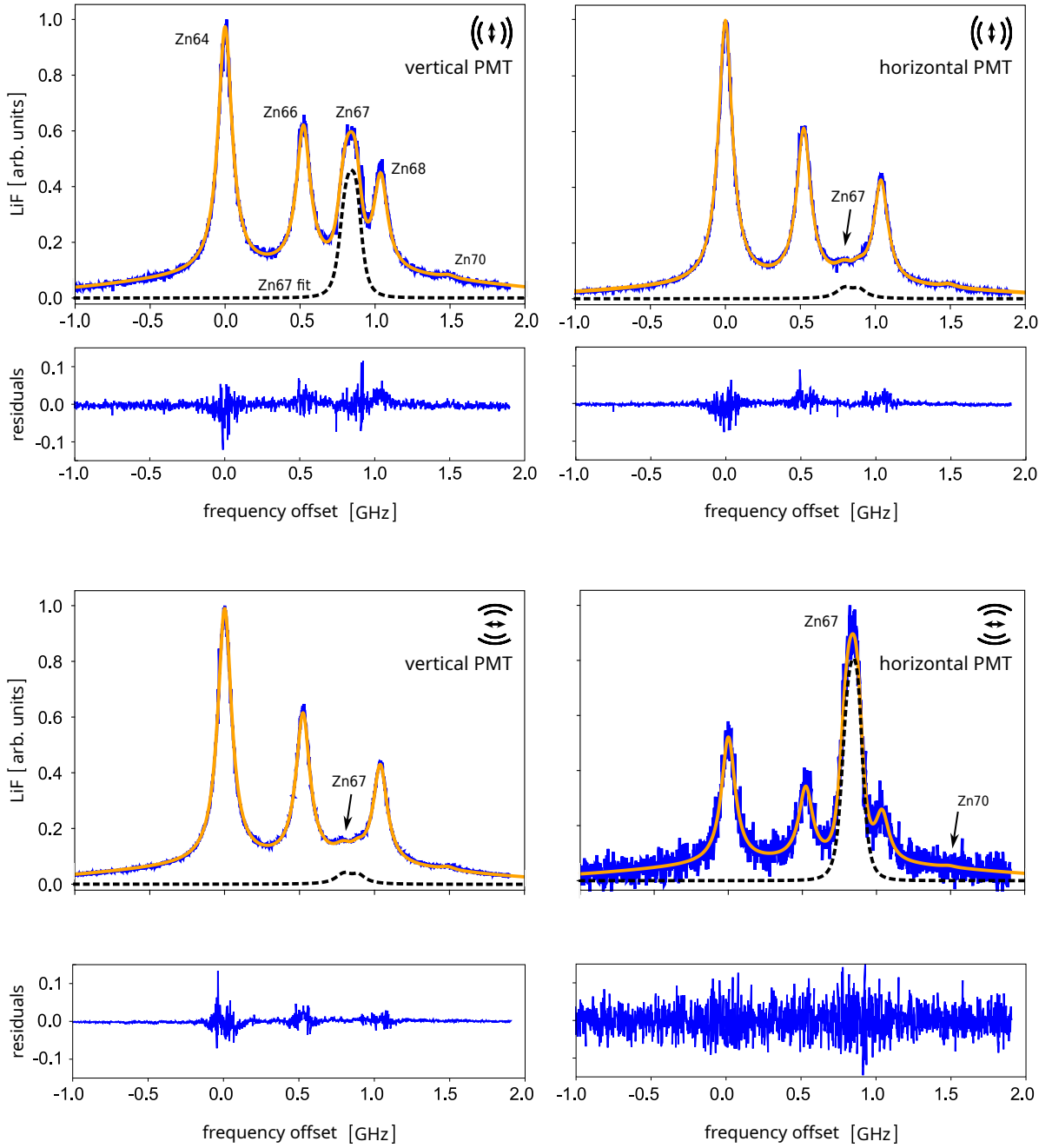


Figure 4.3: Fluorescence measurements with the wavemeter as frequency reference. In the top row, the trace for vertical polarization is shown, while the trace for horizontal polarization is shown in the bottom row. The figure illustrates the spatial emission pattern for fermionic and bosonic isotopes. This figure is adapted from Ref. [34].

acousto-optic modulator shifting the lock frequency of the fundamental.

The results are summarized in Table 4.1. A King plot analysis with available data on the 3P_1 intercombination line at 308 nm [113] is depicted in Fig. 4.4. The respective King plot shows linearity, which is expected for the measurements with MHz-precision (see Section 3.2).

In conclusion, the isotope shift between adjacent bosonic isotopes is around 500 MHz, corresponding to a little less than five linewidths. For the fermionic isotope, the hyperfine coefficients A and B are much smaller than the linewidth itself, which may be beneficial for magneto-optical trapping, as shown in Refs. [115, 116]. The line's center-of-gravity is around three linewidths detuned from the adjacent ^{66}Zn . In general, the isotope shifts are large enough that a magneto-optical-trap operates isotope selectively for all isotopes. The natural linewidth of 111 MHz is large compared to the laser linewidth of the laser presented in Section 2.4.1. As the wavemeter⁶ available in this research group in Bonn provides 5 MHz absolute accuracy, it may serve as a frequency reference regarding laser cooling.

Table 4.1: Results of the 214 nm spectroscopy. All values are given in MHz unless stated otherwise.

quantity	this work	literature
$\nu_{66} - \nu_{64}$	525.0 ± 3.0	480 ± 60 [19] 540 ± 60 [20]
$\nu_{67}^{(\text{CG})} - \nu_{64}$	835.0 ± 5.0	
$\nu_{68} - \nu_{64}$	1039.8 ± 1.7	989 ± 60 [19] 960 ± 85 [20]
$\nu_{70} - \nu_{64}$	1495.0 ± 4.0	
$A(^{67}\text{Zn})$	20 ± 2	17.7 ± 0.5 [129]
$B(^{67}\text{Zn})$	10 ± 5	
$\nu_{64} [\text{cm}^{-1}]$	$46\,745.394 \pm 0.002$	
$\bar{\nu}(^1S_0 \rightarrow ^1P_1) [\text{cm}^{-1}]$	$46\,745.407 \pm 0.002$	$46\,745.404 \pm 0.002$ [55]
$\tau [\text{ns}]$	1.440 ± 0.018	1.40 ± 0.03 [130]

⁶ High Finesse WS-8-5

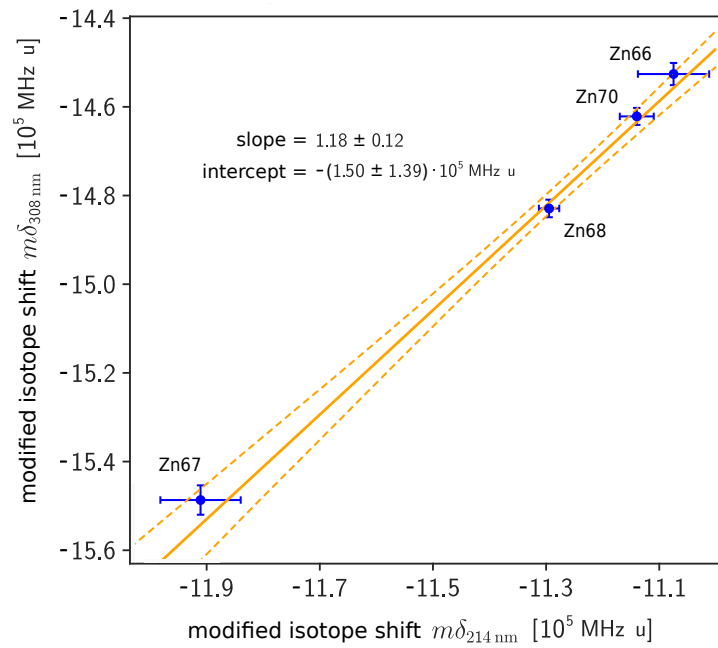


Figure 4.4: King plot analysis with the data reported on the intercombination line in Ref. [113]. The figure is adapted from Ref. [34].

Isotope shift measurement of the $^1S_0 \rightarrow ^1P_1$ transition in calcium

Following the successful hyperfine structure and isotope shift measurements on the main cooling transition, a detailed investigation is conducted by exploring the benefits and limits of saturated absorption spectroscopy. Therefore, isotope shifts are measured on the $(4s^2)^1S_0 \rightarrow (4s4p)^1P_1$ transition in calcium (Ca), featuring a transition wavelength of 423 nm and a natural linewidth of (34.5 ± 0.5) MHz [131]. On one side, the study aims for identifying parameters, which maximize the signal-to-noise ratio and enhance the signal itself. This includes not only aspects from atomic physics, but also technical matters, *e.g.*, the choice of photodiodes and photodiode amplifiers, laser intensities and beam diameters. On the other side, systematic effects like residual Doppler shifts, collisional effects and light pressure-induced distortions of the Maxwell-Boltzmann distribution are characterized.

The findings from this study can be directly applied to spectroscopy on the narrow intercombination lines in Zn and Ca. Especially for the narrow transitions, careful evaluation of methodical errors is needed, as, *e.g.*, collisions may change the shape of a Lamb dip and can influence its amplitude and even lead to its disappearance. Further, the goal is to achieve a measurement precision in the 10 kHz regime. Ca is an ideal test candidate for this study, as it features a natural abundance of isotopes without hyperfine structure between 97 % and 0.004 % [50] as shown in Table 5.1. Thus, the experiment is optimized for the detection of signals from isotopes with low abundance.

Table 5.1: Natural abundances for the bosonic isotopes of Ca in % [50].

isotope	^{40}Ca	^{42}Ca	^{44}Ca	^{46}Ca	^{48}Ca
abundance	96.941	0.647	2.086	0.004	0.187

In general, saturated absorption spectroscopy is susceptible to systematic errors due to high cell temperatures, the large thermal velocity of atoms, magnetic fields, *e.g.*, from heating wires, and the relatively large pressure of ambient buffer gas. Further, the shot noise limit can be three to four orders of magnitude higher for saturated absorption spectroscopy than for fluorescence measurements [36], since it measures the transmission of a relatively intense laser beam. There have been previous

measurements on the respective transition [131–133], the most precise among them rely on fluorescence measurements [131] or ionization spectroscopy [132].

However, the large transition linewidth, a vast vapor cell geometry and previous work on Ca-Ar collisions allow the precise characterization of systematic errors in saturated absorption measurements, as discussed in the following. Hence, in this work, the isotope shifts of the four most abundant bosonic isotopes, ^{40}Ca , ^{42}Ca , ^{44}Ca and ^{48}Ca are measured with superior precision.

The content of this chapter has been published in Ref. [35] The full citation reads

David Röser, Lukas Möller, Hans Keßler, and Simon Stellmer
Isotope Shift Measurements of the 423-nm line in Ca,
Phys. Rev. A **110** (2024) 032809

This chapter summarizes the publication, which is reprinted in Appendix B. **The author of this thesis contributed to the publication by developing the idea of performing this study and the measurement plan. Further, the author constructed and optimized the setup¹, identified systematic errors, devised appropriate corrections and workarounds and conducted the data analysis. Additionally, the writing process was completed primarily by the author².**

5.1 Experimental apparatus

The laser source is based on a diode laser with built-in tapered amplifier³ at 846 nm, which is externally frequency doubled in a SHG cavity operating with an LBO crystal⁴. The SHG cavity resonance is stabilized to the laser with a Hänsch-Couillaud lock. A sketch of the setup is shown in Fig. 5.1 (a).

The laser undergoes a carrier shift modulation and one sideband is frequency stabilized with a Pound-Drever-Hall locking scheme to a ULE cavity⁵ [128]. The carrier shift is derived from the radio frequency signal of a direct digital synthesis generator⁶. The signal is frequency quadrupled, as the generator is limited in frequency to a maximum around 400 MHz. The first doubling is performed by mixing and subsequent high-pass filtering two phase-locked DDS channels. The advantage of using a mixer is to generate less pronounced harmonics of the fundamental frequency. The second doubling is performed by a frequency doubler⁷ operating in the appropriate frequency regime. The lock setup is depicted in Fig. 5.1 (b).

Saturated absorption spectroscopy is performed by sending two laser beams counterpropagating through a vapor cell [24]. The cell is kept at 340 °C to maintain a partial Ca pressure of around 10^{-7} mbar. The laser beams are equal in intensity, corresponding to 1.9 mW on a beam diameter of 4 mm. To actively stabilize the intensity, the power is monitored with a photo detector⁸ and feedback

¹ along with Lukas Möller

² All co-authors have agreed to this description of my personal contribution.

³ Toptica TA pro

⁴ Agile Optic SHG resonator from IR to VIS, identical to the resonator described in Section 2.4.1

⁵ Menlo ORS-Cubic, same cavity as in Chapter 4

⁶ ARTIQ Urukul

⁷ Mini Circuits FK-3000+

⁸ Thorlabs SM05PD3A with FEMTO DHPA-100 transimpedance amplifier

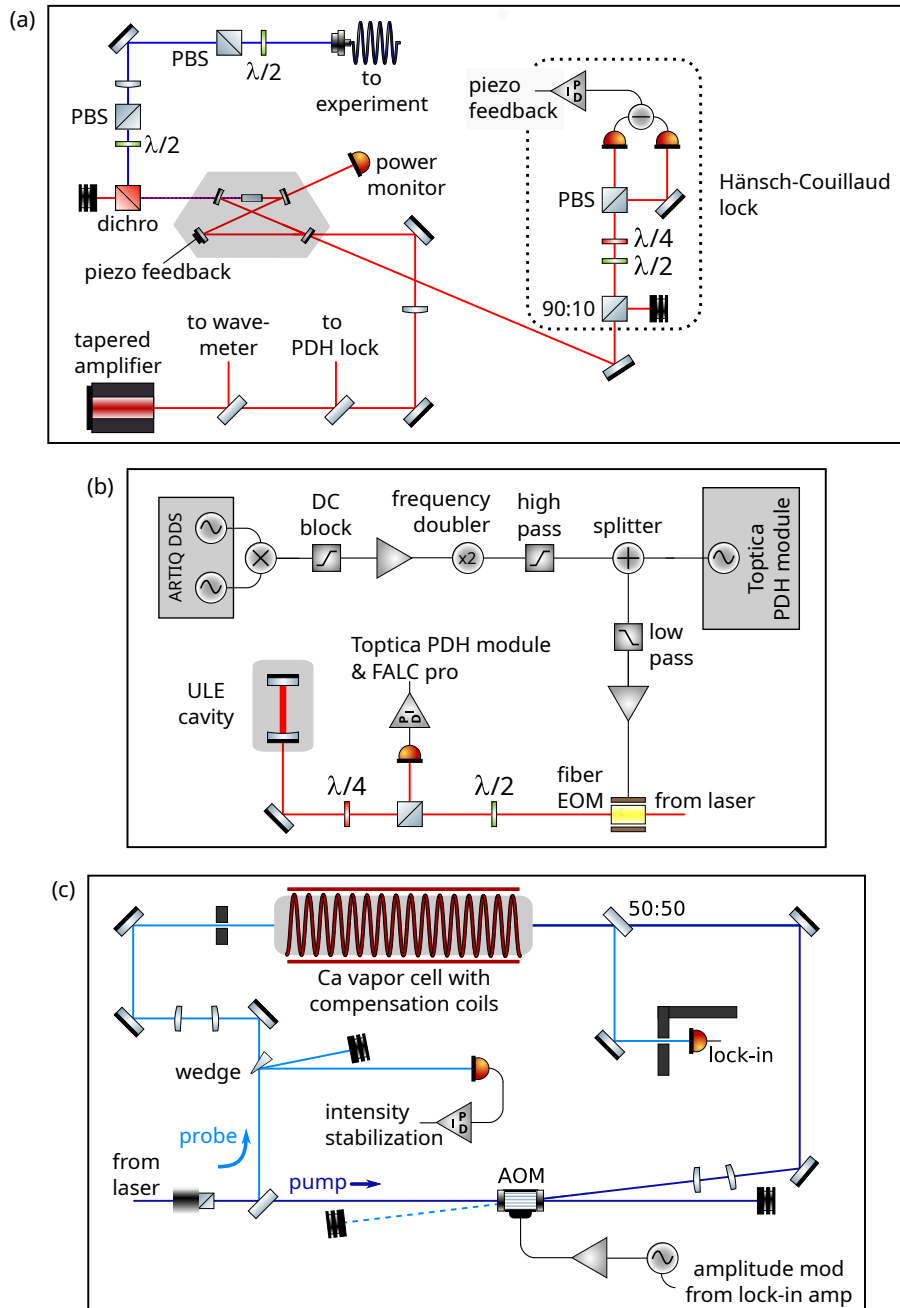


Figure 5.1: (a): Frequency-doubled laser system. The length of the SHG cavity is stabilized to the laser by a Hänsch-Couillaud locking scheme. (b): Setup of the Pound-Drever-Hall lock for frequency stabilization of the laser to a ULE cavity. (c): Setup for saturated absorption spectroscopy. The figure is adapted from Ref. [35].

on the tapered amplifier current is applied via a servo controller⁹ with 10 MHz bandwidth. Further, noise is reduced with the lock-in technique by sinusoidally varying the power in the pump beam with an AOM. The power of the probe beam, transmitted through the cell, is measured¹⁰ and demodulated by a lock-in amplifier¹¹.

5.2 Measurements

To measure the isotope shift for an isotope i , traces of ^{40}Ca and i are taken immediately following after each other. Each trace contains two scans in opposite directions to confirm that there are no shifts due to a too tight low pass filtering of the lock-in amplifier. Subsequently, the respective line centers are averaged. By subtracting the average for isotope i from the average of ^{40}Ca , determined from a previous trace, the isotope shift is extracted. This procedure is repeated to acquire more measurements. As each trace takes around 2 h, errors from drifts of the ULE cavity resonance are negligibly small. Single scans for each isotopes are depicted in Fig. 5.2.

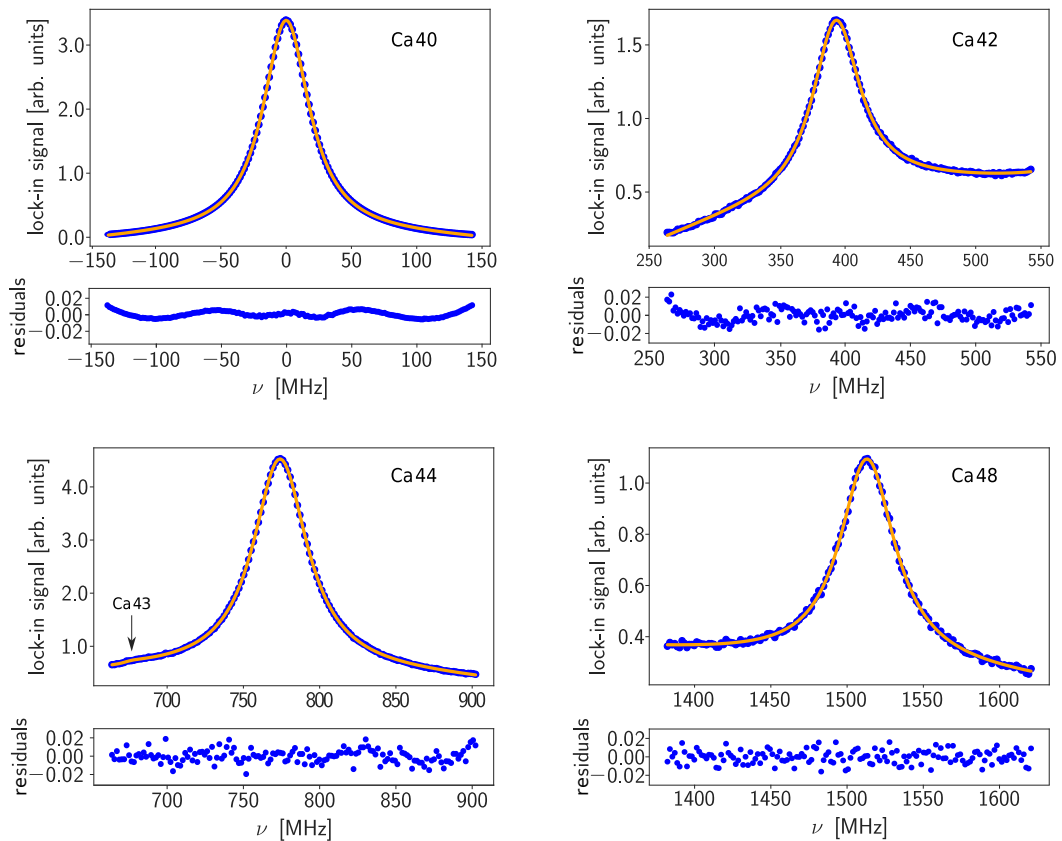


Figure 5.2: Single scans of all measured isotopes including the line fit and residuals. The figure is adapted from Ref. [35].

⁹ Vescent Photonics D2-125

¹⁰ Thorlabs SM05PD3A with FEMTO DHPA-100 transimpedance amplifier

¹¹ Zurich Instruments HF2LI

The measured isotope shifts are subject to the following systematic errors, which have to be taken into account:

Velocity distribution

Resonant laser light induces a distortion in the Maxwell-Boltzmann distribution by transferring momentum on the atoms. This modifies the undisturbed Lorentzian shape by adding a dispersive term to the observed lineshape [134–136]. This effect has been overcome by filling the cell with an Ar buffer gas, restoring the Boltzmann distribution by collisions. Further, the net photon recoil has been minimized by ensuring equal intensity in pump and probe beam.

Power dependent shift

The resonance frequencies of all isotopes have been observed using different laser powers. From these measurements, a power shift coefficient has been extracted to extrapolate the observed resonance frequencies to zero light power. A possible origin might be an imperfect restoring of the Maxwell-Boltzmann distribution. The sensitivity of this line to AC Stark shifts is calculated to be 35 mHz/cm^2 , using all dipole-allowed transitions listed in the NIST atomic spectra database [137]. Comparing this with the measurement uncertainty, AC Stark shifts cannot be detected in this measurement.

Atomic recoil

The atomic recoil leads to a splitting of the Lamb dip in two components. One component corresponds to the absorption resonance of the ground state atoms and the other one to the emission of excited state atoms. The splitting is not resolved in this measurement, as the natural linewidth is much larger than the splitting. Calculating the splitting according to Ref. [138], possible errors on the isotope shift measurement are on the kHz-scale and thus negligibly contribute to the overall uncertainty of the measurement.

Collisions

Collisions between atoms cause a line broadening and a shift [139–142]. While the line broadening is insignificant for this measurement, the shift has to be corrected for. The shift parameter for Ca-Ar collisions has been measured in [143] and the correction can be calculated according to the Ar pressure in the gas cell. Due to the low partial pressure of Ca, Ca-Ca collisions are considered as insignificant, as line center shifts are insignificant compared to the overall measurement uncertainty.

However, it has been shown that collisions alter the atomic lineshape leading to modified Lorentzian lineshape due to the finite collision time T_d [144]. The impact approximation loses validity, as it requires $T_d \cdot \Delta \ll 1$ with the detuning $\Delta = \nu - \nu_0$. The fit function in the presence of collisions can be obtained from Ref. [144–148] and reads

$$I(\Delta) \propto \frac{\gamma_N + \gamma_c(\Delta)}{\Delta^2 + [\gamma_N + \gamma_c(0)]^2} \quad (5.1)$$

with

$$\gamma_c(\Delta) = \gamma_c(0) \cdot (1 + a_1 \Delta T_d) . \quad (5.2)$$

Here, γ_N denotes the natural linewidth, a_1 a potential-dependent parameter, and $\gamma_c(0)$ the collisional broadening from the impact approximation.

Doppler shift

Residual Doppler shifts might originate, if pump and probe beam are not perfectly aligned anti-parallel [149]. From their geometrical overlap and considering the velocity distribution for the respective isotopes, possible Doppler shifts are accounted for by adding a 10 kHz error to the uncertainty budget.

Polarization dependent effects

Effects due to the light's polarization are minimized by ensuring a clean linear polarization in the vapor cell. The polarization extinction ratio is measured with a polarimeter to be larger than 30 dB before and 25 dB after the cell. Further, the magnetic field inside the vapor cell is balanced by compensation coils in all directions. The residual magnetic field strength is measured in the cell and is well below 5 μ T and hence negligibly contributes to Zeeman shifts [131].

5.3 Results

The measured isotope shifts are displayed in Table 5.2 and are in good agreement with Ref. [131]. However, comparing to Ref. [132], there is a discrepancy for ^{42}Ca . In Ref. [132], the resonances of ^{43}Ca were considered as insignificant and not taken into account for fitting. This contributes to a fit error, as the resonance of ^{42}Ca lies on the wing of ^{43}Ca . The uncertainty budget obtained in this work is a factor of about five lower compared to Ref. [131] and a factor of about three lower compared to Ref. [132], as displayed in Table 5.3.

A King plot analysis has been performed by relating this measurement to the high precision data of Ref. [21]. The King plot, displayed in Fig. 5.3, reveals excellent linearity confirming the consistency of our data.

Analyzing the signal-to-noise ratio, isotopes with an abundance of around 0.01 % might have been detected with a signal-to-noise ratio of one. Relating this to the linewidth governing the absorption cross section, a transition with a linewidth in the 10 kHz regime might have been the detection limit for an abundance of 100 %.

Table 5.2: Measured isotope shifts for the $(4s^2)^1S_0 \rightarrow (4s4p)^1P_1$ line in Ca in comparison to previously reported values. All values are in MHz.

isotope	this work	[131]	[132]
^{42}Ca	393.09 ± 0.09	393.1 ± 0.4	393.50 ± 0.10
^{44}Ca	773.81 ± 0.05	773.8 ± 0.2	773.80 ± 0.15
^{48}Ca	1512.99 ± 0.07	1513.1 ± 0.4	1513.00 ± 0.20

Table 5.3: Corrections and uncertainties of the isotope shift measurement, exemplified for ^{42}Ca . All values are in kHz.

source	correction	uncertainty
residual Doppler	0	10
second-order Doppler	0.2	0
atomic recoil	0	1
power dependence	0.7	0
Zeeman effect	0	0
collisions	37	0.3
cavity drift	0	1
statistical error	0	85

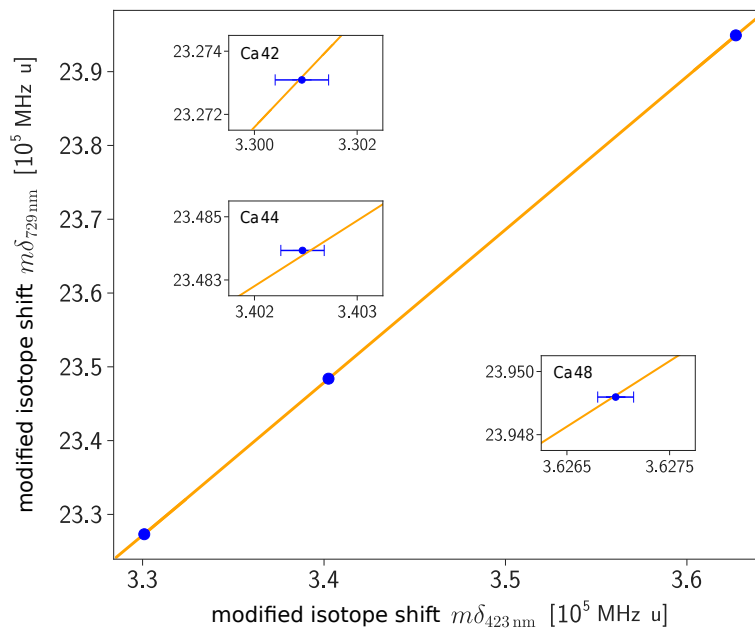


Figure 5.3: King plot with measured isotope shifts from this measurement and from Ref. [21]. The errors from Ref. [21] are too small to be visible as errorbars. The figure is adapted from Ref. [35].

Outlook: Spectroscopy of the $^1S_0 \rightarrow ^3P_1$ transition and towards laser cooling of zinc

Having characterized the main cooling transition in Zn and having characterized systematics in saturated absorption spectroscopy, the hyperfine structure and isotope shifts of the $(4s^2) ^1S_0 \rightarrow (4s4p) ^3P_1$ are going to be measured. To do so, a measurement setup has been designed, which is shown in Section 6.1. The actual measurement is beyond the scope of this thesis. Furthermore, a setup for magneto-optical trapping of Zn has been designed and constructed, which is presented in Section 6.2. Trapping will be attempted in future, when sufficient laser power at 214 nm is available.

6.1 Hyperfine structure and isotope shifts on the $^1S_0 \rightarrow ^3P_1$ transition in zinc

For spectroscopy on narrow lines, fluorescence detection can be advantageous to direct absorption measurements. As the absorption coefficient scales linear with the transition linewidth, absorption of a laser in a vapor cell is reduced. Furthermore, the atom's angular momentum distribution is spread over 4π solid angle. The share of atoms contributing to a Lamb dip depends on Γ , as the condition $\vec{k} \cdot \vec{v} \lesssim \Gamma/2$ needs to be fulfilled. Hence, in saturated absorption spectroscopy, the Zn vapor pressure for transitions with kHz-linewidth needs to be orders-of-magnitude larger compared to transitions with MHz-linewidth. Then, the evaluation of collisional effects has to be performed very carefully, as self-collisions have to be taken into account. The governing potential is given by a dipole-dipole potential with a long-range R^{-3} dependence [150]. Hence, their influence can be significant, although the partial pressure of the atoms may be much lower than the buffer gas pressure. Zn-noble gas collisions are governed by a Lennard-Jones potential, which decays as R^{-6} for large R [150].

Fluorescence spectroscopy benefits from the background-free detection and the high detection efficiency of photomultipliers (PMTs). Hence, the number of absorbers/emitters may be significantly lower than in absorption measurements. In trapped atom/ion experiments, the fluorescence of a single emitter can be collected and used for analysis with appropriate integration time [36, 140]. This allows to perform spectroscopy, *e.g.*, on atomic beams with a typical atom flux of up to 10^{15} atoms per second. In such experiments, the influence self-collisions is minimized due to low atomic densities in the beam. Furthermore, a buffer gas is avoided to maintain the collimation of the beam, making

Zn-background gas collisions negligible. Residual first order Doppler broadening due to imperfect atomic beam collimation can be eliminated sending counterpropagating laser beams orthogonally through the atomic beam. The fluorescence power, measured by the PMT, follows a saturation signal [40]. Different lock-in detection schemes can be applied and examined for the best signal-to-noise ratio and precision. One way is the measurement of intermodulated fluorescence, in which the intensity of the counterpropagating laser beams is modulated with different frequencies. The obtained signal is then demodulated with the sum frequency. This removes unwanted background signals and only the saturation signal remains [140]. Furthermore, detection schemes have been proposed in Ref. [151], offering the observed linewidths to be below the natural linewidth. To exploit these advantages for the Zn spectroscopy, a fluorescence spectroscopy experiment on a Zn beam including a frequency reference cavity has been designed, which is discussed in the following.

6.1.1 Design and construction of a frequency reference cavity

Commonly, frequency reference cavities consist of two highly reflective mirrors, which are optically contacted to a spacer. For having the cavity's resonance frequency as stable as possible, changes in the effective cavity length have to be avoided: For thermal stability, the spacer is made of a material with a low coefficient of thermal expansion (CTE)¹. Mirror substrates are mostly from fused silica and the CTE mismatch between ULE glass and fused silica may lead to an effective CTE, which is different from ULE. This can be compensated by contacting ULE rings to the mirror backsides [152, and Refs. therein]. Further, the cavity is placed in vacuum, also preventing refractive index fluctuations of ambient air. Minimizing the vibration sensitivity is achieved by choosing optimal support points. Therefore, the mirror distance change is simulated under influence of gravitational acceleration and the points of minimal length change are chosen. To avoid mechanical stress, the spacer is laid on its support structure and is typically not clamped [153].

Cavity Design and Construction

Depending on specific requirements, reference cavities have been constructed with various spacer geometries, some of which are shown in Refs. [153–159]. During this work, the spacer design is adapted from Ref. [153] (see Fig. 6.1 (a)), while the support structure and the vacuum system are designed entirely new. For future experiments, this design can be possibly modified such that the cavity is transportable. Therefore, the cavity could be clamped on the 'wings' to restrict any movement.

The spacer is 10 cm long and is fabricated from a single piece of ULE glass². The sides are polished for the optical contact bonding of the mirrors to the spacer. The mirrors consist of a fused silica substrate with dielectric mirror coating on one side and an anti-reflection coating on the other side³. However, it was not possible to contact the ULE rings to the mirror backside, which might be explained by a too large surface roughness or dirt in between the glass surfaces. The mirror performance has been tested with a cavity ring-down measurement [160]. The obtained finesse is $141\,000 \pm 1100$, which corresponds to a cavity linewidth of around 10 kHz. Hence, the linewidth of the cavity resonance is

¹ Typical spacer materials are Corning ULE 7972 and 7973 or Schott ZERODUR.

² Corning ULE 7972

³ substrates and coating from Laseroptik Garbsen,
rms surface roughness < 0.1 nm,
 $R_1 = \infty$, $R_2 = -500$ mm

narrow enough to provide a frequency reference for spectroscopy on transitions with kHz-linewidths [128].

For the design of the support structure, the optimal support points have been determined using finite element simulation⁴ to be $x = 20.8$ mm and $y = 9.3$ mm. The corresponding plot and the definition of the reference frame for x and y are depicted in Fig. 6.1 (b) and (c). The predicted mirror displacement lies within the low 10^{-13} m regime, which is competitive to other designs [156].

For the first test, the support structure has been designed such that the spacer lies on small Viton cylinders on a copper support structure within two copper radiation shields. This system is placed in an indium-sealed vacuum system made of aluminium, which is constantly pumped by a 2 L s^{-1} ion pump⁵. The achieved pressure has been 5×10^{-7} mbar, limited by the low conductance in the vacuum system⁶.

Stabilizing a laser to the cavity with a Pound-Drever-Hall lock [128] and observing the laser frequency with a wavemeter⁷, it has been found that the cavity resonance shifts by 10 MHz within 15 min according to the two-point control of the laboratory air condition. This shift happens in an unexpectedly short time interval and is unexpectedly large, even with the ULE rings not contacted to the mirrors. The frequency drift corresponds to a 4 nm change of the mirror spacing. This change cannot be explained purely by thermal expansion of the spacer: Assuming the CTE of ULE at room temperature to be 30 ppbK^{-1} ⁸, the length change would correspond to a temperature change of the entire cavity spacer of 1°C . This appears unfeasible given the heat shields and the low heat conductivity of glass. Possible origins might be an imperfect optical contact between mirror and spacer, causing additional mirror displacement by thermal stress. Furthermore, the thermal coupling of the cavity to the laboratory environment might be unexpectedly large. Additionally, as no resonance of the 3P_1 transition in Zn has been observed with saturated absorption spectroscopy, it is suspected that the cavity support structure is too vibration sensitive to provide a kHz-stability on the timescale of seconds.

Improved Cavity Support Structure

To address issues listed above, an optimized vacuum system and support structure has been designed, which will be constructed and tested in future. A sketch of the setup is presented in Fig. 6.2 (a).

The vacuum system is made of stainless steel instead of aluminium and features smaller outer dimensions compared to the previous design, as the wall thickness is drastically reduced. Within the vacuum system, there are two copper heat shields with surface roughness below 100 nm ⁹. This minimizes the surface area pointing towards the cavity and thus the power of emitted blackbody radiation. The outer shield one is going to be temperature stabilized with heating wires similarly to Ref. [161]. For this control loop, the temperature is measured with Pt100 sensors and a proportional-integral-derivative controller regulates the electric power sent through the wires. The space between the heat shields is increased, promising a larger pumping speed. To enhance temperature isolation and

⁴ The simulation has been performed with Comsol Multiphysics

⁵ Agilent VacIon 2 l/s pump

⁶ During the writing process of this thesis, the pressure continued to fall with a speed of roughly 0.1×10^{-7} mbar per month.

⁷ High Finesse WS-8-5 specified to 100 kHz resolution and 5 MHz absolute accuracy

⁸ This coefficient is specified to be $(0 \pm 30) \text{ ppbK}^{-1}$ at room temperature

⁹ For this application, a mirror milling process had to be established by the Feinmechanik-Werkstatt des Physikalischen Instituts.

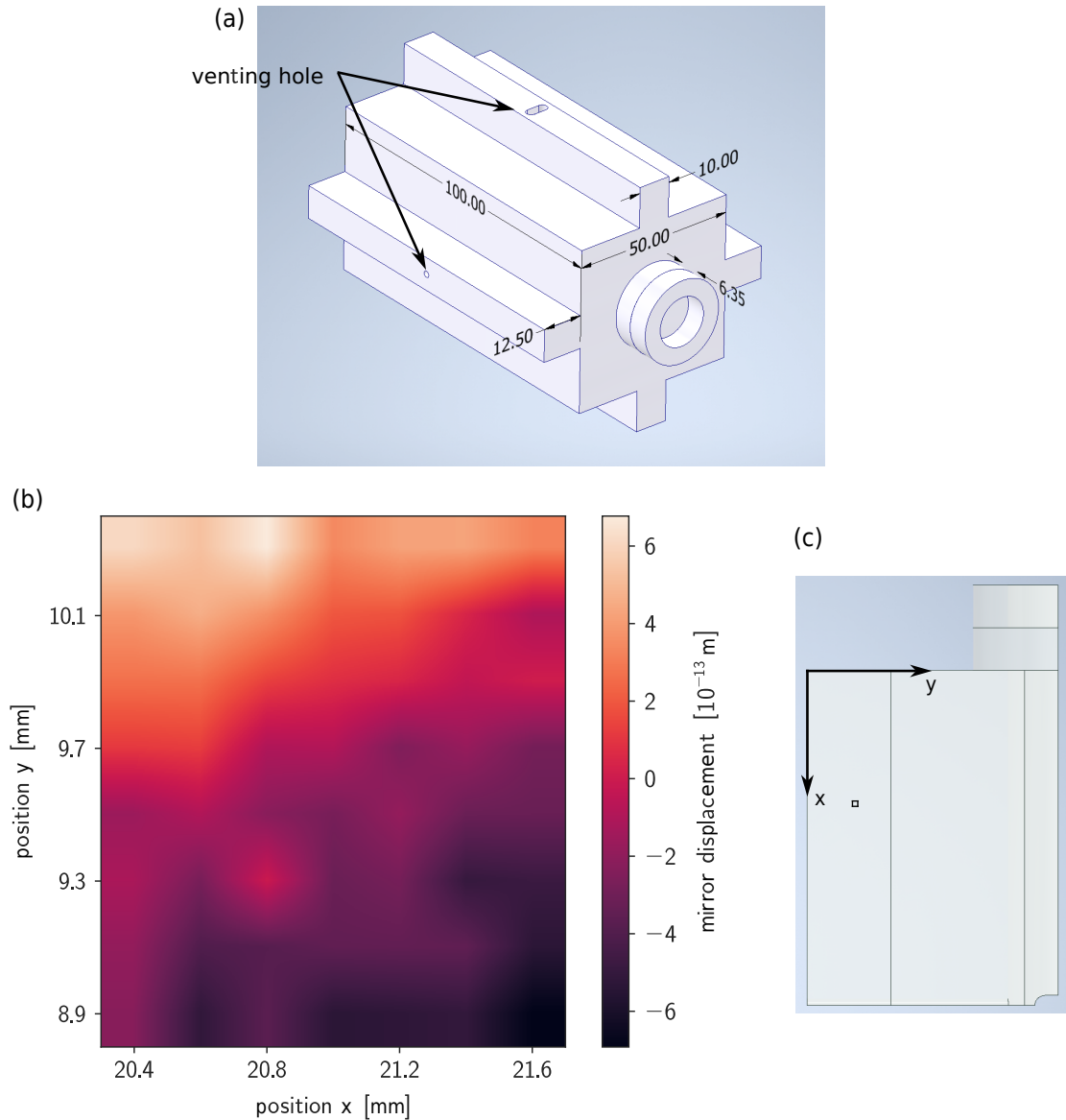


Figure 6.1: (a): Dimensions of the ULE cavity spacer. The mirror dimensions are $\varnothing 25.4 \text{ mm} \times 6.35 \text{ mm}$. All dimensions are given in mm. (b): Simulated mirror center displacement for an automatically optimized mesh by the simulation software. Within the x and y ranges, a point grid with a spacing of 0.2 mm was simulated and linearly interpolated. (c): Definition of the reference frame for x and y . The origin of the coordinate system is located at the outermost corner of the spacer, where the x - and y -axes are intersecting. The little square shows the area shown in (b). Only a quarter of the cavity is shown in top view.

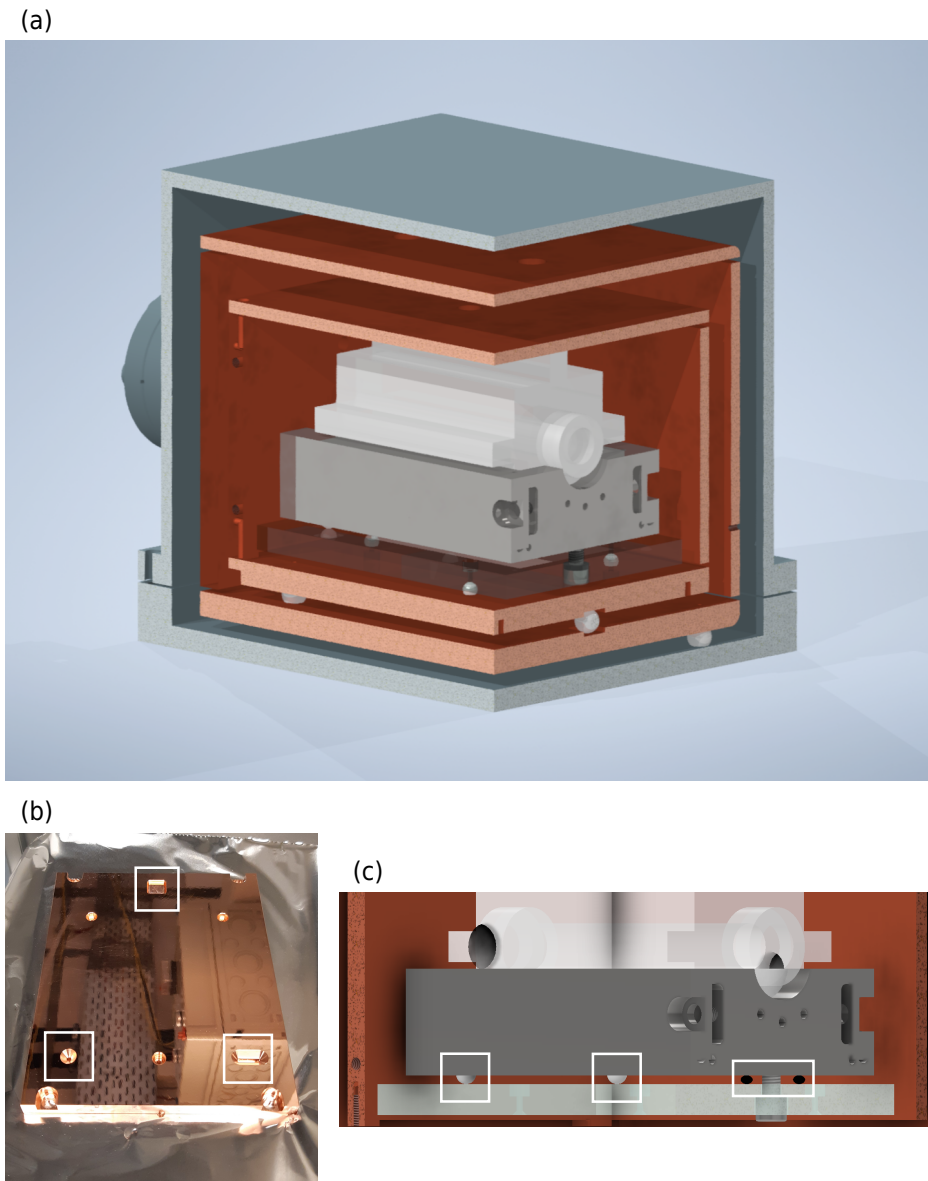


Figure 6.2: (a): Optimized cavity support structure with two copper heat shields and a stainless steel vacuum system. The cavity lies on a stainless steel support structure, which is connected with a self-designed floating bearing to a glass plate. (b): Photograph of the guide rails for the glass spheres between outer and inner heat shield. While the bottom left support point constrains translational movement, the bottom right constrains rotations while leaving space for thermal expansion. The support point on the top does not constrain any movement. Due to the high surface quality, the copper is highly reflective. (c): Between support structure and glass plate, two Viton spheres are placed, which are marked in white. A screw keeps the two spheres under light pressure such that the support structure is weakly allowed to move. At the other support points, the structure lies on glass spheres, which are allowed to freely move.

to absorb vibrations, the outer shield is placed on large PTFE spheres. The inner shield is separated from the outer one by glass spheres positioned within guide rails, as shown in Fig. 6.2 (b). This ensures that each degree of motion is constrained precisely once, avoiding stress between the shields. Glass is preferred over PTFE in this application due to its dimensional stability. Within the inner shield, the cavity support structure is mounted on a borosilicate glass plate¹⁰ to reduce thermal coupling towards the outside and thus improve thermal stabilization. The cavity's support structure is made from thick stainless steel plates to provide enhanced stability. The structure is connected to the glass plate via a self-designed floating bearing, which further reduces vibration transfer to the cavity, as depicted in Fig. 6.2 (c). For the final stage of vibration absorption, the cavity itself rests on small Viton pads placed on the support structure.

The new design is designed to provide significantly increased thermal and vibrational stability compared to the first test setup. With contacting the ULE rings to the cavity mirrors, this design offers a promising starting point for a fully functioning frequency reference for narrow line spectroscopy.

6.1.2 Fluorescence spectroscopy setup

The CAD design of the fluorescence setup is depicted in Fig. 6.3. The main components for the fluorescence setup are the atom source including the collimators and the excitation and measurement section and are introduced in the following.

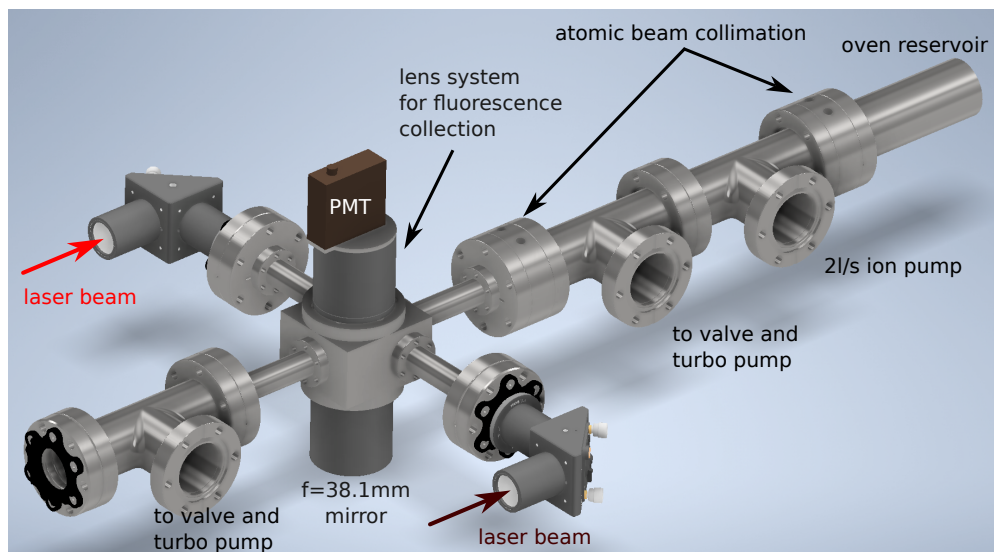


Figure 6.3: Fluorescence spectroscopy setup.

Atomic beam generation

The oven reservoir consists of a small tube section with a CF40 flange, in which Zn can be vaporized with the use of heating tapes. The reservoir is connected to a double-blind flange, with an 1.5 mm aperture, through which atoms are effusing. The aperture is heated with cartridge heaters above the

¹⁰ Borosilicate glass is chosen for its ease of machining with CNC machines using diamond mill heads.

melting temperature of Zn to avoid clogging. A similar collimation stage is located around 30 cm downstream the beam narrowing the transverse velocity distribution. Following Refs. [162, 163], around 10^{13} atoms/s can be expected in the measurement chamber, assuming a reservoir temperature of 350° . The residual transverse Doppler width is calculated to be around 30 MHz. At this level, the Knudsen number is already around one, indicating a transitional flow regime between continuum and free molecular flow. Ref. [163] shows that the number of atoms flowing freely in the atomic beam remain unaffected by the transitional regime. Nevertheless, it might not be possible to increase the atom flux by another order of magnitude.

Measurement chamber

As the atomic beam passes the measurement cell (see Fig. 6.4), the atoms get excited by the laser. The respective viewports are separated from the chamber by CF16 extension tubes to avoid scattered light from the windows on the PMT. 15 mm downstream the atomic beam, a 2 inch collection lens is located outside the vacuum, 37 mm away from the beam, before the light is focused on the PMT¹¹ by an additional lens. Opposing the PMT, a concave mirror with $f = 38.1$ mm is placed to enhance the fluorescence collection efficiency.

As in Ref. [51] a good agreement between the calculated fluorescence intensity and the experiment has been found, this work follows this particular reference in calculating the fluorescence yield. The Rabi frequency has been calculated with

$$\Omega_R = \sqrt{\frac{I}{I_{\text{sat}}}} \cdot \Gamma / \sqrt{2} \quad (6.1)$$

and the effective Rabi frequency is given by

$$\Omega_{\text{eff}} = \sqrt{\Omega_R^2 + \Delta^2}, \quad (6.2)$$

where Δ denotes the detuning, I is the light intensity, I_{sat} the saturation intensity and $\Gamma = 2\pi \Delta\nu$ the linewidth of the transition. The probability of finding an atom in the excited state is given by

$$e = \frac{\Omega_R^2}{\Omega_{\text{eff}}^2} \sin^2(\tau \Omega_{\text{eff}}) \quad (6.3)$$

with the approximation that the interaction time τ is given by $\tau = 2w_0/v$. Here, w_0 denotes the laser beam waist and v the atom's velocity. Following the Maxwell-Boltzmann distribution for the forward velocity¹², a distribution of interaction times is calculated. Assuming a laser power of 10 mW/cm^2 , it is found that the excitation probability is $p = 0.008$ for an atom on resonance. The laser power may be still increased to achieve a higher excitation probability. For estimating the number of collected photons, it is assumed that the atomic beam is characterized by the numbers given above and that only atoms with a Doppler shift smaller than Γ contribute to the signal. The decay of the excited state

¹¹ Hamamatsu H9306-05

¹² The atomic beam actually follows a modified Maxwell-Boltzmann distribution, dependent $v^3 \exp(v^2/\sigma)$, as stated in [162]. Ref. [51] finds that the excitation probability is larger for slow atoms. Hence, a pure Maxwell-Boltzmann distribution describes their experiment more precise and is assumed here.

starts immediately after the excitation and is taken to be exponential governed by the natural linewidth. The time delay between excitation and detection is calculated and the number of photons emitted into the detection system is estimated by the detector's solid angle divided by 4π . This estimation shows that more than 5×10^6 photons are detected for the total number of atoms in the atomic beam. This corresponds to a PMT signal of approx. 500 mV for the most abundant and approx. 10 mV for the least abundant isotope. The PMT's electronic noise floor is specified below 1 mV. Further signal-to-noise enhancement by several orders of magnitude may be achieved with lock-in detection, as described above. This way, a signal-to-noise ratio larger than 100 appears to be possible for the least abundant Zn isotope.

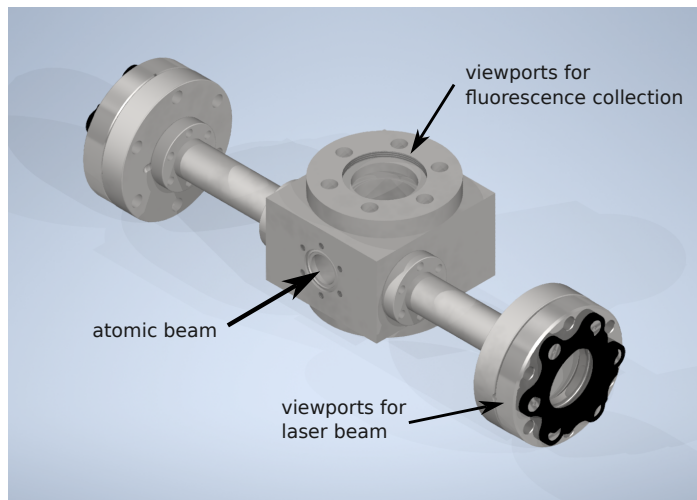


Figure 6.4: Measurement chamber for atom excitation and fluorescence collection.

6.2 Towards magneto-optical trapping of zinc

The foundational step towards a clock operating on Zn is successful laser cooling and magneto-optical trapping, which, to the best of our knowledge, has not been reported in literature yet. The theoretical framework of magneto-optical traps (MOTs) can be found in various references, including Ref. [78]. An experimental setup for the first Zn-based MOT has been constructed, comprising of a vacuum chamber and magnetic field coils. When sufficient laser power becomes available (see Section 2.4.1), this system will be activated. Its design is presented in Fig. 6.5 (a) and is discussed in the following sections.

6.2.1 Vacuum System

The vacuum system is constructed from standard vacuum parts made of stainless steel and is depicted in Fig. 6.5 (b). The magneto-optical trap (MOT) is located at the center point of a CF40 cube, providing optical access along three orthogonal axes for the trap laser beams. The viewports are

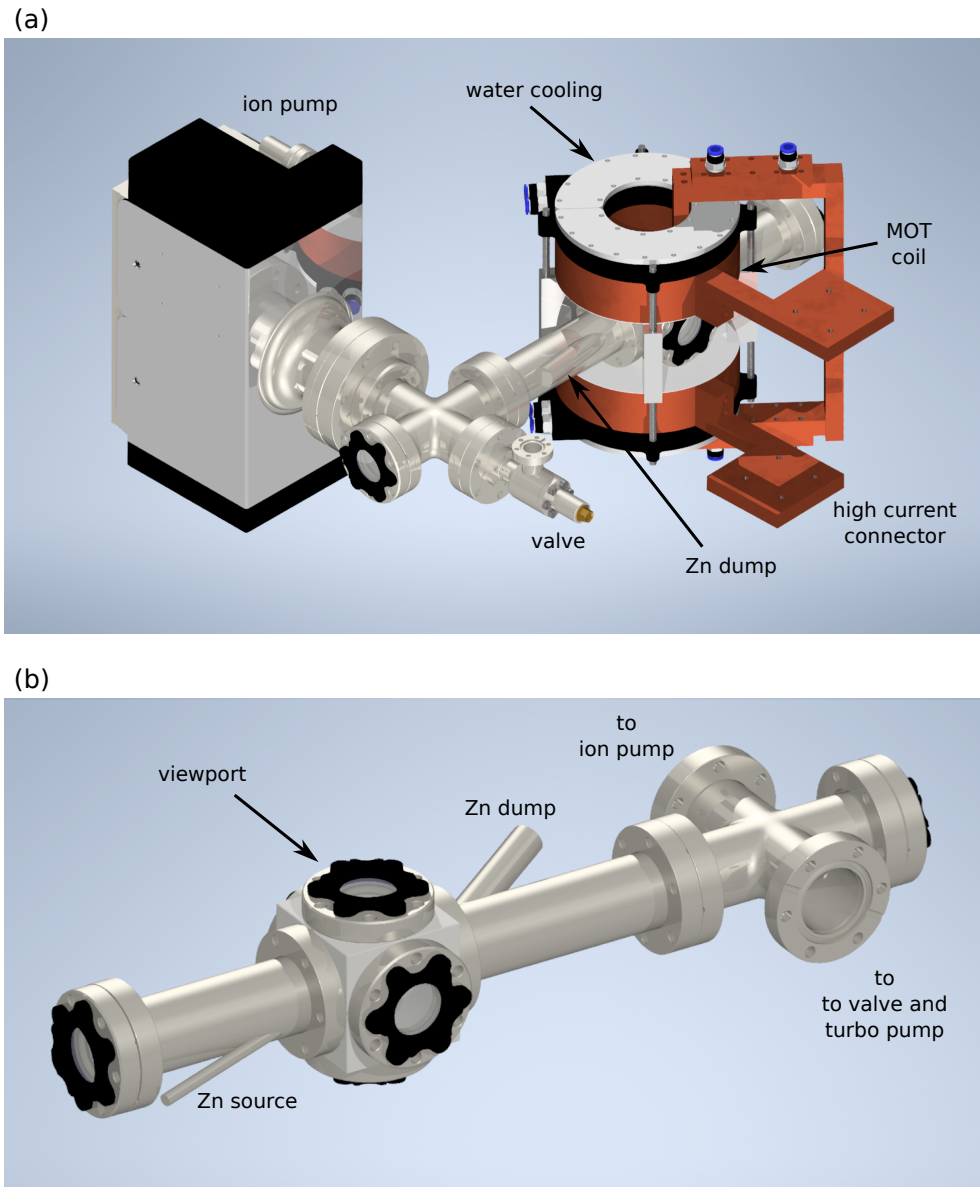


Figure 6.5: (a): CAD drawing of the entire MOT setup including the MOT coils, their watercooling system and the vacuum pumps. (b): Vacuum system used in the MOT setup. The Zn source and the dump are explicitly shown in Fig. 6.6.

commercial flanges with the windows sealed with Viton o-rings¹³. The windows are custom-built¹⁴ from Corning 7980 KrF glass, with dimensions $\varnothing 1.5'' \times 4$ mm, ensuring a line of sight next to the laser beams for MOT fluorescence collection. The vacuum is pumped by a turbo pump and maintained at a background pressure of around 10^{-8} mbar by an ion pump¹⁵. Special components are the atom's source and dump as well as the MOT coils, which are introduced in the following sections.

6.2.2 Atom source and dump

The designs of the Zn source and dump are based on standard CF40 straight connectors and depicted in Fig. 6.6. A small reservoir tube with 5 mm inner diameter contains approximately 15 g of zinc shot¹⁶. The reservoir tube is silver-brazed under an angle of 15° to the straight connector such that it points towards the MOT volume. Silver-brazing is advantageous to welding, as the tubes can be connected under any angle to each other and the braze flows into the system avoiding virtual leaks (see Fig. 6.6 (b)). A high temperature braze has been used so that the tube can be kept at around 400°C to evaporate Zn into the MOT volume. Therefore, a heating cartridge¹⁷ providing 100 W power, can be clamped to the reservoir and isolated by wool. The opening angle of the Zn beam is approximated to be 20° .

Although the atom flow points away from the viewports, the windows could still get coated with Zn scattered from the walls [56]. To minimize the probability of a scattered atom reaching the windows, a Zn dump has been constructed consisting of a tube of 16 mm inner diameter silver-brazed to a CF40 extension tube. The dump's position is chosen such that atoms evaporated from the source head towards the dump and its angle is adapted to simplify the production.

6.2.3 Magneto-optical trap and magnetic field coils

To generate a magnetic field gradient for the MOT, the coil design follows the Anti-Helmholtz configuration, as depicted in Fig. 6.7 (a) and (b). The coils are directly mounted onto the CF40 cube with a PTFE mat providing electrical insulation and feature an inner diameter of 73 mm to allow space for the viewports. They are manufactured by waterjet cutting seven turns, each 5 mm wide with 0.8 mm spacing, from a 4 cm thick rigid copper plate. Four dc power supplies¹⁸, each delivering up to 400 A, are used in parallel to drive the coil system with maximum current of $I = 1600$ A. The low winding number allows faster gradient switching times, which leaves the opportunity to transfer atoms from a broad MOT into a narrow line MOT. However, a suitable ring-down ("snubber") circuit still has to be designed and might be adapted from Ref. [164] for a large current.

For the design work, the gradient has been simulated assuming a uniform current density across the winding cross section. Each macroscopic coil winding is decomposed into 1701 current loops with each of them guiding a current of $I/1701$ using the *magpylib* package for Python [165]. For $I = 800$ A, the gradients were 62 G cm^{-1} in the horizontal and 124 G cm^{-1} in the vertical axes, indicated in Fig. 6.7 (b). After construction of the coil system, the gradients have been measured to be 57 G cm^{-1} and

¹³ Thorlabs VC234

¹⁴ Lens Optics

¹⁵ Agilent Technologies VacIon 55 L s⁻¹ Star Cell

¹⁶ Alfa Aesar, Zinc shot, 1-6 mm, Puratronic, 99.9999 % (metals basis)

¹⁷ HS Heizelemente S/HS-6,5/60/100/24-D

¹⁸ TDK Lambda GEN8-400

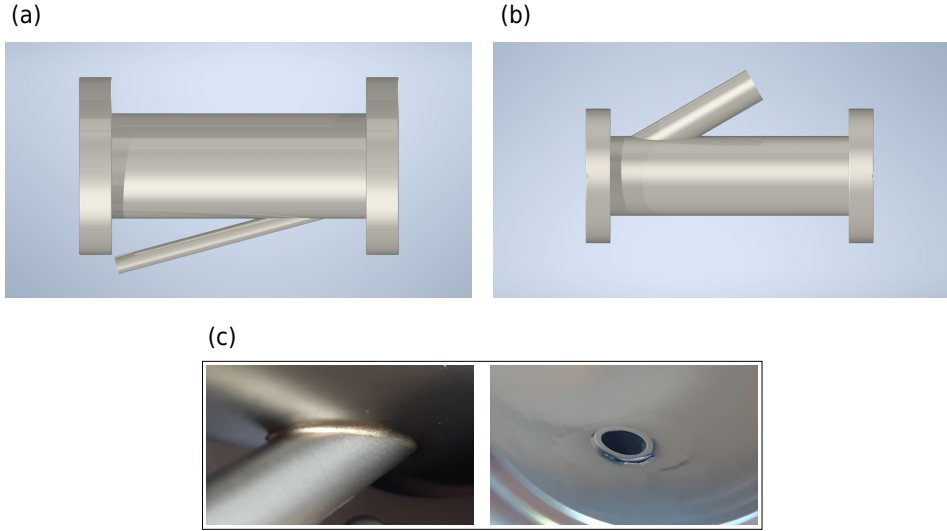


Figure 6.6: (a): CAD drawing of the Zn source. (b): CAD drawing of the Zn dump. (c): Photograph of the joints between the reservoir tube and the CF40 tube depicted from outside of the system (top) and the inside (bottom).

119 G cm^{-1} , as depicted in Fig. 6.7 (c) and (d). The deviation between simulation and measurement is on the percent level and might originate from manufacturing tolerances and the current connectors. As the gradient scales proportional to the current, the measured gradient can be increased by a factor of two.

Based on the internal current and voltage measurement from the power supply, the total resistance of the coil setup is approximated to be $700 \mu\Omega$, which is achieved by maximizing contact surfaces and hence minimizing contact resistances. At $I = 1600 \text{ A}$, the entire coil system heats up with 1.8 kW power. As the coils might heat up the Viton seals in the viewports, watercooling is required. The cooling components are slotted to avoid eddy currents, whenever the B-field gradient is altered and are placed as indicated in Fig. 6.5.

For a vertical gradient at 1600 A , the capture velocity of the MOT has been modeled with the help of the python *PyLCP* package, assuming the cooling force to be quasi-static [166]. For a total power of 50 mW in each MOT beam, a beam radius of $w_0 = 5 \text{ mm}$ and a MOT light detuning of 1.5Γ , this results in a capture velocity of 35 m s^{-1} . This agrees well with an analytical approximation, in which the cooling force is assumed to be maximal throughout the MOT volume and equals $F_c = I \hbar k \Gamma / (2I_{\text{sat}})$. Then, the capture velocity is calculated as

$$v_c = \sqrt{\frac{4F_c w_0}{m_{\text{Zn}}}} \approx 32 \text{ m s}^{-1}, \quad (6.4)$$

where m_{Zn} denotes the mass of the Zn atoms. Comparing to an average atomic velocity of 470 m s^{-1} at $T = 400^\circ \text{C}$, a small, but reasonable amount of atoms might be captured. To further increase the atom number in the trap, a slow atom source would need to be constructed requiring, *e.g.*, a Zeeman slower or a 2D MOT [167].

At the Doppler temperature of around 2.7 mK , the atoms' velocity is around 1 m s^{-1} . Looking

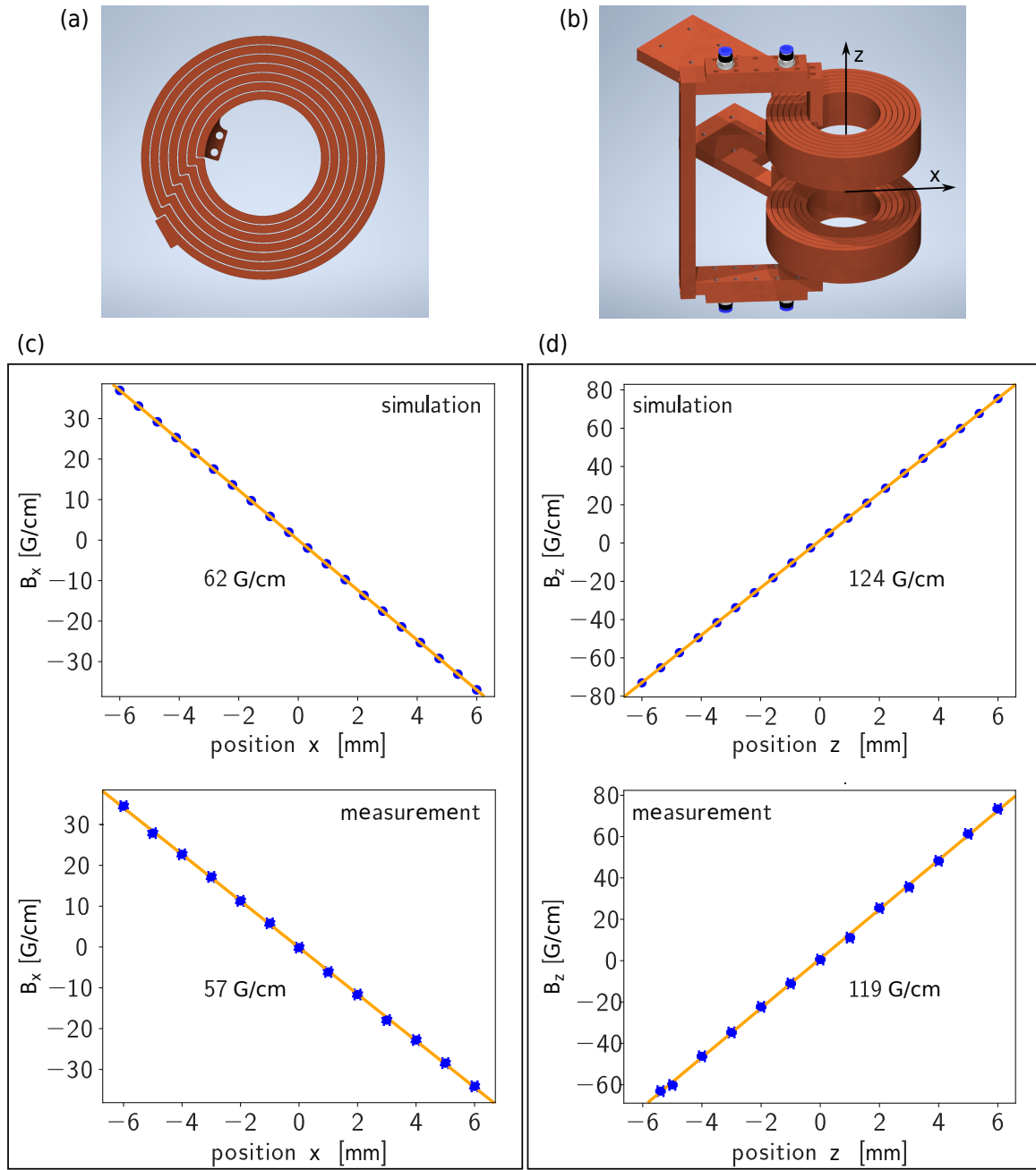


Figure 6.7: (a): Close up drawing of the MOT coil geometry. (b): Coordinate system indicating the x and z axes, along which the magnetic field simulation and measurement is shown. (c): Simulation and measurement of the magnetic field in the horizontal axis x . A measurement along the y axis, the horizontal axis perpendicular to x , shows minimal deviation, which arise from the bars connecting both coils to the power supply. This measurement is not shown here. (d): Simulation and measurement of the magnetic field in the vertical axis z . Simulation and measurement have been performed with a current of 800 A. Generally, simulation and measurement show good agreement, as the deviation is on the percent level of the gradient itself.

ahead towards the operation of a possible Zn clock, the atoms need to be transferred into a MOT operating on the narrow 308 nm transition. Using the approximation above, the capture velocity of the narrow MOT is estimated to be around 1 m s^{-1} , which may be still enhanced by frequency modulating the MOT beams of the narrow MOT [17]. Its limit is given by the atomic recoil at around $3 \text{ } \mu\text{K}$, at which the atoms would be transferred into an optical lattice.

6.3 Calculation of the magic wavelength

The theory behind dipole traps and optical lattices can be found in various publications and theses, *e.g.*, in Ref. [168]. However, trapping atoms in a lattice shifts the clock transition frequency due to the AC Stark effect. Fortunately, there are certain 'magic' wavelengths, at which the AC polarizabilities of the ground- and excited state are equal, eliminating the light shift. For the $^1\text{S}_0 \rightarrow ^3\text{P}_0$ clock transition in Zn, the magic wavelength for bosonic isotopes has been calculated to be 410 nm, following Ref. [116] by summing up the contributions to the AC polarizability from all relevant transitions. An overview over the transitions is provided in Tables 6.1 and 6.2 and a plot of the AC polarizabilities of ground and excited state is shown in Fig. 6.8. By calculating the magic wavelength of Sr with the same code and comparing the result, an error of $\pm 5 \text{ nm}$ is estimated. Hence, this calculation is close to the results of Refs. [169, 170], stating the magic wavelength to be 413 nm and 416 nm, respectively. Assuming a future clock setup, in which the lattice is created by an optical lattice with a finesse of $F = 300$, 100 mW light power coupled into the cavity and a mode waist of $w_0 = 50 \text{ } \mu\text{m}$, the lattice depth is calculated to be 22.7 recoil energies while the scattering rate is around 0.4 Hz for the $^1\text{S}_0$ and $^3\text{P}_0$ state. Scattering lattice photons heats the atoms and limits the trap lifetime to several seconds. By fitting the trapping potential within one full-width-half-maximum with a harmonic oscillator model, the trap frequency is approximated to be 150 kHz, which is well above the recoil frequency and the clock transition linewidth. Following Ref. [116], it can be concluded that this trap confines Zn in the Lamb-Dicke regime with resolved sidebands. As the trap potential is two orders of magnitude larger than the thermal energy at the Doppler temperature of the narrow MOT, $k_{\text{B}}T_{\text{D}, 308 \text{ nm}}$, atoms could be efficiently loaded.

Table 6.1: Transitions from the $^1\text{S}_0$ state involved for the calculation of the magic wavelength in Zn.

transition	λ [nm]	A [s^{-1}]	source
$4s4p\ ^1\text{P}_1$	213.9	7.1×10^8	[137]
$4s5p\ ^1\text{P}_1$	159.0	85.5×10^6	[171]
$4s6p\ ^1\text{P}_1$	145.8	12.5×10^6	[171]
$4s7p\ ^1\text{P}_1$	140.4	5.6×10^6	[171]
$4s8p\ ^1\text{P}_1$	137.7	2.8×10^6	[171]
$4s4p\ ^3\text{P}_1$	307.6	3.8×10^4	[137]

Table 6.2: Transitions from the 3P_0 state involved for the calculation of the magic wavelength in Zn. Experimental values from Ref. [172] are preferred over theoretical values from Refs. [173, 174].

transition	λ [nm]	A [s^{-1}]	source
$4s5s\ ^3S_1$	468.0	13.5×10^6	[173]
$4s6s\ ^3S_1$	307.2	4.0×10^6	[172]
$4s7s\ ^3S_1$	267.1	1.9×10^6	[172]
$4s8s\ ^3S_1$	253.0	1.5×10^6	[173]
$4s4d\ ^3D_1$	328.2	90.0×10^6	[172]
$4s5d\ ^3D_1$	275.7	34.0×10^6	[172]
$4s6d\ ^3D_1$	257.0	18.7×10^6	[173]
$4s7d\ ^3D_1$	248.0	8.5×10^6	[173]
$4p^2\ ^3D_1$	208.0	2.8×10^8	[174]

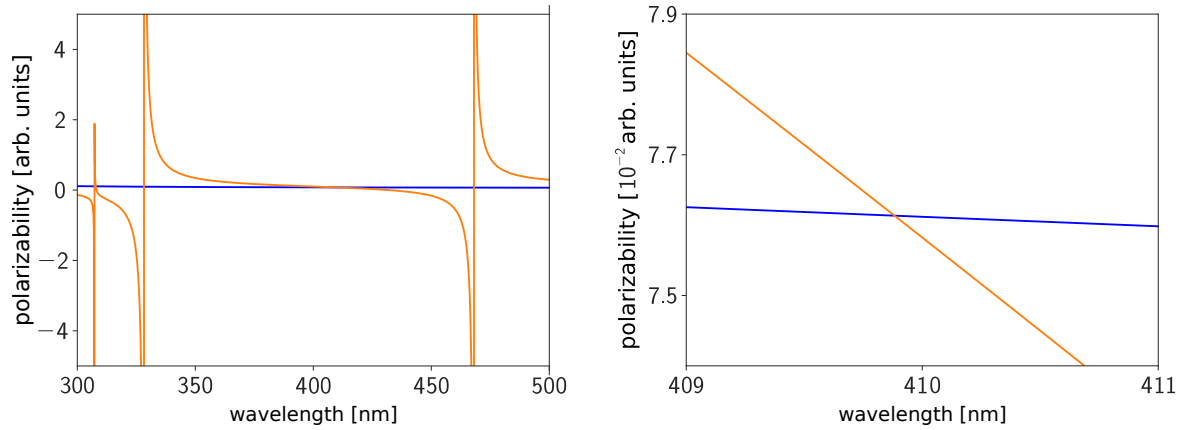


Figure 6.8: This figure shows the AC polarizabilities for the ground state in blue and the excited state in orange. The magic wavelength is around 410 nm, as the the polarizabilities for ground and excited states are equal.

Conclusion

As shown in Chapter 2, Zn is as an interesting candidate for a future optical clock based on neutral atoms trapped in a lattice. Zn offers a favorable natural isotopic abundance, with one fermionic and four bosonic isotope. The level scheme exhibits a typical structure for earth-alkaline and earth-alkaline-like atoms, where the involved transitions lie in the deep-UV (Section 2.2.1). A broad transition at 214 nm with a linewidth of 111 MHz enables efficient momentum transfer on the atoms, allowing efficient laser cooling in Zeeman slower and MOTs. A narrow transition with 4.7 kHz linewidth at 308 nm can be utilized for further cooling with commercially available lasers (Section 2.4.2). The clock transition at 310 nm exhibits a line-Q similar to Sr (Section 2.3.1), but its sensitivity to black-body radiation is one order-of-magnitude lower (Section 2.3.2). The transition can be interrogated by a frequency-quintupled telecom-wavelength laser, whose fundamental can be distributed through existing fiber networks without the need of a frequency comb (Section 2.3.3).

This laser system has been established by three conversion stages, including one doubling stage and two sum-frequency generation stages, eventually resulting in 0.5 mW power. To prepare the way to laser cooling of Zn, a laser at 214 nm has been constructed by frequency quadrupling a titanium-sapphire laser in two subsequent frequency-doubling cavities yielding around 10 mW power (Section 2.4.1). To achieve the first laser cooling of Zn and operate a MOT with sufficient capture velocities and large atom numbers, the power still has to be significantly increased.

One main achievement of this work is the spectroscopic characterization of the 214 nm transition in collaboration with the *Cold Molecule Group* at the *Fritz-Haber-Institut* (Chapter 4 and Appendix A). Using a cryogenic buffer gas cooled atomic beam of Zn and a two-detector fluorescence collection, the isotope shifts for all stable isotopes of Zn are measured and the hyperfine A and B coefficient are determined. By referencing the laser frequency to a ULE cavity, the precision in the isotope shift measurements surpass previously reported values by more than one order-of-magnitude and lies in the percent-level of the linewidth. To the best of our knowledge, this measurement provides the first laser spectroscopy on this transition.

Furthermore, isotope shifts have been measured on the 423 nm transition in Ca using saturated absorption spectroscopy, while applying lock-in detection with amplitude modulation of the pump beam (Chapter 5 and Appendix B). Although saturated absorption spectroscopy is significantly more prone to systematic errors than fluorescence collection on atomic beams, their careful analysis has led to an improvement of existing values by a factor of 3 to the permille-scale of the linewidth. The insights from this study can be directly applied to other lines, *e.g.*, the narrow cooling transition in Zn.

As the narrow lines require significantly higher atom densities, strong Zn-Zn collisional effects come into play. Hence, a setup and a measurement plan for fluorescence collection on a Zn atomic beam has been designed (Section 6.1), exploiting a low atom density in the beam and the large detection efficiency of photomultipliers.

To achieve the required frequency stability in narrow lines, a ULE resonator has been designed and its optimal support points were simulated to achieve a minimal vibration sensitivity of its resonance frequency (Section 6.1.1). After construction and locking a laser to its resonance, the frequency drifted within minutes on scales much larger than the atomic linewidth. To improve the setup, a new vacuum system has been designed for faster evacuation. A new support structure promises enhanced rigidity and reduced thermal coupling to the surrounding, while an active temperature stabilization will improve the thermal stability. The new design will be constructed in the future featuring an active temperature stabilization and promising improved rigidity and thermal isolation.

To prepare the path towards a Zn lattice clock, a MOT setup has been constructed (see Section 6.2), with the vacuum maintained at 10^{-8} mbar (Section 6.2.1). The setup includes, a suitable atom source (Section 6.2.2) and an Anti-Helmholtz coil pair (Section 6.2.3) and provides a promising platform for demonstration of the first laser cooling of Zn. This setup will be made operational to demonstrate the first laser cooling of Zn, when sufficient laser power is available.

In conclusion, during this work high precision spectroscopy on atomic transitions has been performed. The insights lay a foundation for future spectroscopy on narrow lines, not only for the intercombination line in Zn, but also in Ca. Furthermore, it established the groundwork for the construction of deep UV lasers with powers larger than 100 mW, sufficient for laser cooling of Zn. Fundamentals in the design, the simulation and the construction of ULE cavities have been explored, additionally which may be further continued in this research group. Ultimately, it shows an experiment, in which laser cooling could be achieved. Once attempts for laser cooling on the 214 nm transition has been successful, effort may be put into transferring the atom into a narrow MOT operating on the intercombination line. To obtain an operating optical clock, a more elaborated experimental setup would be needed, suitable for an optical lattice at the magic wavelength and interrogation of the clock transition along the same axis.

Publication: Hyperfine structure and isotope shifts of the $(4s^2) ^1S_0 \rightarrow (4s4p) ^1P_1$ transition in atomic zinc

This section shows a reprint of the journal article [34]. Its complete citation reads

David Röser, J. Eduardo Padilla-Castillo, Ben Ohayon, Russell Thomas, Stefan Truppe, Gerard Meijer, Simon Stellmer, and Sid C. Wright,

Hyperfine structure and isotope shifts of the $(4s^2) ^1S_0 \rightarrow (4s4p) ^1P_1$ transition in atomic zinc,
Phys. Rev. A **109** (2024) 012806.

DOI: <https://doi.org/10.1103/PhysRevA.109.012806>

The article is included in this dissertation with the consent of all co-authors and the permission of the American Physical Society under the terms of the Creative Commons Attribution 4.0 International license.

Contents of Publication

A.1	I. Introduction	62
A.2	II. Experimental Setup	62
A.3	III. Analysis of Spectral Line Shapes	64
A.4	IV. Results	65
A.5	V. Discussion	67
A.6	VI. Summary and Outlook	68

Hyperfine structure and isotope shifts of the $(4s^2)^1S_0 \rightarrow (4s4p)^1P_1$ transition in atomic zincDavid Röser,^{1,*} J. Eduardo Padilla-Castillo^{2,*} Ben Ohayon³ Russell Thomas² Stefan Truppe^{2,4}
Gerard Meijer² Simon Stellmer¹ and Sid C. Wright^{2,†}¹University of Bonn, Nussallee 12, 53115 Bonn, Germany²Fritz-Haber-Institut der Max-Planck-Gesellschaft, Faradayweg 4-6, 14195 Berlin, Germany³The Helen Diller Quantum Center, Department of Physics, Technion-Israel Institute of Technology, Haifa 3200003, Israel⁴Centre for Cold Matter, Blackett Laboratory, Imperial College London, London SW7 2AZ, United Kingdom (Received 30 August 2023; revised 8 November 2023; accepted 29 November 2023; published 10 January 2024)

We report absolute frequency, isotope shift, radiative lifetime, and hyperfine structure measurements of the $(4s^2)^1S_0 \rightarrow (4s4p)^1P_1$ (213.8 nm) transition in Zn I using a cryogenic buffer gas beam. Laser-induced fluorescence is collected with two orthogonally oriented detectors to take advantage of differences in the emission pattern of the isotopes. This enables a clear distinction between isotopes whose resonances are otherwise unresolved, and a measurement of the ^{67}Zn hyperfine structure parameters, $A(^{67}\text{Zn}) = 20(2)$ MHz and $B(^{67}\text{Zn}) = 10(5)$ MHz. We reference our frequency measurements to an ultralow expansion cavity and achieve an uncertainty at the level of 1 MHz, about 1 percent of the natural linewidth of the transition.

DOI: [10.1103/PhysRevA.109.012806](https://doi.org/10.1103/PhysRevA.109.012806)**I. INTRODUCTION**

The alkaline-earth-metal (AEM) elements are identified by two valence electrons and a $J = 0$ electronic ground state. These two features give rise to a number of unique properties. First, the level structure decomposes into singlet and triplet states, with broad transitions within each system and narrow intercombination lines between them. Just as in the helium atom, the lowest triplet states are metastable. Second, states with zero electronic angular momentum are free of hyperfine structure. In addition, even-mass isotopes have even proton and even neutron numbers, leading to zero nuclear spin and absence of hyperfine structure in all electronic states. These properties enable a wealth of applications, including optical clocks [1], precision metrology [2], quantum computing [3–5], and Rydberg physics [6,7]. In recent years, AEM elements have played a major role in the search for yet undiscovered scalar gauge bosons through high-precision isotope shift spectroscopy [8], and various studies with neutral AEM atoms have been presented on this topic [9–14].

Alongside the AEM elements, and sharing these attractive properties, are the so-called group-IIB elements zinc, cadmium, and mercury. The broad singlet $^1S_0 \rightarrow ^1P_1$ transitions for these elements lie deep in the ultraviolet range of the spectrum, with natural linewidths in excess of 100 MHz. They possess a multitude of even- and odd-mass isotopes, with the latter showing hyperfine structure. The resonance lines

of the different isotopes are convoluted and often cannot be resolved in conventional Doppler-free spectroscopy. While Cd and Hg have already been employed for the development of optical clocks [15–17], there is very modest work towards this application with zinc thus far [18], mainly limited by the available laser technology. The wider chain of radioactive zinc isotopes is of interest for nuclear structure studies. For this reason, their isotope shifts have been measured in the triplet manifold [19,20], with new experiments ongoing [21,22].

Here, we present high-resolution spectroscopy of the $(4s^2)^1S_0 \rightarrow (4s4p)^1P_1$ transition near 213.8 nm in neutral zinc. Experiments were conducted over a two-week campaign in which an ultralow expansion cavity and required deep ultraviolet optics (University of Bonn) were transported to an atomic beam machine at the Fritz Haber Institute in Berlin. Our measurements are based on laser-induced fluorescence of a cryogenic beam of atoms extracted from a helium buffer gas cell. We employ a two-detector method to enable a clear distinction between even-mass isotopes with nuclear spin zero from the spin-5/2 ^{67}Zn isotope. As a result, we are able to use zinc samples of natural isotopic abundance in the experiments. Isotope shifts and hyperfine interaction constants are determined with an uncertainty of the order of 1 MHz. This method provides a blueprint for measurements of hyperfine structure in strong optical transitions, and a convenient and direct way to measure the true collection solid angle of a fluorescence detector. Our approach can be readily adapted to other species with several naturally occurring isotopes, e.g., Sn, Ni, and applied in the study of radioactive nuclei.

II. EXPERIMENTAL SETUP

Figure 1(a) illustrates our experimental apparatus and laser system. We use a cryogenic buffer gas source to produce a cold, slow atomic beam of zinc. The atoms are produced by laser ablation of a solid Zn target (natural abundance)

*These authors contributed equally to this work.

†sidwright@fhi-berlin.mpg.de

Published by the American Physical Society under the terms of the [Creative Commons Attribution 4.0 International license](https://creativecommons.org/licenses/by/4.0/). Further distribution of this work must maintain attribution to the author(s) and the published article's title, journal citation, and DOI. Open access publication funded by the Max Planck Society.

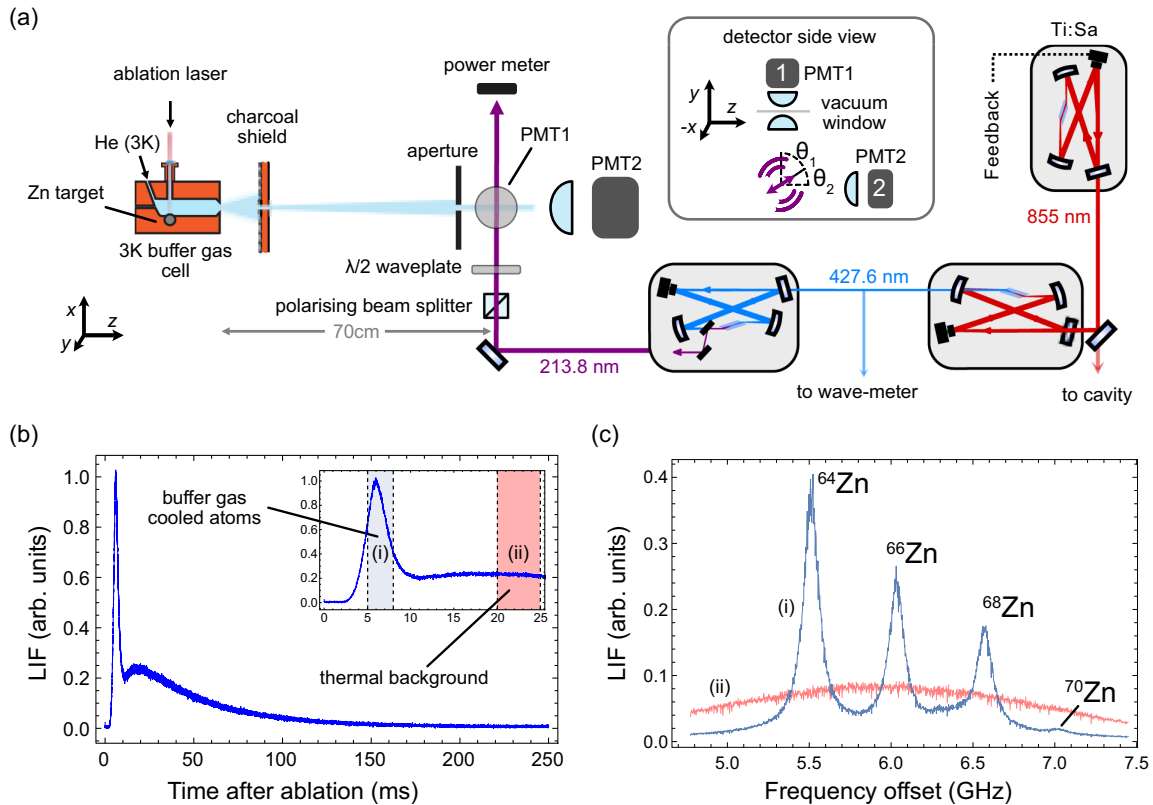


FIG. 1. (a) Experimental setup for $^1S_0 \rightarrow ^1P_1$ laser-induced fluorescence spectroscopy of Zn, showing the cryogenic buffer gas beam, and 213.8 nm laser system. We also show a side view of the detector geometry, showing the two photomultipliers used, and the angles θ_1 and θ_2 relative to the linear polarization angle of the excitation light. These angles determine the emission pattern observed at the two detectors. (b) A typical time-of-flight fluorescence trace observed at the ^{64}Zn resonance. The inset shows a zoom-in of the region $0 < t < 25$ ms. Observation windows for the buffer gas cooled and thermal background components of the signal are shown by the shaded bars. (c) Fluorescence spectra for the observation windows in (b).

and are cooled in the cell by collisions with a He gas at a temperature of 3 K, and exit the cell with a typical velocity of 140 m/s along the z axis. The ablation laser is fired at a rate of 1 Hz which sets the repetition rate for the experiments. At a distance 70 cm downstream of the cell exit, we excite the $^1S_0 \rightarrow ^1P_1$ transition with a single probe laser beam near 213.8 nm, which intersects the atomic beam perpendicularly. A 2×2 mm square aperture restricts the range of transverse velocities in the atomic beam to below 2 m/s. Around 10^7 atoms per pulse pass through the detector.

Continuous wave laser light is produced by twice frequency doubling the infrared light of a Ti:sapphire laser near 855.2 nm. Each frequency doubling stage consists of an enhancement resonator containing a nonlinear crystal; to reach 213.8 nm from 427.6 nm, we use beta barium borate (β -BBO). The 855.2 nm light from the Ti:sapphire laser is frequency stabilized either by referencing to a commercial wave-meter (High Finesse WS8-10 calibrated with a temperature-stabilized HeNe laser) or via an ultralow expansion (ULE) optical cavity (Menlo ORC) with a measured free spectral range of 2.992 184(30) GHz. We also record the intermediate 427.6 nm light on the wave-meter since this light is immune from parasitic multimode content at the fundamental

wavelength. The wave-meter option offers an absolute accuracy of about 30 MHz when measuring the 427.6 nm light, a resolution of about 1 MHz, and enables continuous scanning over the entire spectrum. Scanning via the reference cavity reduces the linewidth of the laser and improves the linearity of the frequency axis. To do this, light at the fundamental wavelength of the Ti:sapphire laser is coupled into a fiber phase modulator (EOM, Jenoptik) driven with two rf frequencies, $\nu_{\text{PDH}} = 18$ MHz and $\nu_{\text{scan}} \sim 1$ GHz. The phase-modulated light reflected from the cavity is collected on a fast photodiode, demodulated at the frequency ν_{PDH} which produces a Pound-Drever-Hall (PDH) signal with sharp zero crossing points when the laser frequency is at a cavity resonance ν_c , or at $\nu_c \pm \nu_{\text{scan}}$. We lock the laser to the latter and scan the laser frequency by varying ν_{scan} . A camera is used to monitor the light transmitted through the cavity and ensure locking to the TEM_{00} mode. This locking scheme enables continuous scanning of the Ti:sapphire laser frequency up to one-half of the cavity free spectral range, corresponding to 6 GHz at the 213.8 nm detection wavelength.

At the atomic beam machine, we purify the laser polarization with a polarizing beam cube and control its linear polarization angle relative to the direction of the atomic

beam with a $\lambda/2$ plate. The probe light propagates along the x axis and has a peak intensity $I = 10^{-3}I_{\text{sat}}$, where $I_{\text{sat}} = \pi\hbar c\Gamma/(3\lambda^3) = 1.5 \text{ W/cm}^2$ is the two-level saturation intensity of the transition. Orthogonality between the laser and atomic beam direction is ensured using a set of alignment irises mounted on the detection chamber, and by aligning light through the atomic beam aperture and a small hole in the back of the buffer gas cell. We estimate that an atom traveling through the maximum intensity of the excitation light scatters five photons at resonance. The resulting laser-induced fluorescence (LIF) is collected and imaged onto two photomultiplier tubes (PMTs), whose photocurrents are delivered to separate transimpedance amplifiers and recorded as time-of-flight traces. The two PMTs are oriented to collect fluorescence emitted parallel and perpendicular to the direction of the atomic beam, as shown in Fig. 1(a). The angle θ_i between the laser polarization and the direction of detector i , illustrated in the inset to the figure, determines the portion of the fluorescence emission pattern collected by the two detectors. This enables discriminating between even- and odd-mass isotopes [13,23,24]. We record the laser power after the machine with a calibrated optical power meter and compensate for drifts in the probe intensity over a scan (typically 5–10%).

Figure 1(b) shows a typical time-of-flight trace observed in detector 1 when exciting the ^{64}Zn resonance. The signal comprises an initial intense peak from the buffer gas cooled atomic beam at roughly 5 ms, followed by an extended tail which appears for several tens of ms later. The extended tail consists of thermalized Zn atoms which leave the cell and collide with the vacuum walls without sticking; it persists even when the direct line of sight from the source to the detector is blocked, and leads to a broad background signal in the fluorescence spectra, whose Doppler width is consistent with the laboratory temperature. Example spectra showing the two signal components are shown in Fig. 1(c). Compared to a continuous atomic vapor source, signal from the thermalized atoms is significantly reduced simply by choosing an appropriate time-of-flight observation window.

III. ANALYSIS OF SPECTRAL LINE SHAPES

The five naturally occurring isotopes of zinc ($Z = 30$) can be separated into four even-mass isotopes and a single odd-mass isotope with mass number 67. In the following, we discuss the line-shape models used for these two cases in order to fit the experimental spectra. Here we use ν_L to label the laser frequency and assume that the laser linewidth is much less than the natural linewidth of the transition.

Line shape for even-mass isotopes. The even-mass zinc isotopes, all with nuclear spin $I_N = 0$, exhibit no hyperfine structure and the total angular momenta of the ground and excited states are $F = 0$ and $F' = 1$, respectively. The resonance line of an even-mass isotope e can be simply described with the line function,

$$S^{(e)} = \frac{\Gamma^2/4}{\Gamma^2/4 + \Delta_e^2} [1 - P_2(\cos\theta)g(\theta_C)]. \quad (1)$$

Here, $\Gamma/(2\pi)$ is the Lorentzian linewidth of the transition, $\Delta_e/(2\pi) = \nu_L - \nu_e$ is the detuning of the laser from the resonance frequency ν_e , and $P_2(\cos\theta) = \frac{1}{2}(3\cos^2\theta - 1)$ is the

64

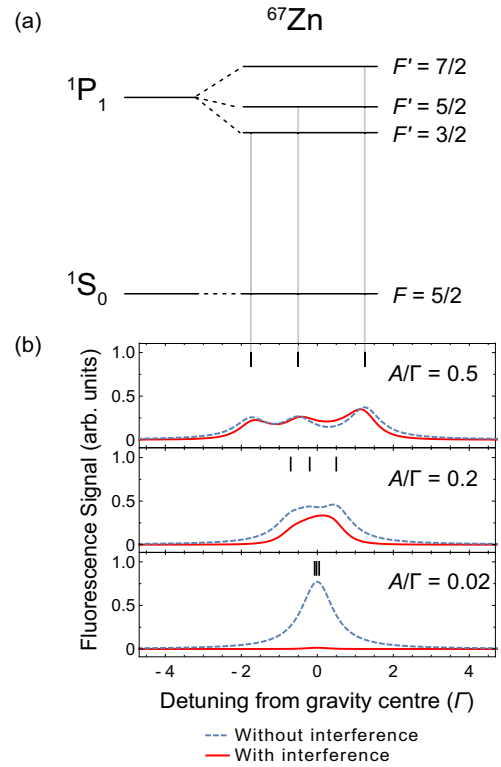


FIG. 2. Simulated fluorescence spectra for ^{67}Zn . (a) Level scheme labeling the total angular momenta F, F' for the ground and excited states, respectively. (b) Simulated spectra for detection along $\theta = 0$, for different values of the ratio A/Γ and with $B = 0$. We show the results with and without quantum interference included in the calculation. The sticks above the spectra correspond to the energies of the levels in (a). As A/Γ approaches zero (negligible hyperfine interaction), the emission pattern including interference converges to that of an ideal Hertzian dipole, meaning the emission is zero along $\theta = 0$.

second Legendre polynomial, with θ the angle between the detection direction and the electric field of the linearly polarized excitation light. The factor $g(\theta_C) = \cos(\theta_C)\cos^2(\theta_C/2)$ corrects for the effect of the finite solid angle of the detection optics, with θ_C the half angle of a circular collection lens. For $\theta = 0$, $S^{(e)} \rightarrow 0$ as $\theta_C \rightarrow 0$, as would be expected from the well-known Hertzian dipole radiation pattern. Importantly, adjusting θ or θ_C changes the amplitude of $S^{(e)}$ observed at the detector.

Line shape for odd-mass isotopes. There exists a single naturally abundant odd-mass isotope of Zn with nucleon number 67 and a nuclear spin $I_N = 5/2$. The nuclear spin couples with the electronic angular momentum J to give total angular momentum F , resulting in a single $^1S_0, F = 5/2$ hyperfine level and three $^1P_1, F'$ excited levels with $F' = 3/2, 5/2, 7/2$. These energy levels are shown in Fig. 2(a). We assume the hyperfine energies $E(F)$ are given by

$$E(F) = \frac{A}{2}C + B\frac{3}{4}\frac{C(C+1) - I_N(I_N+1)J(J+1)}{2I_N(2I_N-1)J(2J-1)}, \quad (2)$$

with $C = F(F + 1) - I_N(I_N + 1) - J(J + 1)$. Here, $A = A(^1P_1)$ describes the strength of the magnetic dipole interaction between the electron and the nucleus. The coefficient $B = B(^1P_1)$ describes the interaction strength between the nuclear electric quadrupole moment and the electric field gradient at the nucleus.

Following Brown *et al.* [25], the fluorescence spectrum of ^{67}Zn , $S^{(o)}$ can be separated into three terms:

$$\begin{aligned}
 S^{(o)} &= \frac{\Gamma^2}{4} \{A + [B + C]P_2(\cos\theta)g(\theta_C)\}, \\
 A &= \frac{1}{9} \left(\frac{2}{\Gamma^2/4 + \Delta_{3/2}^2} + \frac{3}{\Gamma^2/4 + \Delta_{5/2}^2} + \frac{4}{\Gamma^2/4 + \Delta_{7/2}^2} \right), \\
 B &= -\frac{1}{225} \frac{1}{\Gamma^2/4 + \Delta_{3/2}^2} \\
 &\quad - \frac{64}{525} \frac{1}{\Gamma^2/4 + \Delta_{5/2}^2} - \frac{2}{21} \frac{1}{\Gamma^2/4 + \Delta_{7/2}^2}, \\
 C &= \left[-\frac{8}{45} \frac{1}{(\Gamma/2 + i\Delta_{7/2})(\Gamma/2 - i\Delta_{3/2})} \right. \\
 &\quad - \frac{6}{35} \frac{1}{(\Gamma/2 + i\Delta_{7/2})(\Gamma/2 - i\Delta_{5/2})} \\
 &\quad \left. - \frac{1}{25} \frac{1}{(\Gamma/2 + i\Delta_{5/2})(\Gamma/2 - i\Delta_{3/2})} \right] + \text{c.c.} \quad (3)
 \end{aligned}$$

Here, $\Delta_{F'}/(2\pi) = \nu_L - \nu_{F'}$ is the detuning of the laser from the excited state with total angular momentum F' ; we assumed all Zeeman sublevels in the 1S_0 state are equally populated in the source and neglected optical pumping during the interaction with the probe light.

Important for the experiments is the fact that when the hyperfine structure is barely resolved, the emission pattern and hyperfine structure become strongly coupled. This is illustrated by Fig. 2(b), which shows simulated fluorescence spectra along $\theta = 0$ for different ratios of A/Γ . Each panel compares Eq. (3) with the result when interference is removed from the model, i.e., C is deliberately set to zero. The calculations show that as $A/\Gamma \rightarrow 0$, interference between scattering paths is destructive, leading to complete suppression of the fluorescence along this direction. There is an intuitive explanation for this effect: when the hyperfine interaction with the nucleus becomes negligible, the emission pattern must converge to that of the (spinless) even-mass isotopes. Conversely, one can produce the reverse effect in the even-mass isotopes by deliberately applying a magnetic field along $\theta = 90^\circ$. This is the so-called Hanle effect [26,27] and, while understood for about a century, is often overlooked. The behavior illustrated in Fig. 2(b) shows that interference in the emission pattern of barely resolved lines contains useful information which can be used to constrain the hyperfine structure. The central spectrum in the figure, where $A/\Gamma = 0.2$, is near the value observed in the experiments. This results in a total span of the 1P_1 levels of 1.2Γ , and reduces the peak scattering rate by about 40% with respect to that of the even-mass isotopes. Optical pumping between Zeeman sublevels of the ground state by the excitation light results in a time-dependent emission pattern, and a slight change to the fluorescence line shape. We simu-

lated population changes using rate equations and include this effect in our uncertainty analysis.

Combined line function. The total fit function used in this study is given by

$$S^{(\text{tot})} = a_{67}S^{(o)} + \sum_e a_e S^{(e)} + a_{bg} e^{-(\nu_L - \nu_{bg})^2 / (2w_{bg}^2)}. \quad (4)$$

Here, a_{67} and a_e represent the relative abundances of the odd- and even-mass isotopes, respectively. The final term in Eq. (4) approximates the residual thermal background in the spectrum, whose amplitude a_{bg} is typically 5 to 10 percent of the ^{64}Zn resonance peak. The center frequency ν_{bg} and width parameter w_{bg} can be either fitted as free parameters or introduced as fixed parameters by first fitting the data at late arrival times when only the thermal background component is present. The fitted values for the isotope shifts in these two cases are consistent within the statistical error of the fits.

IV. RESULTS

A. Determination of the ^{67}Zn hyperfine structure by a two-detector method

Figures 3(a) and 3(b) show two sets of spectra obtained using the High Finesse wave-meter as a frequency reference. The data constitute two separate scans where the input polarization of the laser is along the y axis [Fig. 3(a)] and along the z axis [Fig. 3(b)], and for each panel, we show the fluorescence spectrum recorded by the two detectors 1 and 2. For clarity, each is labeled with a schematic showing the laser polarization, the detector orientation, and the dominant emission pattern for the even-mass isotopes. The different emission pattern of the ^{67}Zn isotope (relative natural abundance 4.1%) dramatically increases its visibility in detector i when $\theta_i = 0$. We show the fitted ^{67}Zn line shape with a black dashed line in each panel to illustrate this effect.

We use these spectra to determine solid angles of the collection optics and hyperfine structure of the ^{67}Zn isotope. The four spectra in Fig. 3 were fitted as a single dataset, fixing the detection angles θ_i to their values in the experiment, and enforcing the natural abundance of Zn isotopes [28]. This fixes the relative peak heights in each spectrum so that the detector solid angles $\theta_{C,1}$, $\theta_{C,2}$, and the hyperfine structure constants A and B of the ^{67}Zn isotope, can be determined. All resonance frequencies ν_e for all even-mass isotopes e , $\nu_{1/2,3/2,5/2}$ for the ^{67}Zn isotope, and a common Lorentzian linewidth Γ are shared fit parameters between the datasets. From this data, we conclude $\theta_{C,1} = 0.281 \pm 0.005$, $\theta_{C,2} = 0.145 \pm 0.005$ radians. The uncertainties are the range of values obtained when fitting the data with various reasonable assumptions, such as fixing the values of w_{bg} and ν_{bg} in the fit function using the signal at late arrival times. The value of $\theta_{C,2}$ is very close to the half angle subtended by the collection lens at the fluorescence region, 0.156(5) radians. The value of $\theta_{C,1}$ is significantly below the half angle subtended by its in-vacuum collection lens, 0.43(1) radians, and consistent with this lens being placed about 5 mm too close to the atomic beam, a result of incorrectly extrapolating the focal length from the visible to the deep ultraviolet.

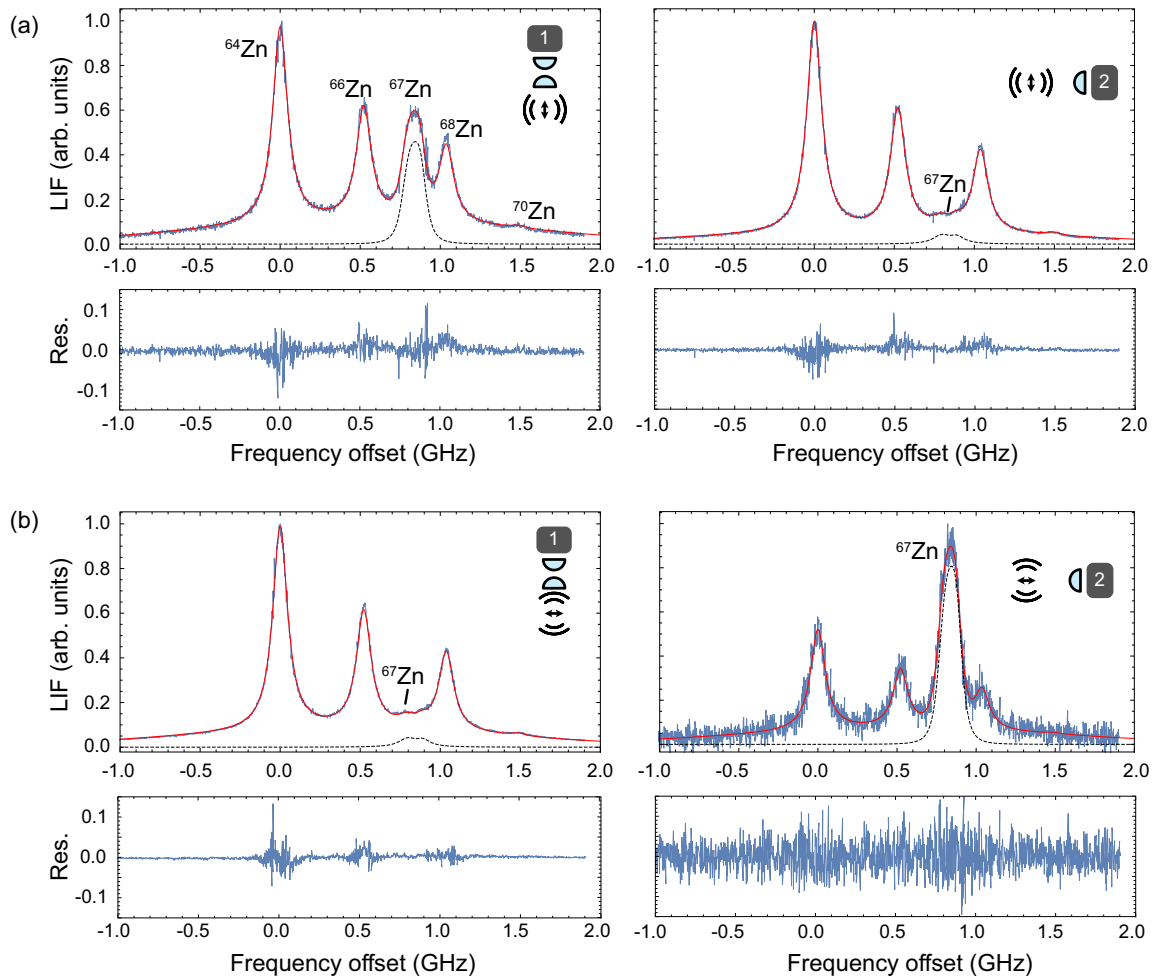


FIG. 3. Polarization sensitive fluorescence detection of Zn isotopes. Each spectrum is labeled by the probe laser polarization and detector configuration. The relative line intensities of the even- and odd-mass isotopes are strong functions of the angle θ between the laser polarization and the detector direction, and the solid angle of the collection optics. Blue lines show experimental data, red solid lines are fits as described in the text, and black dashed lines show the fitted ^{67}Zn line shape. Underneath each spectrum, the residuals are shown in a separate plot (Res.). (a) Laser polarization along the y axis. (b) Laser polarization along the z axis.

For the hyperfine interaction parameters, we obtain $A(^{67}\text{Zn}) = 20 \pm 2$ MHz and $B(^{67}\text{Zn}) = 10 \pm 5$ MHz. Fitting the data with $B = 0$ returns $A = 21$ MHz but noticeably reduces the goodness of the fit near the ^{67}Zn peak. Fitting to a model which ignores interference may be done by simply setting $C = 0$ in Eq. (3); this gave the best-fit values $A = 9.5$ MHz, $B = 0.6$ MHz, $\theta_{C,1} = 0.37$, and $\theta_{C,2} = 0.20$, and line centers consistent with the full interference model. In this case, the fitted value of $\theta_{C,2}$ is larger than the geometric solid angle presented by the collection lens, and the fit residuals clearly indicate that only the interference model can adequately describe the signal observed in both detectors.

B. High-resolution measurements with the cavity

Having constrained the ^{67}Zn hyperfine structure and solid angle of the collection optics, we proceeded to scan the laser via the ULE reference cavity to more accurately determine

the isotope shifts. Figure 4 shows spectra obtained when scanning ν_{scan} with the laser locked to the ULE cavity, and with the probe laser horizontally polarized. The scan rate corresponds to approximately 0.8 MHz/s for the 213.8 nm probe light, where the frequency ν_{scan} was measured near the time of the ablation laser pulse, and then stepped discretely after each measurement. By happenstance, the ^{66}Zn resonance appeared almost exactly at the midpoint between two cavity resonances, where the locking method fails. We therefore frequency shifted the Ti:sapphire laser light by 90 MHz before delivery to the cavity with an acoustic optic modulator, moving the unstable lock point by 360 MHz in the deep ultraviolet. The upper (lower) dataset in the figure is taken with (without) the frequency shifting method applied, on the same day but ablating different spots on the Zn target, which enabled measuring all isotopes. We fit the two spectra as a single dataset with shared resonance line positions in a Monte Carlo routine, where the values of $\theta_{C,1}$, $\theta_{C,2}$, A , and

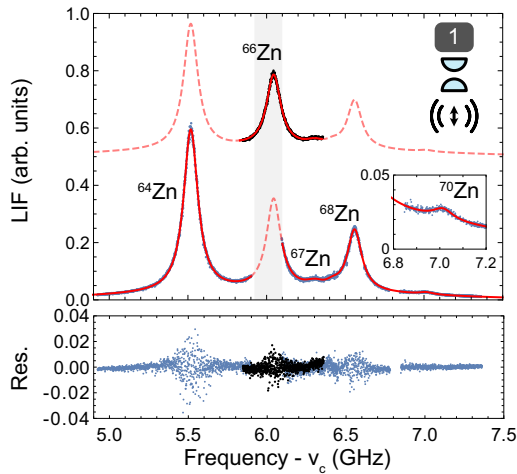


FIG. 4. Fluorescence spectra taken with the probe laser locked to the ULE cavity. The shaded box shows the region near the midpoint of the cavity resonances in which the lock fails. In the upper spectrum, shown with a deliberate offset on the y axis, the light delivered to the cavity was first frequency shifted by 90 MHz. This enables a continuous scan over the ^{66}Zn resonance. The two spectra are fitted as a single dataset to recover the isotope shifts as discussed in the text. Dashed lines show the fit functions where data are not present for each spectrum. The plot underneath shows the residual from the fit function for the two datasets.

B are drawn from uniform distributions whose ranges are given by the limits constrained in Sec. IV A. Enforcing the relative natural abundance of Zn in the fits leads to small changes in the best-fit values compared to allowing the line intensities to float, and we include this when estimating the uncertainties. We combine the best-fit values and errors for the isotope shifts to give a weighted mean and statistical error for these parameters, and assume a 1 MHz systematic frequency uncertainty which derives from the ~ 200 kHz uncertainty of ν_{scan} and the frequency shifting AOM, considering the two successive stages of frequency doubling. Doppler shifts due to slight misalignment of the probe laser light contribute an uncertainty ~ 2 MHz to the absolute resonance frequencies, and negligibly to the isotope shifts. Recoil from absorption of the probe laser light leads to a Doppler shift of roughly 0.6 MHz across the detection volume, and the differential shift across the range of isotopes is an order of magnitude smaller. We neglect this contribution to the isotope shift uncertainty. The ambient magnetic field in the detector was measured as below 0.3 Gauss, corresponding to an upper bound to the line-shape broadening of 0.5 MHz.

V. DISCUSSION

Table I summarizes the results of our measurements and compares them to the available literature values. Our final values for the isotope shifts are presented relative to the ^{64}Zn resonance since this isotope is of highest abundance and its line center has the smallest statistical uncertainty. We combine measurements from the cavity and spectra taken using the wave-meter, and include a systematic frequency error of

TABLE I. Summary of the results obtained for the $(4s^2)^1S_0 \rightarrow (4s4p)^1P_1$ transition in Zn. Hyperfine constants and the radiative lifetime refer to the excited state. Results are given in MHz unless otherwise stated. CG: center of gravity. The isotope-averaged line center, $\bar{\nu}(^1S_0 - ^1P_1)$, is computed as the average of the individual isotope line centers weighted by their isotopic abundance.

	This work	Literature
$\nu_{66} - \nu_{64}$	525.0(3.0)	480(60) [30] 540(60) [31]
$\nu_{67}^{(\text{CG})} - \nu_{64}$	835(5)	
$\nu_{68} - \nu_{64}$	1039.8(1.7)	989(60) [30] 960(85) [31]
$\nu_{70} - \nu_{64}$	1495(4)	
$A(^{67}\text{Zn})$	20(2)	17.7(5) [29]
$B(^{67}\text{Zn})$	10(5)	
ν_{64}/cm^{-1}	46745.394(2)	
$\bar{\nu}(^1S_0 - ^1P_1)/\text{cm}^{-1}$	46745.407(2)	46745.404(2) [32]
τ/ns	1.440(18)	1.40(3) [33]

2.1 MHz for the wave-meter values, which derives from directly comparing frequency intervals measured by the cavity scan method with the wave-meter. For the ^{67}Zn isotope shift, we increased the error bar by 1 MHz to account for the effect of optical pumping within the detection volume. Our values are two orders of magnitude more precise than previous measurements, also given in the table. Our value of $A(^{67}\text{Zn})$ is consistent with the value measured by Kowalski and Träger [29], by level crossing spectroscopy of enriched ^{67}Zn . However, this study was unable to experimentally constrain the value of $B(^{67}\text{Zn})$ and we therefore recommend the values from our measurements.

The absolute frequency of the ^{64}Zn resonance measured through our experiments is 1401 391.66(6) GHz [46 745.394(2) cm^{-1}] and given in Table I. The uncertainty in our value is dominated by the wave-meter accuracy as specified by the manufacturer. The average of the line centers weighted by isotopic abundance, $\bar{\nu}(^1S_0 - ^1P_1)$, is also given in the table. It is in excellent agreement with the (isotope-unresolved) hollow cathode lamp measurements presented in Ref. [32].

Our best-fit value of the Lorentzian linewidth is $\Gamma/(2\pi) = 110.5(1.4)$ MHz, where the error derives from the standard deviation of the Monte Carlo fitted values combined with the frequency uncertainty from the cavity scanning method. Fitting with a Voigt line shape did not change the value of Γ within the uncertainty of the fit, and returned a Gaussian contribution to the linewidth of 7(7) MHz full width at half maximum. The radiative lifetime $\tau = 1/\Gamma$ given in the table is consistent with the weighted average of five measurements collated by Doidge [33], and is a factor of two more precise than previous measurements.

King plot. We combine our isotope shift results with values reported for the $^1S_0 \rightarrow ^3P_1$ intercombination transition [34] on a King plot as follows. We calculate the reduced isotope shifts $\delta\bar{\nu}^{A,A'} = \delta\nu/\mu^{A,A'}$, with $\mu^{A,A'}$ the difference in the

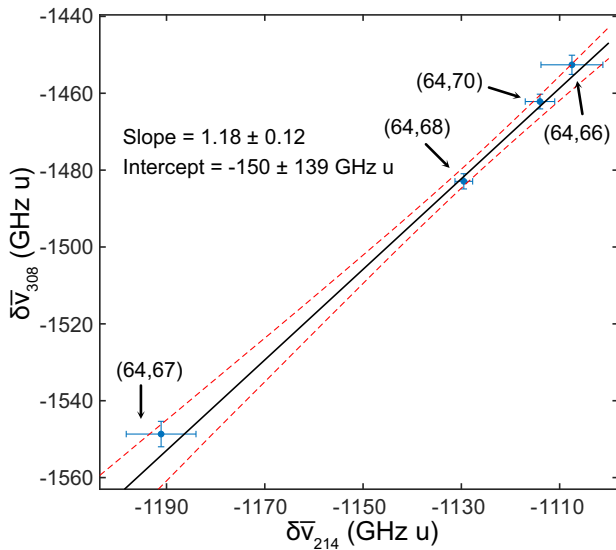


FIG. 5. A King plot of the $^1S_0 \rightarrow ^1P_1$ (213.8 nm, this work) and $^1S_0 \rightarrow ^3P_1$ (308 nm, Ref. [34]) transitions in Zn. The black solid line shows a linear fit to the data as discussed in the text. Red dashed lines indicate the 68% confidence interval of the fit.

inverse nuclear masses of the isotope pair (A, A'), and present the data in Fig. 5. The data are fitted to a linear relationship according to the recipe described in Ref. [35]. Briefly, we first define a mixing matrix to shuffle the 308 nm reduced isotope shifts so that they are referred to ^{64}Zn . We then calculate the covariance matrices, taking into account the mixing matrix and the reported errors. The most-probable values of the adjusted parameters, the intercept and slope, are found by minimizing a generalized χ^2 test statistic. To assign confidence intervals to the fitted parameters, we perform a Monte Carlo estimation procedure of repeated measurements drawn from a normal distribution centered at the most probable fitted values. The most probable value and 68% confidence interval of the fitted line is plotted in Fig. 5. That the value of the best-fitted slope, 1.18 ± 0.12 , is close to 1 reflects the fact that the $(4s^2)^1S_0$ ground state is common to both transitions. The remaining field shift likely stems from electron correlation effects, contributing to small but non-negligible field shifts for the $4s4p$ states.

An additional hyperfine interaction between the different electronic states in Zn would additionally shift the gravity center of the ^{67}Zn resonance lines, $\nu_{67}^{(\text{CG})}$, relative to the even-mass isotopes, and is often referred to as an “off-diagonal” hyperfine interaction. Such shifts should be detectable in a King plot as deviations of isotopes with nuclear spin from linear fits to the data of spin-zero isotopes (see, for example, Ref. [9]). To test for this, we repeat the fitting procedure without the (64,67) pair, and calculate its predicted values in each iteration of the Monte Carlo procedure to obtain its distribution. The resulting 68% confidence interval for the frequency difference $\nu_{67}^{(\text{CG})} - \nu_{64}$ is from 818 to 834 MHz, which agrees with our measured value [835(5) MHz] within its uncertainty. We infer that the difference in off-diagonal hyperfine shifts of the ^{67}Zn resonances, for this pair of transitions, is less than 10 MHz.

This closely follows results of isotope shift measurements for the lowest lying, and analogous, transitions in cadmium [13], another group-IIB element. It may be of interest considering recently observed strong hyperfine mixing effects for higher-lying transitions in zinc in the collinear resonance ionization spectroscopy (CRIS) experiment [22].

VI. SUMMARY AND OUTLOOK

We have reported isotope shifts, radiative lifetime, and hyperfine structure measurements for the $(4s^2)^1S_0 \rightarrow (4s4p)^1P_1$ transition in neutral Zn by cw laser-induced fluorescence spectroscopy of an atomic beam. Our measurements considerably improve upon the published literature for this transition and contribute to the study of the ^{67}Zn nucleus, where unexpected isotope shifts have recently been observed in collinear laser spectroscopy at the ISOLDE facility [22]. With its multitude of nuclear spin-zero isotopes and various narrow optical transitions, zinc is a candidate for further isotope shift spectroscopy at the sub-kHz level.

The two-detector method and analysis procedure described here takes greater advantage of the information available in atomic fluorescence measurements and has several benefits. First, it enables reliably extracting hyperfine parameters from barely resolved peaks. Second, two spectra are obtained simultaneously in which the visibility of isotopes can be tuned based on their fluorescence emission pattern. This approach allows disentangling otherwise overlapping lines and, in the case of atomic Zn studied here, enables a measurement of the isotope shifts and hyperfine structure at the ~ 1 MHz level. The approach can readily be adopted to other elements which feature broad transitions and many isotopes. It may be of benefit for accelerator-based collinear laser spectroscopy experiments, in particular those involving nuclear isomers which are difficult to separate by nuclear mass (see, for example, Ref. [36]). In addition, there are often multiple fluorescence decay channels from a given excited state, to final states with different values of the angular momentum J . Isolating fluorescence from specific decay path with a spectral filter necessarily selects a specific emission pattern for each isotope, a further tool in spectral analysis.

ACKNOWLEDGMENTS

We thank Sebastian Kray and the mechanical workshop of the Fritz Haber Institute for expert technical assistance. S.W. thanks Clara Bachorz for critical reading of the manuscript. We gratefully acknowledge financial support from the European Research Council (ERC) under the European Union’s Horizon 2020 Research and Innovation Programme [Co-MoFun, Grant Agreement No. 949119 (S.T.); “quMercury”, Grant Agreement No. 757386 (S.S.)], from the European Commission through Project No. 101080164 “UVQuanT” (S.T. and S.S.), and from Deutsche Forschungsgemeinschaft (DFG) through Grants No. 277625399, No. 414709674 and No. 496941189 and through the Cluster of Excellence ML4Q (Grant No. EXC 2004/1 - 390534769). B.O. is thankful for the support of the Council for Higher Education Program for Hiring Outstanding Faculty Members in Quantum Science and Technology.

- [1] A. D. Ludlow, M. M. Boyd, J. Ye, E. Peik, and P. O. Schmidt, *Rev. Mod. Phys.* **87**, 637 (2015).
- [2] M. G. Tarallo, T. Mazzoni, N. Poli, D. V. Sutyryn, X. Zhang, and G. M. Tino, *Phys. Rev. Lett.* **113**, 023005 (2014).
- [3] A. J. Daley, M. M. Boyd, J. Ye, and P. Zoller, *Phys. Rev. Lett.* **101**, 170504 (2008).
- [4] A. V. Gorshkov, A. M. Rey, A. J. Daley, M. M. Boyd, J. Ye, P. Zoller, and M. D. Lukin, *Phys. Rev. Lett.* **102**, 110503 (2009).
- [5] M. Saffman, *J. Phys. B: At. Mol. Opt. Phys.* **49**, 202001 (2016).
- [6] C. E. Simien, Y. C. Chen, P. Gupta, S. Laha, Y. N. Martinez, P. G. Mickelson, S. B. Nagel, and T. C. Killian, *Phys. Rev. Lett.* **92**, 143001 (2004).
- [7] A. Browaeys and T. Layahe, *Nat. Phys.* **16**, 132 (2020).
- [8] J. C. Berengut, D. Budker, C. Delaunay, V. V. Flambaum, C. Frugiuele, E. Fuchs, C. Grojean, R. Harnik, R. Ozeri, G. Perez, and Y. Soreq, *Phys. Rev. Lett.* **120**, 091801 (2018).
- [9] H. Miyake, N. C. Pisenti, P. K. Elgee, A. Sitaram, and G. K. Campbell, *Phys. Rev. Res.* **1**, 033113 (2019).
- [10] M. Witkowski, G. Kowzan, R. Munoz-Rodriguez, R. Ciuryło, P. S. Żuchowski, P. Masłowski, and M. Zawada, *Opt. Express* **27**, 11069 (2019).
- [11] N. L. Figueroa, J. C. Berengut, V. A. Dzuba, V. V. Flambaum, D. Budker, and D. Antypas, *Phys. Rev. Lett.* **128**, 073001 (2022).
- [12] K. Ono, Y. Saito, T. Ishiyama, T. Higomoto, T. Takano, Y. Takasu, Y. Yamamoto, M. Tanaka, and Y. Takahashi, *Phys. Rev. X* **12**, 021033 (2022).
- [13] S. Hofsäss, J. E. Padilla-Castillo, S. C. Wright, S. Kray, R. Thomas, B. G. Sartakov, B. Ohayon, G. Meijer, and S. Truppe, *Phys. Rev. Res.* **5**, 013043 (2023).
- [14] B. Ohayon, S. Hofsäss, J. E. Padilla-Castillo, S. C. Wright, G. Meijer, S. Truppe, K. Gibble, and B. K. Sahoo, *New J. Phys.* **24**, 123040 (2022).
- [15] A. Yamaguchi, M. S. Safronova, K. Gibble, and H. Katori, *Phys. Rev. Lett.* **123**, 113201 (2019).
- [16] L. D. Sarlo, M. Favier, R. Tyumenev, and S. Bize, *J. Phys.: Conf. Ser.* **723**, 012017 (2016).
- [17] R. Tyumenev, M. Favier, S. Bilicki, E. Bookjans, R. L. Targat, J. Lodewyck, D. Nicolodi, Y. L. Coq, M. Abgrall, J. Guéna, L. D. Sarlo, and S. Bize, *New J. Phys.* **18**, 113002 (2016).
- [18] M. Büki, D. Röser, and S. Stellmer, *Appl. Opt.* **60**, 9915 (2021).
- [19] C. Wraith, X. Yang, L. Xie, C. Babcock, J. Bieroń, J. Billowes, M. Bissell, K. Blaum, B. Cheal, L. Filippin, R. Garcia Ruiz, W. Gins, L. Grob, G. Gaigalas, M. Godefroid, C. Gorges, H. Heylen, M. Honma, P. Jönsson, S. Kaufmann *et al.*, *Phys. Lett. B* **771**, 385 (2017).
- [20] L. Xie, X. Yang, C. Wraith, C. Babcock, J. Bieroń, J. Billowes, M. Bissell, K. Blaum, B. Cheal, L. Filippin, K. Flanagan, R. Garcia Ruiz, W. Gins, G. Gaigalas, M. Godefroid, C. Gorges, L. Grob, H. Heylen, P. Jönsson, S. Kaufmann *et al.*, *Phys. Lett. B* **797**, 134805 (2019).
- [21] X. Yang, T. Cocolios, and S. Geldhof, Probing the magicity and shell evolution in the vicinity of $n = 50$ with high-resolution laser spectroscopy of $^{81,82}\text{Zn}$ isotopes (2020), CERN-INTC-2020-064 (unpublished).
- [22] Y. Liu, X. Yang, S. Bai, J. Reilly, T. Cocolios, K. Flanagan, R. G. Ruiz, F. Gustafsson, J. Li, M. Ma *et al.*, *Collinear resonance ionization spectroscopy of stable 64, 66, 67, 68, 70 Zn isotopes* (2022), ISOLDE workshop and users meeting, Contribution ID: 21 (unpublished).
- [23] W. Rasmussen, R. Schieder, and H. Walther, *Opt. Commun.* **12**, 315 (1974).
- [24] P. E. G. Baird, R. J. Brambley, K. Burnett, D. N. Stacey, D. M. Warrington, and G. K. Woodgate, *Proc. R. Soc. London. Ser. A, Math. Phys. Sci.* **365**, 567 (1979).
- [25] R. C. Brown, S. Wu, J. V. Porto, C. J. Sansonetti, C. E. Simien, S. M. Brewer, J. N. Tan, and J. D. Gillaspay, *Phys. Rev. A* **87**, 032504 (2013).
- [26] W. Hanle, *Naturwissenschaften* **11**, 690 (1923).
- [27] A. C. G. Mitchell and M. W. Zemansky, *Resonance Radiation and Excited Atoms* (Cambridge University Press, London, 1961), Chap. V.
- [28] K. J. R. Rosman and P. D. P. Taylor, *Pure Appl. Chem.* **70**, 217 (1998).
- [29] J. Kowalski and F. Träger, *Z. Phys. A* **278**, 1 (1976).
- [30] M. Crawford, A. Schawlow, W. Gray, and F. Kelly, *Can. J. Res.* **28a**, 138 (1950).
- [31] G. Hately and T. Littlefield, *J. Opt. Soc. Am.* **48**, 851 (1958).
- [32] D. Gullberg and U. Litzén, *Phys. Scr.* **61**, 652 (2000).
- [33] P. Doidge, *Spectrochimica Acta Part B: Atom. Spectrosc.* **50**, 209 (1995).
- [34] P. Campbell, J. Billowes, and I. S. Grant, *J. Phys. B: At., Mol. Opt. Phys.* **30**, 2351 (1997).
- [35] B. K. Sahoo and B. Ohayon, *Phys. Rev. Res.* **5**, 043142 (2023).
- [36] P. Plattner, E. Wood, L. A. Ayoubi, O. Beliuskina, M. L. Bissell, K. Blaum, P. Campbell, B. Cheal, R. P. de Groote, C. S. Devlin, T. Eronen, L. Filippin, R. F. G. Ruiz, Z. Ge, S. Geldhof, W. Gins, M. Godefroid, H. Heylen, M. Hukkanen, P. Imgram *et al.*, *Phys. Rev. Lett.* **131**, 222502 (2023).

List of References

As the references of this publication follows its specific numbering, the bibliography of the publication is linked to the thesis bibliography:

Ref. in publication	equivalent in thesis	Ref. in publication	equivalent in thesis
[1]	[5]	[19]	[123]
[2]	[175]	[20]	[124]
[3]	[176]	[21]	[185]
[4]	[177]	[22]	[186]
[5]	[178]	[23]	[187]
[6]	[179]	[24]	[188]
[7]	[180]	[25]	[114]
[8]	[26]	[26]	[189]
[9]	[37]	[27]	[190]
[10]	[181]	[28]	[191]
[11]	[106]	[29]	[129]
[12]	[182]	[30]	[19]
[13]	[121]	[31]	[20]
[14]	[120]	[32]	[55]
[15]	[17]	[33]	[130]
[16]	[183]	[34]	[113]
[17]	[184]	[35]	[192]
[18]	[33]	[36]	[193]

Publication: Isotope shift measurement of the 423-nm transition in neutral Ca

This section shows a reprint of the journal article [35].
Its complete citation reads

David Röser, Lukas Möller, Hans Keßler, and Simon Stellmer
Isotope shift measurement of the 423-nm line in Ca,
Phys. Rev. A **110** (2024) 032809.
DOI: <https://doi.org/10.1103/PhysRevA.110.032809>

The article is included in this dissertation with the consent of all co-authors and the permission of the American Physical Society under the terms of the Creative Commons Attribution 4.0 International license.

Contents of Publication

B.1	I. Introduction	72
B.2	II. Experimental Apparatus	72
B.3	III. Measurements	74
B.4	IV. Conclusions and Outlook	76

Isotope-shift measurement of the 423-nm transition in neutral CaDavid Röser,^{*} Lukas Möller, Hans Keßler[✉], and Simon Stellmer^{✉†}
Physikalisches Institut, Universität Bonn, Nussallee 12, 53115 Bonn, Germany (Received 10 June 2024; revised 9 August 2024; accepted 30 August 2024; published 11 September 2024)

We report on saturated absorption spectroscopy measurements of the $(4s^2)^1S_0 \rightarrow (4s4p)^1P_1$ transition for the four most abundant even-mass isotopes in calcium. By referencing the laser locked to an ultralow expansion cavity and carefully investigating systematic errors, isotope shifts are determined with a precision below 100 kHz, improving previously reported values by a factor of about 3. A King plot analysis, employing literature values of the 729-nm transition in Ca^+ ions, shows excellent linearity. The field and mass shift parameters are determined from King plots with other transitions.

DOI: [10.1103/PhysRevA.110.032809](https://doi.org/10.1103/PhysRevA.110.032809)**I. INTRODUCTION**

Laser spectroscopy plays a key role in investigating the atomic or molecular structure [1]. Over the past decades, spectroscopic techniques have been developed and improved to outstanding precision on the single Hz level [2–7]. These measurements can be used to define frequency standards or explore physics beyond the standard model, e.g., to search for temporal variations in fundamental constants [8], breaking of local Lorentz invariance [9,10], *CPT* violation [10], or a new gauge boson [5,11–17].

The term “isotope shift” refers to the energy difference of electronic states between different isotopes. The main contributions to the isotope shifts are the mass and the field shift. The mass shift originates from a change of the electron’s reduced mass and momentum correlations of electrons and is proportional to the relative mass difference between isotopes. The field shift arises from a different nuclear charge distribution due to different neutron numbers [18].

In a simplified case, the field shift is assumed to be proportional to the difference of the squared nuclear charge radii. Then, isotope shifts of different transitions in atoms or ions of the same species are linearly related to each other, when they undergo a King plot analysis [19]. The degree of observed linearity provides insights into the nuclear potential, and higher-order corrections or new physics terms might be determined [5,20].

It has been found that strong nonlinearities can occur due to large nuclear deformation. Here, the simple field shift approximation fails, as the quadratic field shift and the next-higher-order Seltzer moment have to be taken into account [5,13]. Still, the combination of various transitions in the Yb system allowed researchers to constrain the parameter space for the new boson coupling (see Refs. [6,21] and references therein).

For isotope-shift measurements, group-II elements are of particular interest. Their even-mass isotopes feature an even

number of protons and an even number of neutrons leading to zero nuclear spin. The absence of hyperfine structure circumvents center-of-gravity determinations and thus enhances measurement precision.

Among the group-II elements, calcium holds particular significance, as it offers two “doubly magic” nuclei. They feature a closed proton and a closed neutron shell, resulting in nondeformed nuclei [22]. Isotope-shift measurements on neutral or ionized Ca have been measured on numerous transitions with different methods, e.g., Refs. [3,4,7,12,15,23–29]. Especially the shifts on the $4s^2S_{1/2} \rightarrow 3d^2D_{5/2}$ quadrupole transition at 729 nm in Ca^+ have been measured with outstanding precision [3]. Reported King plots show excellent linearities, further narrowing the bounds on the coupling strength of a new possible boson [7]. An overview about previous work up to 2020 can be found in Ref. [30].

The $(4s^2)^1S_0 \rightarrow (4s4p)^1P_1$ transition in Ca I is at 423 nm with a natural linewidth of 34.5(4) MHz and saturation intensity of 54(5) mW/cm². Isotope shifts on this line have been measured with different methods, e.g., ionization spectroscopy [24] and fluorescence detection of an atomic beam [25,26]. The values reported have typical 1σ uncertainties of several hundred kHz. While the reported values of Refs. [24,26] agree in general, there remain open questions from Ref. [30] regarding the measurements and the given error budget.

In this paper, we report on a saturated absorption spectroscopy measurement in a gas cell, narrowing down the uncertainty to the sub-100-kHz range. A King plot analysis proves linearity between our measurement and isotope shifts on the 729-nm line in Ca^+ [3]. The field and mass shift coefficients for the 423-nm lines are determined from isotope-shift data on dipole transitions in Ca^+ [29].

II. EXPERIMENTAL APPARATUS**A. Optical setup**

The laser light used in the experiment is derived from an infrared diode laser system equipped with a tapered amplifier operating at 846 nm (Toptica TA pro). A vibration-isolated and temperature-stabilized ultralow expansion (ULE) cavity

^{*}Contact author: roeser@physik.uni-bonn.de[†]Contact author: stellmer@uni-bonn.de

(Menlo Systems ORC-Cubic) serves as a frequency reference. The laser undergoes a carrier shift modulation and the sideband is frequency stabilized with the Pound-Drever-Hall method to the ULE cavity. The carrier shift frequency can be tuned with a direct digital synthesis generator with a Hz level precision. The performance of the lock has been evaluated by locking two identical lasers with different carrier shifts to the same cavity mode. Their beat signal linewidth is smaller than 2 Hz on a timescale of 1 s.

The light is converted to 423 nm with second harmonic generation (SHG) in a nonlinear crystal within an optical cavity, which is locked to the laser using the Hänsch-Couillaud method [31]. A polarization-maintaining fiber is used to clean the mode profile and guide the linearly polarized light to the experiment table.

To suppress intensity noise in the experiment, the light power is measured on the experiment table. A proportional-integral-derivative controller is used to stabilize it by applying feedback on the tapered amplifier current. The locking bandwidth is measured to approximately 80 kHz, which is mainly limited by the slow response of the SHG cavity.

The laser light is split into two beams of equal intensities (1.9 mW on a Gaussian beam diameter of 4 mm), with one serving as the pump and the other as the probe beam. Saturated absorption spectroscopy is performed by sending both beams counterpropagating through a 1.5-m-long stainless steel vacuum system acting as a gas cell [1]. Lenses are slightly tilted from normal incidence, and all other optics, including the vacuum viewports, are wedged to avoid etaloning effects due to reflections or stray light impinging on the photodiodes or interacting with the probed velocity class of atoms.

A lock-in technique is employed by sinusoidal amplitude modulation of the pump beam with an acousto-optic modulator (AOM). The lock-in frequency is set to 11 kHz, as the spectral noise amplitude is minimal here and all electronic components reach the white noise floor.

The AOM is driven at a frequency of 200 MHz. Thus, interference effects between pump and probe beam are modulated much faster than the atomic linewidth. To reduce residual Doppler shifts, proper overlap of pump and probe beam is ensured by coupling the probe beam into the AOM and observing the diffraction orders [32].

The Lamb dip is measured with a photodiode followed by a low noise transimpedance amplifier (FEMTO DHPCA-100), which is then connected to a lock-in amplifier (Zurich Instruments HF2LI). The demodulated signal is low pass filtered, typically with a time constant of 5 s. Measurements are performed by shifting the laser frequency and a subsequent settling time of twice this time constant. Afterwards, the lock-in signal is recorded and used for evaluation. This procedure leads to a gain in signal-to-noise ratio of four orders of magnitude compared to unmodulated spectroscopy. A sketch of the optical setup is shown in Fig. 1.

B. Systematic effects

Five grams of naturally abundant calcium are placed into a 1.1-m-long reservoir region, which is kept at 340 °C by a

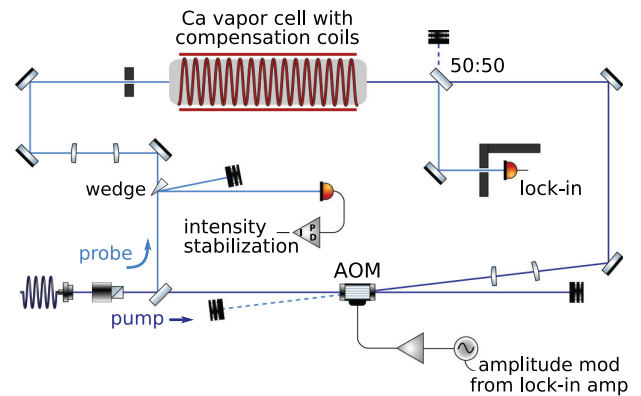


FIG. 1. Sketch of the saturated absorption spectroscopy setup.

magnetic-field-compensating heating tape. The temperature inhomogeneity is monitored with sensors and measured to be smaller than 10 °C.

The vapor pressure of Ca is estimated to be 10^{-7} mbar, leading to approximately 20 % absorption of each beam [33]. At this level, Beer-Lambert's law can be utilized to show that the combined light power of probe and pump beam remains constant within the uncertainty margin of our power measurement.

To further minimize systematic errors, any magnetic fields including the Earth's magnetic field are compensated with coils in all directions. The remaining field is significantly smaller than 5 μ T and reduces Zeeman splitting and thus polarization dependent effects.

Residual Doppler shifts can be estimated with the geometric overlap of pump and probe. We estimate that the separation is smaller than 10 μ m on a traveling path of 3 m. We estimate an upper bound on the Doppler shift of 10 kHz. The second-order Doppler effect shifts the lines by less than 1 kHz and is thus neglected in the analysis of our measurement.

In test measurements, pump and probe beam have been deliberately set to a significant power imbalance to enhance light pressure-induced modifications of the atomic velocity distribution. This results in line-shape asymmetry, which can be characterized by incorporating a dispersive function into the Lorentzian profile [34]. The asymmetry is suppressed by filling the cell with 1-mbar argon buffer gas to restore the Maxwell-Boltzmann distribution by "strong" collisions. In strong collisions, the change of velocity is approximately on the order of v_0 , where v_0 represents the velocity of the class of atoms interacting with the pump beam. In precision measurements, it is essential to exercise caution in selecting the type of buffer gas, as a too high number of "weak" collisions may cause a Gaussian line shape of the Lamb dip [35]. Additionally, by ensuring equal intensity between probe and pump beam, the net momentum transfer on the atoms is minimized. Thus, we can effectively avoid this asymmetry.

Ca-Ar collisions cause a line broadening γ_c and a shift δ_c [36,37]. While the broadening insignificantly deteriorates the line center determination, the shift has to be corrected for. For

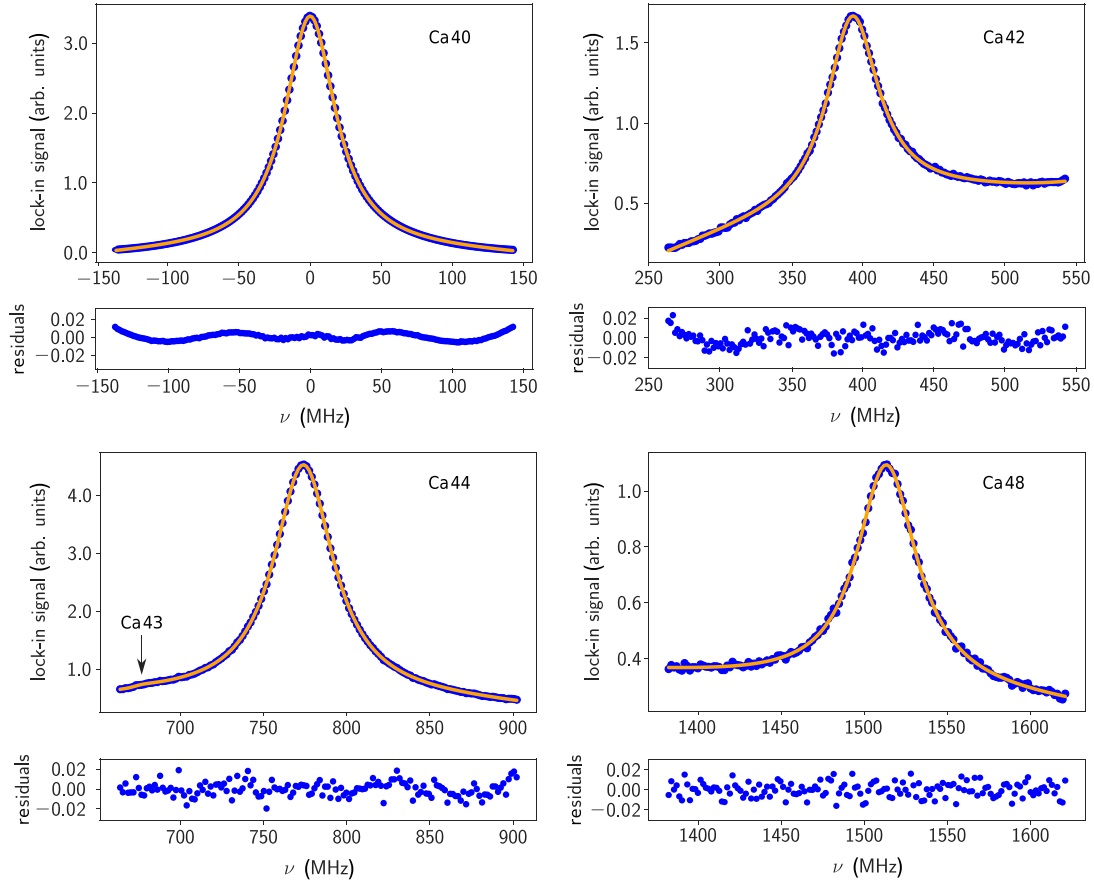


FIG. 2. The figure shows the demodulated and low pass filtered lock-in signal exhibiting the measured Lamb dips of ^{40}Ca , ^{42}Ca , ^{44}Ca , and ^{48}Ca including the fit residuals. ν denotes the frequency offset from ^{40}Ca in natural frequencies, while the lock-in signal is depicted in arbitrary units. The resonances are scaled by a factor of 100, 50, and 300 for ^{42}Ca , ^{44}Ca , and ^{48}Ca , respectively, and the offset is adjusted for better visibility.

our measurement, it is determined as

$$\delta_c = \sigma_{\text{Ca-Ar}} \bar{v} n_{\text{Ar}}, \quad (1)$$

where $\sigma_{\text{Ca-Ar}}$ denotes the collisional cross section, which is precisely measured in Ref. [38], \bar{v} denotes the mean relative collision velocity, and n_{Ar} denotes the argon density. For each Ca isotope, we calculate

$$\bar{v} = \sqrt{8k_B T / (3\pi m_{\text{red}})} \quad (2)$$

with

$$m_{\text{red}} = M_A m_{\text{Ar}} / (M_A + m_{\text{Ar}}) \quad (3)$$

to accommodate the specific velocity distribution of each isotope A with its mass M_A [36,37].

Recoil effects are not measurable, as the atomic linewidth is much larger than the recoil splitting of the line. With Ref. [39], it can be shown that the recoil splitting is symmetrical around the resonance up to 800 Hz. We expect this to be the common mode for all resonances, but nevertheless an error of 1 kHz is added to the uncertainty margin.

III. MEASUREMENTS

A. Modified Lorentzian line shape

It has been shown in previous theoretical and experimental work that the Lamb dip profile is modified in the presence of collisions and thus exhibits asymmetry [40–42]. This originates from a finite collision time resulting in failure of the impact approximation, which requires $T_d \Delta \ll 1$. Here, T_d denotes the finite collision time and $\Delta = \nu - \nu_0$ the laser detuning from the atomic resonance ν_0 [42]. The actual line shape that is used to evaluate the data from this experiment thus reads

$$I(\Delta) \propto \frac{\gamma_N + \gamma_c(\Delta)}{\Delta^2 + [\gamma_N + \gamma_c(0)]^2} \quad (4)$$

with

$$\gamma_c(\Delta) = \gamma_c(0)(1 + a_1 \Delta T_d), \quad (5)$$

whereas γ_N is the natural linewidth, a_1 is a potential-dependent parameter, and $\gamma_c(0)$ is the collisional broadening from the impact approximation [40,41].

The fit of ^{40}Ca (see Fig. 2) exhibits small and symmetric but systematic residuals. The accuracy of the fitted line center is investigated by deliberately fitting inaccurate fit models like a modified Gaussian function that increases the residuals by a factor of 50 without altering their shape. We find that the extracted line centers agree with our model and consider the fit to be correct. For other isotopes, the residuals are dominated by noise and show much weaker systematic deviations. Other possible fit models like (generalized) Voigt profiles and a Hartmann-Tran profile [43–45] show either similar residuals or do not fully converge.

For all isotopes, the background is approximated by a second-order polynomial. This accounts for the fact that the resonances of all isotopes lie on the far wing of ^{40}Ca and that all other isotopes add a small background to the ^{40}Ca resonance. While a first-order polynomial leads to a systematic trend in the residuals noticeable with a linear fit, a third-order polynomial worsens the fit convergence without altering the line centers within their errors. Further, it turns out that an additional background term is needed for ^{42}Ca , as the wings of ^{43}Ca and ^{44}Ca contribute significantly to the background seen at the position of the ^{42}Ca resonance. This term is identified by a comprehensive scan over the resonances of ^{42}Ca , ^{43}Ca , and ^{44}Ca and a heuristic fit, which is optimized to describe the shape of the wings most precisely at the position of ^{42}Ca . Using a purely second-order polynomial background, the fitted line center of ^{42}Ca would shift by 55 kHz to higher frequencies and the residuals would exhibit a significant trend on the wings. Additionally, one hyperfine transition of ^{43}Ca falls within the scan range of ^{44}Ca . This is accounted for by adding a second resonance in the fit, which shifts the line center of ^{44}Ca by approximately 15 kHz.

B. Lamb dip measurement

In this paper, the Lamb dips of ^{40}Ca , ^{42}Ca , ^{44}Ca , and ^{48}Ca are measured. Their abundances are 97.0, 0.6, 2.1, and 0.2 %, respectively. The hyperfine components of ^{43}Ca are not determined, as the lines are not well separated from the crossover resonances. The abundance of ^{46}Ca is 0.004 %, which is too low to determine its line center with competitive precision [46].

Each isotope undergoes multiple scans in opposite directions to confirm that the measurement does not suffer from systematics arising from too tight low pass filter settings in the lock-in amplifier. For each scan, Eq. (4) is fitted more than 100 times to the data, each time with a different fit range to analyze further systematic fit errors. The ranges are both symmetrically and asymmetrically varied between $0.5 \times \text{FWHM} < |\Delta| < 3 \times \text{FWHM}$. The extracted line centers are averaged and the standard deviation of their distribution is considered as the statistical error of this scan. The experimental stability is confirmed, as the line centers for each scan are equal within their uncertainty interval, which are around 25, 160, 90, and 120 kHz for ^{40}Ca , ^{42}Ca , ^{44}Ca , and ^{48}Ca , respectively. In total, there are four scans for ^{42}Ca and ^{44}Ca and three for ^{48}Ca . In between scans of ^{42}Ca , ^{44}Ca , and ^{48}Ca , which take around 1 h, the resonance frequency of ^{40}Ca is determined to ensure that the measurement precision does not suffer from drifts of the ULE cavity resonance, which are well below 30 kHz d^{-1} .

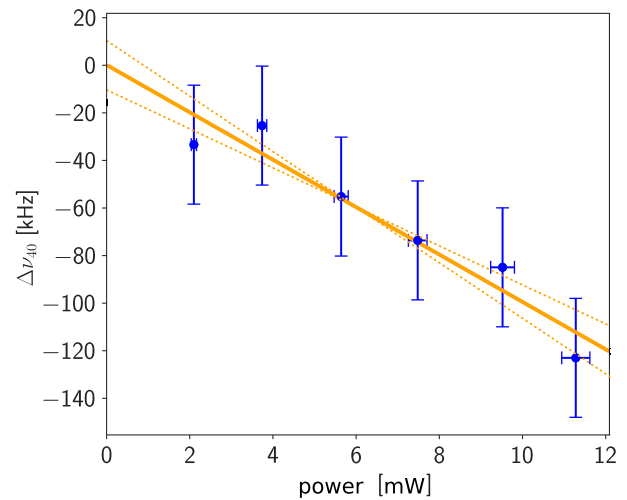


FIG. 3. The resonance of ^{40}Ca is measured for different light powers and is shown as deviation from the extrapolated line center at zero intensity. An error of 2 % is estimated for the power measurement, while the displayed uncertainty of $\Delta\nu_{40}$ originates from the fit.

Thus, the cavity drift does not add a correction term, but contributes with 1 kHz to the uncertainty budget of the isotope shifts.

As the absorption coefficient exhibits the Doppler broadened profile, the light absorption within the cell differs among the isotopes. Hence, the total power of pump and probe beam as well as their power imbalance within the cell alter for different isotopes. To account for possible errors, the resonance frequency of ^{40}Ca is measured for different light powers. The data are shown in Fig. 3. By fitting a linear function, the slope is determined to be $-10.0(1.5) \text{ kHz}/(\text{mW}/\text{cm}^2)$. Measurements on the other isotopes agree with this value. The resonance frequencies are corrected by determining the total light power in the cell during the measurement and extrapolating the resonance frequencies to zero power. The corrections on the isotope shifts are smaller than 10 kHz and thus are one order of magnitude lower than the statistical errors. Compared to Ref. [26], our slope is approximately a factor of 5 lower in absolute value indicating that our experiment is less prone to power-dependent systematic errors. To improve the precision of our measurements, a more elaborate work on power-dependent shifts would be necessary to rule out all possible sources of shifts, which goes beyond the scope of this paper. Using all dipole transitions listed in the NIST atomic spectra database [47], the influence of the AC Stark shift is calculated to be approximately $35 \text{ mHz}/(\text{mW}/\text{cm}^2)$ and thus excluded as a possible origin. A possible explanation might be an incomplete cancellation of the light pressure-induced changes in the velocity distribution. Although the line shape appears symmetric and the amplitude of the dispersive function is minimal, it can still shift the observed resonance frequency on the parts-per-thousand scale of the linewidth.

Our measured isotope shifts are presented in Table I. The results for ^{44}Ca and ^{48}Ca agree well with Ref. [24]. However, there is a discrepancy for ^{42}Ca , which might arise from the

TABLE I. Measured isotope shifts relative to ^{40}Ca compared with previously reported values. All values are in MHz.

Isotope	This paper	[26]	[24]
^{42}Ca	393.09(9)	393.1(4)	393.50(10)
^{44}Ca	773.81(5)	773.8(2)	773.80(15)
^{48}Ca	1512.99(7)	1513.1(4)	1513.00(20)

exclusion of the ^{43}Ca hyperfine lines from the fit, as stated in Ref. [24]. However, our measurement agrees for all isotopes with Ref. [26]. The uncertainty ranges of our measurement are smaller by a factor of about 5 compared to Ref. [26], but only a factor of 3 lower than the measurements presented in Ref. [24]. The corrections, corresponding to the systematic effects in our measurement, and the uncertainty budget (exemplified for ^{42}Ca) are displayed in Table II. The Lamb dips including the fits and the respective residuals are shown for each isotope in Fig. 2.

C. King plot analysis

To further investigate our data, a King plot analysis is performed, as shown in Fig. 4. We use isotope shifts of the $4s\ ^2S_{1/2} \rightarrow 3d\ ^2D_{5/2}$ quadrupole transition at 729 nm in trapped Ca^+ with uncertainties below 10 Hz [3].

In our King plots, modified isotope shifts $m\delta_{729\text{nm}}$ are plotted against our measurement $m\delta_{423\text{nm}}$, with the actual shift being scaled by $g^{A,A'} = (1/m_{A'} - 1/m_A)^{-1}$. Here, m_A and $m_{A'}$ denote the nuclear masses of the respective isotopes A and A' [20]. For each isotope, the masses are calculated from the respective atomic mass [48] as

$$m_{\text{nucleus}} = m_{\text{atom}} - 20m_e + \sum_{i=1}^{20} E_i^{\text{bind}}. \quad (6)$$

Here, m_e denotes the electron mass and E_i^{bind} the binding energy of each electron i , which is derived from the NIST database [12,47].

A linear function

$$m\delta_{729\text{nm}} = K_{729\text{nm}} - \frac{F_{729\text{nm}}}{F_{423\text{nm}}} K_{423\text{nm}} + \frac{F_{729\text{nm}}}{F_{423\text{nm}}} m\delta_{423\text{nm}} \quad (7)$$

is fitted to the data, with F_i and K_i the field and mass shift parameters of the transition i , respectively [20].

TABLE II. Corrections and uncertainties of the isotope-shift measurement, exemplified for ^{42}Ca .

Source	Correction (kHz)	Uncertainty (kHz)
Residual Doppler	0	10
Second-order Doppler	0.2	0.0
Atomic recoil	0	1
Power dependence	0.7	0
Zeeman effect	0	0
Collisions	37	0.3
Cavity drift	0	1
Statistical error	0	85

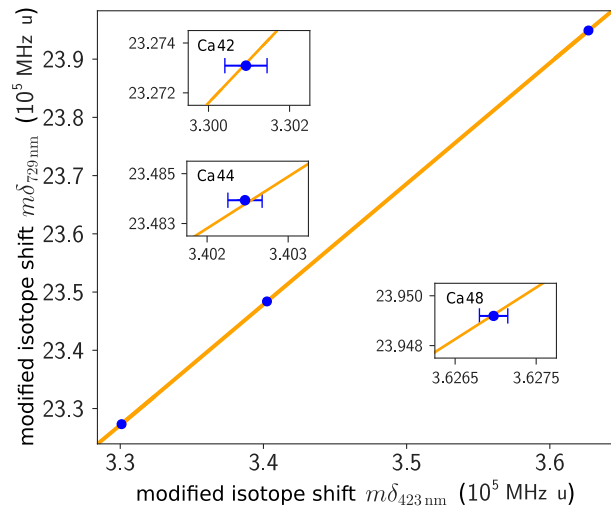


FIG. 4. King plot generated with our measurements and isotope shifts of the $4s\ ^2S_{1/2} \rightarrow 3d\ ^2D_{5/2}$ transition at 729 nm in trapped Ca^+ [3]. The error bars of $\delta m_{729\text{nm}}$ are too small to be visible.

Our King plot reveals an excellent linearity between our measurement and Ref. [3], as the line intersects all uncertainty intervals of our data points. This suggests reliability of our data, as the linearity of Ref. [3] is proven with another sub-10-Hz-accuracy measurement in Ref. [7]. From the fit, we find $F_{729\text{nm}}/F_{423\text{nm}} = 2.073\ 36(85)$ and $K_{729\text{nm}} - (F_{729\text{nm}}/F_{423\text{nm}})K_{423\text{nm}} = 16.4290(29) \times 10^5$ MHz u.

From isotope-shift measurements of the $^2S_{1/2} \rightarrow ^2P_{1/2}$ and $^2D_{3/2} \rightarrow ^2P_{1/2}$ transitions in trapped Ca^+ , Ref. [29] determines the field and mass shift coefficients for the respective transitions. Using their data to perform a King plot analysis, we can deduce the field and mass shift coefficients $F_{423\text{nm}} = -178.4(3.2)$ MHz/fm² and $K_{423\text{nm}} = 363.6(1.4)$ GHz u. To prove consistency, we have fitted our data against the mean-squared charge radii difference $\Delta\langle r_{A,A'}^2 \rangle$ [30], as $m\delta_{423\text{nm}} = K_{423\text{nm}} + F_{423\text{nm}} \Delta\langle r_{A,A'}^2 \rangle$: We obtain $F_{423\text{nm}} = -181.8(7.3)$ MHz/fm² and $K_{423\text{nm}} = 362.7(0.9)$ GHz u.

IV. CONCLUSIONS AND OUTLOOK

We have reported isotope shifts for the most abundant isotopes, ^{42}Ca , ^{44}Ca , and ^{48}Ca , relative to ^{40}Ca . Our measurement reduces the uncertainty by a factor of roughly 3 compared to Ref. [24], lowering it to the parts-per-thousand scale of the linewidth.

By performing a King plot analysis with data from Ref. [3], we find excellent linearity. Furthermore, by comparison to the field and mass shift parameters determined in Ref. [29], the field and mass shift constants are calculated for the 423-nm line.

For future measurements, different spectroscopic techniques, e.g., polarization spectroscopy, will be applied to evaluate their signal-to-noise performance compared to saturated-absorption spectroscopy [49]. For this, detailed studies about the line shape in the presence of collisions have to be performed. Further, also double modulation schemes with an amplitude-modulated pump beam in modulation

transfer spectroscopy can be applied. This is advantageous, as the frequency can be modulated with several hundred MHz.

Further, changing to copropagating pump and probe beams eliminates the crossover resonances and allows for precise determination of the hyperfine coupling constants in ^{43}Ca [50].

ACKNOWLEDGMENTS

We acknowledge fruitful discussions with W. Alt and F. Vewinger and thank F. Wenger and A. Hamer for

assistance in the setup and operation of the experiment. Financial support from Deutsche Forschungsgemeinschaft through the Cluster of Excellence ML4Q (EXC2004/1 Grant No. 390534769) and Projects No. 496941189 and No. INST 217/978-1 FUGG, as well as from BMBF (Project No. 13N16371 QuantumGuide), is gratefully acknowledged. Further, H.K. and S.S. acknowledge funding by the state of North Rhine–Westphalia through the EIN Quantum NRW program. Experimental data will be made available upon reasonable request.

-
- [1] W. Demtröder, *Laser Spectroscopy 2: Experimental Techniques* (Springer-Verlag, Berlin, 2015).
- [2] A. D. Ludlow, M. M. Boyd, J. Ye, E. Peik, and P. O. Schmidt, *Rev. Mod. Phys.* **87**, 637 (2015).
- [3] F. W. Knollmann, A. N. Patel, and S. C. Doret, *Phys. Rev. A* **100**, 022514 (2019).
- [4] P. Micke, T. Leopold, S. A. King, E. Benkler, L. J. Spieß, L. Schmöger, M. Schwarz, J. R. C. López-Urrutia, and P. O. Schmidt, *Nature (London)* **578**, 60 (2020).
- [5] J. Hur, D. P. L. Aude Craik, I. Counts, E. Knyazev, L. Caldwell, C. Leung, S. Pandey, J. C. Berengut, A. Geddes, W. Nazarewicz, P.-G. Reinhard, A. Kawasaki, H. Jeon, W. Jhe, and V. Vuletić, *Phys. Rev. Lett.* **128**, 163201 (2022).
- [6] K. Ono, Y. Saito, T. Ishiyama, T. Higomoto, T. Takano, Y. Takasu, Y. Yamamoto, M. Tanaka, and Y. Takahashi, *Phys. Rev. X* **12**, 021033 (2022).
- [7] T. T. Chang, B. B. Awazi, J. C. Berengut, E. Fuchs, and S. C. Doret, *Phys. Rev. A* **110**, L030801 (2024).
- [8] J. C. Berengut, V. V. Flambaum, and E. M. Kava, *Phys. Rev. A* **84**, 042510 (2011).
- [9] L. S. Dreissen, C. H. Yeh, H. A. Fürst, K. C. Grensemann, and T. E. Mehlstäubler, *Nat. Commun.* **13**, 7314 (2022).
- [10] B. Ohayon, G. Janka, I. Cortinovis, Z. Burkley, L. de Sousa Borges, E. Depero, A. Golovizin, X. Ni, Z. Salman, A. Suter, C. Vigo, T. Prokscha, and P. Crivelli (Mu-MASS Collaboration), *Phys. Rev. Lett.* **128**, 011802 (2022).
- [11] C. Delaunay, R. Ozeri, G. Perez, and Y. Soreq, *Phys. Rev. D* **96**, 093001 (2017).
- [12] C. Solaro, S. Meyer, K. Fisher, J. C. Berengut, E. Fuchs, and M. Drewsen, *Phys. Rev. Lett.* **125**, 123003 (2020).
- [13] I. Counts, J. Hur, D. P. L. Aude Craik, H. Jeon, C. Leung, J. C. Berengut, A. Geddes, A. Kawasaki, W. Jhe, and V. Vuletić, *Phys. Rev. Lett.* **125**, 123002 (2020).
- [14] J. C. Berengut, C. Delaunay, A. Geddes, and Y. Soreq, *Phys. Rev. Res.* **2**, 043444 (2020).
- [15] N.-H. Rehbehn, M. K. Rosner, H. Bekker, J. C. Berengut, P. O. Schmidt, S. A. King, P. Micke, M. F. Gu, R. Müller, A. Surzhykov, and J. R. C. López-Urrutia, *Phys. Rev. A* **103**, L040801 (2021).
- [16] N. L. Figueroa, J. C. Berengut, V. A. Dzuba, V. V. Flambaum, D. Budker, and D. Antypas, *Phys. Rev. Lett.* **128**, 073001 (2022).
- [17] R. M. Potvliege, A. Nicolson, M. P. A. Jones, and M. Spannowsky, *Phys. Rev. A* **108**, 052825 (2023).
- [18] V. V. Flambaum, A. J. Geddes, and A. V. Viatkina, *Phys. Rev. A* **97**, 032510 (2018).
- [19] W. H. King, *J. Opt. Soc. Am.* **53**, 638 (1963).
- [20] J. C. Berengut, D. Budker, C. Delaunay, V. V. Flambaum, C. Frugiuele, E. Fuchs, C. Grojean, R. Harnik, R. Ozeri, G. Perez, and Y. Soreq, *Phys. Rev. Lett.* **120**, 091801 (2018).
- [21] M. Door *et al.*, [arXiv:2403.07792](https://arxiv.org/abs/2403.07792).
- [22] H. Nakada, *Phys. Rev. C* **100**, 044310 (2019).
- [23] A. Mortensen, J. J. T. Lindballe, I. S. Jensen, P. Staunum, D. Voigt, and M. Drewsen, *Phys. Rev. A* **69**, 042502 (2004).
- [24] W. Nörtershäuser, N. Trautmann, K. Wendt, and B. Bushaw, *Spectrochim. Acta, Part B* **53**, 709 (1998).
- [25] A. Andl, K. Bekk, S. Göring, A. Hanser, G. Nowicki, H. Rebel, G. Schatz, and R. C. Thompson, *Phys. Rev. C* **26**, 2194 (1982).
- [26] E. J. Salumbides, V. Maslinskas, I. M. Dildar, A. L. Wolf, E.-J. van Duijn, K. S. E. Eikema, and W. Ubachs, *Phys. Rev. A* **83**, 012502 (2011).
- [27] C. Shi, F. Gebert, C. Gorges, S. Kaufmann, W. Nörtershäuser, B. K. Sahoo, A. Surzhykov, V. A. Yerokhin, J. C. Berengut, F. Wolf, J. C. Heip, and P. O. Schmidt, *Appl. Phys. B* **123**, 2 (2017).
- [28] P. Müller, K. König, P. Imgram, J. Krämer, and W. Nörtershäuser, *Phys. Rev. Res.* **2**, 043351 (2020).
- [29] F. Gebert, Y. Wan, F. Wolf, C. N. Angstmann, J. C. Berengut, and P. O. Schmidt, *Phys. Rev. Lett.* **115**, 053003 (2015).
- [30] A. Kramida, *At. Data Nucl. Data Tables* **133**, 101322 (2020).
- [31] T. W. Hänsch and B. Couillaud, *Opt. Commun.* **35**, 441 (1980).
- [32] S. E. Park, H. S. Lee, T. Y. Kwon, and H. Cho, *Opt. Commun.* **192**, 49 (2001).
- [33] C. B. Alcock, V. P. Itkin, and M. K. Horrigan, *Canadian Metallurgical Quarterly* **23**, 309 (1984).
- [34] R. Grimm and J. Mlynek, *Phys. Rev. Lett.* **63**, 232 (1989).
- [35] J. Tenenbaum, E. Miron, S. Lavi, J. Liran, M. Strauss, J. Oreg, and G. Erez, *J. Phys. B* **16**, 4543 (1983).
- [36] W. Hindmarsh and J. M. Farr, *Prog. Quantum Electron.* **2**, 141 (1973).
- [37] J. M. Farr and W. R. Hindmarsh, *J. Phys. B* **4**, 568 (1971).
- [38] G. Smith, *J. Phys. B* **5**, 2310 (1972).
- [39] J. L. Hall, C. J. Bordé, and K. Uehara, *Phys. Rev. Lett.* **37**, 1339 (1976).
- [40] R. E. Walkup, A. Spielfiedel, and D. E. Pritchard, *Phys. Rev. Lett.* **45**, 986 (1980).
- [41] R. Walkup, B. Stewart, and D. E. Pritchard, *Phys. Rev. A* **29**, 169 (1984).
- [42] R. Ciurylo, J. Szudy, and R. S. Trawifiski, *J. Quant. Spectrosc. Radiat. Transfer* **57**, 551 (1997).

- [43] N. Ngo, D. Lisak, H. Tran, and J.-M. Hartmann, *J. Quant. Spectrosc. Radiat. Transfer* **129**, 89 (2013).
- [44] H. Tran, N. Ngo, and J.-M. Hartmann, *J. Quant. Spectrosc. Radiat. Transfer* **129**, 199 (2013).
- [45] H. Tran, N. Ngo, and J.-M. Hartmann, *J. Quant. Spectrosc. Radiat. Transfer* **134**, 104 (2014).
- [46] F. Kondev, M. Wang, W. Huang, S. Naimi, and G. Audi, *Chin. Phys. C* **45**, 030001 (2021).
- [47] A. Kramida, Yu. Ralchenko, J. Reader, and NIST ASD Team, NIST Atomic Spectra Database, version 5.11, 2023.
- [48] M. Wang, G. Audi, F. G. Kondev, W. J. Huang, S. Naimi, and X. Xing, *Chin. Phys. C* **41**, 030003 (2017).
- [49] G. C. Bjorklund and E. A. Whittaker, *J. Phys. Chem. A* **125**, 8519 (2021).
- [50] A. Banerjee and V. Natarajan, *Opt. Lett.* **28**, 1912 (2003).

List of References

As the references of this publication follows its specific numbering, the bibliography of the publication is linked to the thesis bibliography:

Ref. in publication	equivalent in thesis	Ref. in publication	equivalent in thesis
[1]	[140]	[26]	[131]
[2]	[5]	[27]	[199]
[3]	[21]	[28]	[200]
[4]	[194]	[29]	[201]
[5]	[23]	[30]	[202]
[6]	[182]	[31]	[89]
[7]	[195]	[32]	[149]
[8]	[27]	[33]	[203]
[9]	[30]	[34]	[135]
[10]	[29]	[35]	[204]
[11]	[109]	[36]	[141]
[12]	[110]	[37]	[142]
[13]	[22]	[38]	[143]
[14]	[28]	[39]	[138]
[15]	[111]	[40]	[145]
[16]	[106]	[41]	[146]
[17]	[112]	[42]	[144]
[18]	[25]	[43]	[205]
[19]	[107]	[44]	[206]
[20]	[26]	[45]	[207]
[21]	[196]	[46]	[50]
[22]	[197]	[47]	[137]
[23]	[198]	[48]	[208]
[24]	[132]	[49]	[209]
[25]	[133]	[50]	[210]

Bibliography

- [1] L. Essen and J. V. L. Parry, *The caesium resonator as a standard of frequency and time*, Philos. Trans. R. Soc. London. Ser. A **250** (1957) 45, URL: <https://dx.doi.org/10.1098/rsta.1957.0010> (cit. on p. 1).
- [2] B. I. des Poids et Mesures, *The International System of Units (SI)*, SI Brochure (2024), URL: <https://www.bipm.org/en/publications/mises-en-pratique> (cit. on p. 1).
- [3] A. Aeppli, K. Kim, W. Warfield, M. S. Safronova and J. Ye, *Clock with 8×10^{-19} Systematic Uncertainty*, Phys. Rev. Lett. **133** (2024) 023401, URL: <https://dx.doi.org/10.1103/PhysRevLett.133.023401> (cit. on pp. 1, 6, 9–11).
- [4] N. Huntemann, C. Sanner, B. Lipphardt, C. Tamm and E. Peik, *Single-Ion Atomic Clock with 3×10^{-18} Systematic Uncertainty*, Phys. Rev. Lett. **116** (2016) 063001, URL: <https://doi.org/10.1103/PhysRevLett.116.063001> (cit. on p. 1).
- [5] A. D. Ludlow, M. M. Boyd, J. Ye, E. Peik and P. O. Schmidt, *Optical atomic clocks*, Rev. Mod. Phys. **87** (2015) 637, URL: <https://doi.org/10.1103/RevModPhys.87.637> (cit. on pp. 1, 6, 12, 70, 79).
- [6] E. Kaplan and C. Hegarty, *Understanding Gps: Principles and Applications*, 2nd ed., Artech House, 2005, ISBN: 9781580538947 (cit. on p. 1).
- [7] J. Grotti, S. Koller, S. Vogt et al., *Geodesy and metrology with a transportable optical clock*, Nat. Phys. **14** (2018) 437, URL: <https://doi.org/10.1038/s41567-017-0042-3> (cit. on p. 1).
- [8] C. Lisdat et al., *A clock network for geodesy and fundamental science*, Nat. Commun. **7** (2016) 12443 (cit. on p. 1).
- [9] V. A. Dzuba and A. Derevianko, *Blackbody radiation shift for the $^1S_0 - ^3P_0$ optical clock transition in zinc and cadmium atoms*, J. Phys. B: At. Mol. Opt. Phys. **52** (2019) 215005, URL: <https://dx.doi.org/10.1088/1361-6455/ab4434> (cit. on pp. 1, 11, 12).
- [10] G. Wang and A. Ye, *Possibility of using Zn as the quantum absorber for a laser-cooled neutral atomic optical frequency standard*, Phys. Rev. A **76** (2007) 043409, URL: <https://doi.org/10.1103/PhysRevA.76.043409> (cit. on pp. 1, 7–10).

- [11] A. Witte, T. Kisters, F. Riehle and J. Helmcke, *Laser cooling and deflection of a calcium atomic beam*, J. Opt. Soc. Am. B **9** (1992) 1030, URL: <https://dx.doi.org/10.1364/JOSAB.9.001030> (cit. on p. 1).
- [12] N. Beverini et al., *Evidence for laser cooling in a magnesium atomic beam*, Opt. Lett. **14** (1989) 350, URL: <https://dx.doi.org/10.1364/OL.14.000350> (cit. on p. 1).
- [13] D. B. Fim, *First Optical Lattice Frequency Standard Based on ^{24}Mg Atoms*, PhD thesis: Gottfried Wilhelm Leibniz Universität Hannover, 2021 (cit. on p. 1).
- [14] T. Kurosu and F. Shimizu, *Laser Cooling and Trapping of Calcium and Strontium*, Jpn. J. Appl. Phys. **29** (1990) L2127, URL: <https://dx.doi.org/10.1143/JJAP.29.L2127> (cit. on p. 1).
- [15] F. M. J. Cozijn et al., *Laser cooling of beryllium ions using a frequency-doubled 626 nm diode laser*, Opt. Lett. **38** (2013) 2370, URL: <https://dx.doi.org/10.1364/OL.38.002370> (cit. on p. 1).
- [16] M. Fan, C. A. Holliman, A. L. Wang and A. M. Jayich, *Laser Cooling of Radium Ions*, Phys. Rev. Lett. **122** (2019) 223001 (cit. on p. 1).
- [17] A. Yamaguchi, M. S. Safronova, K. Gibble and H. Katori, *Narrow-line Cooling and Determination of the Magic Wavelength of Cd*, Phys. Rev. Lett. **123** (2019) 113201, URL: <https://doi.org/10.1103/PhysRevLett.123.113201> (cit. on pp. 1, 57, 70).
- [18] R. Tyumenev, *Mercury lattice clock : from the Lamb-Dicke spectroscopy to stable clock operation*, PhD thesis: Université Pierre et Marie Curie - Paris VI, 2015 (cit. on p. 1).
- [19] M. F. Crawford, A. L. Schawlow, W. M. Gray and F. M. Kelly, *ISOTOPE SHIFT IN THE RESONANCE LINES OF ZINC*, Can. J. Res. **28a** (1950) 138, URL: <https://doi.org/10.1139/cjr50a-012> (cit. on pp. 2, 29, 35, 70).
- [20] G. F. Hatley and T. A. Littlefield, *Isotope Shift in the Arc Spectrum of Zinc*, J. Opt. Soc. Am. **48** (1958) 851, URL: <https://doi.org/10.1364/JOSA.48.000851> (cit. on pp. 2, 29, 35, 70).
- [21] F. W. Knollmann, A. N. Patel and S. C. Doret, *Part-per-billion measurement of the $4^2S_{1/2} \rightarrow 3^2D_{5/2}$ electric-quadrupole-transition isotope shifts between $^{42,44,48}\text{Ca}^+$ and $^{40}\text{Ca}^+$* , Phys. Rev. A **100** (2019) 022514, URL: <https://doi.org/10.1103/PhysRevA.100.022514> (cit. on pp. 2, 24, 42, 43, 79).
- [22] I. Counts et al., *Evidence for Nonlinear Isotope Shift in Yb^+ Search for New Boson*, Phys. Rev. Lett. **125** (2020) 123002, URL: <https://doi.org/10.1103/PhysRevLett.125.123002> (cit. on pp. 2, 24, 79).
- [23] J. Hur et al., *Evidence of Two-Source King Plot Nonlinearity in Spectroscopic Search for New Boson*, Phys. Rev. Lett. **128** (2022) 163201, URL: <https://doi.org/10.1103/PhysRevLett.128.163201> (cit. on pp. 2, 79).

-
- [24] W. Demtroder, *Experimentalphysik 2: Elektrizität und Optik*, 7, korr. und erw. Aufl 2017th edition, Springer Berlin Heidelberg, 2018, ISBN: 9783662557891 (cit. on pp. 2, 13, 38).
- [25] V. V. Flambaum, A. J. Geddes and A. V. Viatkina, *Isotope shift, nonlinearity of King plots, and the search for new particles*, Phys. Rev. A **97** (2018) 032510, URL: <https://doi.org/10.1103/PhysRevA.97.032510> (cit. on pp. 2, 23, 24, 79).
- [26] J. C. Berengut et al., *Probing New Long-Range Interactions by Isotope Shift Spectroscopy*, Phys. Rev. Lett. **120** (2018) 091801, URL: <https://doi.org/10.1103/PhysRevLett.120.091801> (cit. on pp. 2, 70, 79).
- [27] J. C. Berengut, V. V. Flambaum and E. M. Kava, *Search for variation of fundamental constants and violations of fundamental symmetries using isotope comparisons*, Phys. Rev. A **84** (2011) 042510, URL: <https://doi.org/10.1103/PhysRevA.84.042510> (cit. on pp. 2, 79).
- [28] J. C. Berengut, C. Delaunay, A. Geddes and Y. Soreq, *Generalized King linearity and new physics searches with isotope shifts*, Phys. Rev. Res. **2** (2020) 043444, URL: <https://doi.org/10.1103/PhysRevResearch.2.043444> (cit. on pp. 2, 24, 79).
- [29] B. Ohayon et al., *Precision Measurement of the Lamb Shift in Muonium*, Phys. Rev. Lett. **128** (2022) 011802, URL: <https://doi.org/10.1103/PhysRevLett.128.011802> (cit. on pp. 2, 79).
- [30] L. S. Dreissen, C. H. Yeh, H. A. Füst, K. C. Grensemann and T. E. Mehlstäubler, *Improved bounds on Lorentz violation from composite pulse Ramsey spectroscopy in a trapped ion*, Nat. Commun. **13** (2022) 7314, URL: <https://doi.org/10.1038/s41467-022-34818-0> (cit. on pp. 2, 79).
- [31] M. A. Vöhringer Carrera, *Laser spectroscopy of zinc*, MA thesis: Rheinische Friedrich-Wilhelms-Universität Bonn, 2022 (cit. on pp. 2, 13, 14, 17).
- [32] M. Büki, *A Frequency Quintupled Laser for Spectroscopy of the Clock Transition of Zinc*, MA thesis: Rheinische Friedrich-Wilhelms-Universität Bonn, 2020 (cit. on pp. 2, 12, 18).
- [33] M. Büki, D. Röser and S. Stellmer, *Frequency-quintupled laser at 308 nm for atomic physics applications*, Appl. Opt. **60** (2021) 9915, URL: <https://doi.org/10.1364/AO.438793> (cit. on pp. 2, 12, 17, 18, 70).
- [34] D. Röser et al., *Hyperfine structure and isotope shifts of the $(4s^2)^1S_0 \rightarrow (4s4p)^1P_1$ transition in atomic zinc*, Phys. Rev. A **109** (2024) 012806, URL: <https://dx.doi.org/10.1103/PhysRevA.109.012806> (cit. on pp. 2, 8, 30, 32, 34, 36, 61).
- [35] D. Röser, L. Möller, H. Keßler and S. Stellmer, *Isotope-shift measurement of the 423-nm transition in neutral Ca*, Phys. Rev. A **110** (2024) 032809, URL: <https://doi.org/10.1103/PhysRevA.110.032809> (cit. on pp. 2, 38–40, 43, 71).

- [36] J. Ye, L.-S. Ma and J. L. Hall, *Ultrasensitive detections in atomic and molecular physics: demonstration in molecular overtone spectroscopy*, *J. Opt. Soc. Am. B* **15** (1998) 6, URL: <https://doi.org/10.1364/JOSAB.15.000006> (cit. on pp. 2, 37, 45).
- [37] H. Miyake, N. C. Pisenti, P. K. Elgee, A. Sitaram and G. K. Campbell, *Isotope-shift spectroscopy of the $^1S_0 \rightarrow ^3P_1$ and $^1S_0 \rightarrow ^3P_0$ transitions in strontium*, *Phys. Rev. Res.* **1** (2019) 033113, URL: <https://doi.org/10.1103/PhysRevResearch.1.033113> (cit. on pp. 3, 70).
- [38] D. G. Matei et al., *1.5 μ m Lasers with Sub-10 mHz Linewidth*, *Phys. Rev. Lett.* **118** (2017) 263202, URL: <https://doi.org/10.1103/PhysRevLett.118.263202> (cit. on p. 5).
- [39] V. Dzuba et al., *Strongly enhanced effects of Lorentz symmetry violation in entangled Yb^+ ions*, *Nat. Phys.* **12** (2016) 465, URL: <https://doi.org/10.1038/nphys3610> (cit. on p. 5).
- [40] U. Klingbeil, J. Kowalski, F. Träger, H. B. Wiegemann and G. zu Putlitz, *Atomic beam saturation and resonance fluorescence spectroscopy of a calcium intercombination line*, *Sov. J. Quantum Electron.* **8** (1978) 976, URL: <https://dx.doi.org/10.1070/QE1978v008n08ABEH010639> (cit. on pp. 5, 46).
- [41] D. Allan, *Statistics of atomic frequency standards*, *Proceedings of the IEEE* **54** (1966) 221, URL: <https://dx.doi.org/10.1109/PROC.1966.4634> (cit. on p. 5).
- [42] F. Riehle, *Frequency Standards: Basics and Applications*, Wiley-VCH, 2003, URL: <https://doi.org/10.1002/3527605991.fmatter> (cit. on p. 5).
- [43] W. J. Riley, *Handbook of Frequency Stability Analysis*, 2008, URL: https://tsapps.nist.gov/publication/get_pdf.cfm?pub_id=50505 (cit. on p. 5).
- [44] N. F. Ramsey, *A Molecular Beam Resonance Method with Separated Oscillating Fields*, *Phys. Rev.* **78** (1950) 695, URL: <https://dx.doi.org/10.1103/PhysRev.78.695> (cit. on p. 5).
- [45] N. F. Ramsey, *Experiments with separated oscillatory fields and hydrogen masers*, *Rev. Mod. Phys.* **62** (1990) 541, URL: <https://dx.doi.org/10.1103/RevModPhys.62.541> (cit. on p. 5).
- [46] P. Gill, *Optical frequency standards*, *Metrologia* **42** (2005) S125, URL: <https://dx.doi.org/10.1088/0026-1394/42/3/S13> (cit. on p. 6).
- [47] N. Hinkley et al., *An Atomic Clock with 10^{-18} Instability*, *Science* **341** (2013) 1215, URL: <https://doi.org/10.1126/science.1240420> (cit. on p. 6).
- [48] T. Prohaska et al., *Standard atomic weights of the elements 2021 (IUPAC Technical Report)*, *Pure and Applied Chemistry* **94** (2022) 573, URL: <https://doi.org/10.1515/pac-2019-0603> (cit. on p. 6).
- [49] M. Wang, W. Huang, F. Kondev, G. Audi and S. Naimi, *The AME 2020 atomic mass evaluation (II). Tables, graphs and references**, *Chin. Phys. C* **45** (2021) 030003, URL: <https://dx.doi.org/10.1088/1674-1137/abddaf> (cit. on p. 6).

-
- [50] F. Kondev, M. Wang, W. Huang, S. Naimi and G. Audi, *The NUBASE2020 evaluation of nuclear physics properties*, Chin. Phys. C **45** (2021) 030001, URL: <https://dx.doi.org/10.1088/1674-1137/abddae> (cit. on pp. 6, 37, 79).
- [51] J. Olson, *Ramsey-Bordé matter-wave interferometry with a thermal calcium beam for optical frequency stabilization 10^{-16}* , PhD thesis: University of Colorado, 2013 (cit. on pp. 7, 51).
- [52] J. Olson et al., *Ramsey-Borde Matter-Wave Interferometry for Laser Frequency Stabilization at 10^{-16} Frequency Instability and Below*, Phys. Rev. Lett. **123** (2019) 073202, URL: <https://doi.org/10.1103/PhysRevLett.123.073202> (cit. on p. 7).
- [53] A. V. Taichenachev et al., *Magnetic Field-Induced Spectroscopy of Forbidden Optical Transitions with Application to Lattice-Based Optical Atomic Clocks*, Phys. Rev. Lett. **96** (2006) 083001, URL: <https://dx.doi.org/10.1103/PhysRevLett.96.083001> (cit. on pp. 7, 9).
- [54] S. Origlia et al., *Towards an optical clock for space: Compact, high-performance optical lattice clock based on bosonic atoms*, Phys. Rev. A **98** (2018) 053443, URL: <https://dx.doi.org/10.1103/PhysRevA.98.053443> (cit. on pp. 7, 9).
- [55] D. Gullberg and U. Litzén, *Accurately Measured Wavelengths of Zn I and Zn II Lines of Astrophysical Interest*, Phys. Scr. **61** (2000) 652, URL: <https://dx.doi.org/10.1238/Physica.Regular.061a00652> (cit. on pp. 8, 29, 35, 70).
- [56] E. Staub, *Developing a High-Flux Atomic Beam Source for Experiments with Ultracold Strontium Quantum Gases*, MA thesis: Ludwig-Maximilians-Universität München, 2019 (cit. on pp. 7, 54).
- [57] F. C. Porter, *Corrosion resistance of zinc and zinc alloys*, CRC Press, 1994, ISBN: 0824792130 (cit. on p. 9).
- [58] A. F. Holleman and N. Wiberg, *Band 1 Grundlagen und Hauptgruppenelemente*, Berlin, Boston: De Gruyter, 2017, ISBN: 9783110495850, URL: <https://doi.org/10.1515/9783110495850> (cit. on p. 9).
- [59] A. F. Holleman and N. Wiberg, *Band 2 Nebengruppenelemente, Lanthanoide, Actinoide, Transactinoide*, Berlin, Boston: De Gruyter, 2017, ISBN: 9783110495904, URL: <https://doi.org/10.1515/9783110495904> (cit. on p. 9).
- [60] V. D. Ovsianikov et al., *Magic-wave-induced $^1S_0 - ^3P_0$ transition in even isotopes of alkaline-earth-metal-like atoms*, Phys. Rev. A **75** (2007) 020501, URL: <https://dx.doi.org/10.1103/PhysRevA.75.020501> (cit. on pp. 9–11).
- [61] S. Origlia, *A high-performance bosonic optical lattice clock*, PhD thesis: Heinrich-Heine-Universität Düsseldorf, 2018 (cit. on p. 9).

- [62] R. Santra, E. Arimondo, T. Ido, C. H. Greene and J. Ye, *High-Accuracy Optical Clock via Three-Level Coherence in Neutral Bosonic ^{88}Sr* , Phys. Rev. Lett. **94** (2005) 173002, URL: <https://dx.doi.org/10.1103/PhysRevLett.94.173002> (cit. on p. 10).
- [63] C. Lisdat, S. Dörscher, I. Nosske and U. Sterr, *Blackbody radiation shift in strontium lattice clocks revisited*, Phys. Rev. Res. **3** (2021) L042036, URL: <https://dx.doi.org/10.1103/PhysRevResearch.3.L042036> (cit. on pp. 10–12).
- [64] R. Schwarz, *A cryogenic strontium lattice clock*, PhD thesis: Gottfried Wilhelm Leibniz Universität Hannover, 2022 (cit. on pp. 10, 11).
- [65] T. Middelmann, S. Falke, C. Lisdat and U. Sterr, *High Accuracy Correction of Blackbody Radiation Shift in an Optical Lattice Clock*, Phys. Rev. Lett. **109** (2012) 263004, URL: <https://dx.doi.org/10.1103/PhysRevLett.109.263004> (cit. on p. 12).
- [66] R. Schwarz et al., *Long term measurement of the ^{87}Sr clock frequency at the limit of primary Cs clocks*, Phys. Rev. Res. **2** (2020) 033242, URL: <https://dx.doi.org/10.1103/PhysRevResearch.2.033242> (cit. on p. 12).
- [67] H. Hachisu et al., *Trapping of Neutral Mercury Atoms and Prospects for Optical Lattice Clocks*, Phys. Rev. Lett. **100** (2008) 053001, URL: <https://dx.doi.org/10.1103/PhysRevLett.100.053001> (cit. on p. 12).
- [68] D. Calonico et al., *High-accuracy coherent optical frequency transfer over a doubled 642-km fiber link*, Appl. Phys. B **117** (2014) 979, URL: <https://doi.org/10.1007/s00340-014-5917-8> (cit. on p. 12).
- [69] C. Clivati et al., *A coherent fiber link for very long baseline interferometry*, TUFFC **62** (2015) 1907, URL: <https://dx.doi.org/10.1109/TUFFC.2015.007221> (cit. on p. 12).
- [70] P. Delva et al., *Test of Special Relativity Using a Fiber Network of Optical Clocks*, Phys. Rev. Lett. **118** (2017) 221102, URL: <https://dx.doi.org/10.1103/PhysRevLett.118.221102> (cit. on p. 12).
- [71] Y. Hu, Y. Wang, J. Kuang and B. Wu, *A Clock Distribution and Synchronization Scheme Over Optical Links for Large-Scale Physics Experiments*, IEEE Transactions on Nuclear Science **68** (2021) 1351, URL: <https://dx.doi.org/10.1109/TNS.2021.3070589> (cit. on p. 12).
- [72] F. Riehle, *Optical clock networks*, Nature Photonics **11** (2017) 25 (cit. on p. 12).
- [73] M. Filzinger et al., *Improved Limits on the Coupling of Ultralight Bosonic Dark Matter to Photons from Optical Atomic Clock Comparisons*, Phys. Rev. Lett. **130** (2023) 253001, URL: <https://dx.doi.org/10.1103/PhysRevLett.130.253001> (cit. on p. 12).

-
- [74] S. M. F. Raupach, A. Koczwara and G. Grosche, *Brillouin amplification supports 1×10^{-20} uncertainty in optical frequency transfer over 1400 km of underground fiber*, Phys. Rev. A **92** (2015) 021801(R), URL: <https://dx.doi.org/10.1103/PhysRevA.92.021801> (cit. on p. 12).
- [75] A. Bercy et al., *Two-way optical frequency comparisons at 5×10^{-21} relative stability over 100-km telecommunication network fibers*, Phys. Rev. A **90** (2014) 061802(R), URL: <https://dx.doi.org/10.1103/PhysRevA.90.061802> (cit. on p. 12).
- [76] L.-S. Ma, P. Jungner, J. Ye and J. L. Hall, *Delivering the same optical frequency at two places: accurate cancellation of phase noise introduced by an optical fiber or other time-varying path*, Opt. Lett. **19** (1994) 1777, URL: <https://dx.doi.org/10.1364/OL.19.001777> (cit. on p. 12).
- [77] J. Jahns, *Photonik: Grundlagen, Komponenten und Systeme*, Oldenbourg Verlag München Wien, 2001, ISBN: 3486254251 (cit. on p. 12).
- [78] H. J. Metcalf and P. van der Straten, *Laser Cooling and Trapping*, Springer New York, 1999, ISBN: 9781461214700, URL: <https://doi.org/10.1007/978-1-4612-1470-0> (cit. on pp. 12, 52).
- [79] T. G. Tiecke, S. D. Gensemer, A. Ludewig and J. T. M. Walraven, *High-flux two-dimensional magneto-optical-trap source for cold lithium atoms*, Phys. Rev. A **80** (2009) 013409, URL: <https://dx.doi.org/10.1103/PhysRevA.80.013409> (cit. on p. 12).
- [80] J. C. Shaw, S. Hannig and D. J. McCarron, *Stable 2 W continuous-wave 261.5 nm laser for cooling and trapping aluminum monochloride*, Opt. Express **29** (2021) 37140, URL: <https://dx.doi.org/10.1364/OE.441741> (cit. on p. 13).
- [81] Z. Burkley, C. Rasor, S. Cooper, A. Brandt and D. Yost, *Yb fiber amplifier at 972.5 nm with frequency quadrupling to 243.1 nm*, Appl. Phys. B **123** (2017) 1 (cit. on p. 13).
- [82] Z. Burkley, A. D. Brandt, C. Rasor, S. F. Cooper and D. C. Yost, *Highly coherent, watt-level deep-UV radiation via a frequency-quadrupled Yb-fiber laser system*, Appl. Opt. **58** (2019) 1657 (cit. on p. 13).
- [83] Y. Kaneda et al., *Continuous-wave, single-frequency 229 nm laser source for laser cooling of cadmium atoms*, Opt. Lett. **41** (2016) 705, URL: <https://doi.org/10.1364/OL.41.000705> (cit. on p. 13).
- [84] S. Galtier, F. Nez, L. Julien and F. Biraben, *Ultraviolet continuous-wave laser source at 205nm for hydrogen spectroscopy*, Opt. Commun. **324** (2014) 34, URL: <https://doi.org/10.1016/j.optcom.2014.03.018> (cit. on p. 13).
- [85] K. Takachiho et al., *Ultraviolet laser-induced degradation of CsLiB₆O₁₀ and β - BaB₂O₄*, Opt. Mater. Express **4** (2014) 559, URL: <https://doi.org/10.1364/OME.4.000559> (cit. on p. 13).

- [86] M. Scheid et al., *750 mW continuous-wave solid-state deep ultraviolet laser source at the 253.7 nm transition in mercury*, *Opt. Lett.* **32** (2007) 955 (cit. on p. 13).
- [87] D. Kiefer, D. Preißler, T. Führer and T. Walther, *Non-degrading CW UV generation in β -barium borate at 257 nm using an elliptical focusing enhancement cavity*, *Laser Phys. Lett.* **16** (2019) 075403,
URL: <https://dx.doi.org/10.1088/1612-202X/ab232d> (cit. on p. 13).
- [88] D. Preißler, D. Kiefer, T. Führer and T. Walther, *Evolutionary algorithm-assisted design of a UV SHG cavity with elliptical focusing to avoid crystal degradation*, *Appl. Phys. B* **125** (2019) 1, URL: <https://doi.org/10.1007/s00340-019-7333-6> (cit. on p. 13).
- [89] T. Hänsch and B. Couillaud,
Laser frequency stabilization by polarization spectroscopy of a reflecting reference cavity, *Opt. Commun.* **35** (1980) 441,
URL: [https://doi.org/10.1016/0030-4018\(80\)90069-3](https://doi.org/10.1016/0030-4018(80)90069-3) (cit. on pp. 16, 79).
- [90] R. W. Boyd, *Nonlinear Optics*, Third Edition, Academic Press, 2008 v,
ISBN: 978-0-12-369470-6,
URL: <https://doi.org/10.1016/B978-0-12-369470-6.00020-4> (cit. on pp. 16, 18).
- [91] S. Kraemer, *Towards Laser Cooling of Beryllium Ions at the ALPHATRAP Experiment*, MA thesis: Ludwig-Maximilians-Universität München, 2017 (cit. on p. 17).
- [92] A. Egl, *High-Precision Laser Spectroscopy of the Fine Structure in $^{40}\text{Ar}^{13+}$ at ALPHATRAP*, PhD thesis: Ruperto-Carola-University of Heidelberg, 2020 (cit. on p. 17).
- [93] F. Hahne, *Investigation of a Novel Method for Sympathetic Laser Cooling of Highly Charged Ions in a Penning Trap*, MA thesis: Max-Planck-Institut für Kernphysik, Heidelberg, 2020 (cit. on p. 17).
- [94] L. Ricci et al., *A compact grating-stabilized diode laser system for atomic physics*, *Opt. Commun.* **117** (1995) 541,
URL: [https://doi.org/10.1016/0030-4018\(95\)00146-Y](https://doi.org/10.1016/0030-4018(95)00146-Y) (cit. on p. 17).
- [95] A. C. Wilson, J. C. Sharpe, C. R. McKenzie, P. J. Manson and D. M. Warrington,
Narrow-linewidth master-oscillator power amplifier based on a semiconductor tapered amplifier, *Appl. Opt.* **37** (1998) 4871, URL: <https://doi.org/10.1364/AO.37.004871> (cit. on p. 17).
- [96] D. A. Kleinman, A. Ashkin and G. D. Boyd,
Second-Harmonic Generation of Light by Focused Laser Beams, *Phys. Rev.* **145** (1966) 338,
URL: <https://dx.doi.org/10.1103/PhysRev.145.338> (cit. on p. 18).
- [97] R. Batchko, G. Miller, A. Alexandrovski, M. Fejer and R. Byer,
“Limitations of high-power visible wavelength periodically poled lithium niobate devices due to green-induced infrared absorption and thermal lensing”, *Technical Digest. Summaries of Papers Presented at the Conference on Lasers and Electro-Optics. Conference Edition. 1998 Technical Digest Series, Vol.6 (IEEE Cat. No.98CH36178)*, 1998 75,
URL: <https://dx.doi.org/10.1109/CLEO.1998.675885> (cit. on p. 19).

-
- [98] J. Sun and C.-q. Xu, *Green-induced infrared absorption in annealed proton-exchanged MgO:LiNbO₃ waveguides*, *J. Opt. Soc. Am. B* **31** (2014) 2779, URL: <https://doi.org/10.1364/JOSAB.31.002779> (cit. on p. 19).
- [99] W. H. King, *Isotope shifts in atomic spectra*, Springer Science & Business Media, 2013 (cit. on pp. 21, 23).
- [100] P. Campbell, I. Moore and M. Pearson, *Laser spectroscopy for nuclear structure physics*, *Progress in Particle and Nuclear Physics* **86** (2016) 127, URL: <https://doi.org/10.1016/j.pnpnp.2015.09.003> (cit. on p. 21).
- [101] J. C. Berengut, V. A. Dzuba and V. V. Flambaum, *Isotope-shift calculations for atoms with one valence electron*, *Phys. Rev. A* **68** (2003) 022502, URL: <https://dx.doi.org/10.1103/PhysRevA.68.022502> (cit. on p. 21).
- [102] C. W. P. Palmer, *Reformulation of the theory of the mass shift*, *J. Phys. B: At. Mol. Phys.* **20** (1987) 5987, URL: <https://dx.doi.org/10.1088/0022-3700/20/22/011> (cit. on p. 22).
- [103] I. Sobelman, *Introduction to the Theory of Atomic Spectra*, vol. 40, Pergamon, 1972, URL: <https://doi.org/10.1016/B978-0-08-016166-2.50006-8> (cit. on p. 22).
- [104] A. V. Viatkina, V. A. Yerokhin and A. Surzhykov, *Calculation of isotope shifts and King-plot nonlinearities in Ca⁺*, *Phys. Rev. A* **108** (2023) 022802, URL: <https://dx.doi.org/10.1103/PhysRevA.108.022802> (cit. on p. 22).
- [105] J. Billowes and P. Campbell, *High-resolution laser spectroscopy for the study of nuclear sizes and shapes*, *J. Phys. G* **21** (1995) 707, URL: <https://dx.doi.org/10.1088/0954-3899/21/6/003> (cit. on p. 23).
- [106] N. L. Figueroa et al., *Precision Determination of Isotope Shifts in Ytterbium and Implications for New Physics*, *Phys. Rev. Lett.* **128** (2022) 073001, URL: <https://doi.org/10.1103/PhysRevLett.128.073001> (cit. on pp. 23, 24, 70, 79).
- [107] W. H. King, *Comments on the Article "Peculiarities of the Isotope Shift in the Samarium Spectrum"*, *J. Opt. Soc. Am.* **53** (1963) 638, URL: <https://doi.org/10.1364/JOSA.53.000638> (cit. on pp. 23, 79).
- [108] K. Mikami, M. Tanaka and Y. Yamamoto, *Probing new intra-atomic force with isotope shifts*, *Eur. Phys. J. C* **77** (2017) 896, URL: <https://doi.org/10.1140/epjc/s10052-017-5467-4> (cit. on p. 24).
- [109] C. Delaunay, R. Ozeri, G. Perez and Y. Soreq, *Probing atomic Higgs-like forces at the precision frontier*, *Phys. Rev. D* **96** (2017) 093001, URL: <https://doi.org/10.1103/PhysRevD.96.093001> (cit. on pp. 24, 79).

- [110] C. Solaro et al., *Improved Isotope-Shift-Based Bounds on Bosons beyond the Standard Model through Measurements of the $^2D_{3/2} - ^2D_{5/2}$ Interval in Ca^+* , Phys. Rev. Lett. **125** (2020) 123003, URL: <https://doi.org/10.1103/PhysRevLett.125.123003> (cit. on pp. 24, 79).
- [111] N.-H. Rehbehn et al., *Sensitivity to new physics of isotope-shift studies using the coronal lines of highly charged calcium ions*, Phys. Rev. A **103** (2021) L040801, URL: <https://doi.org/10.1103/PhysRevA.103.L040801> (cit. on pp. 24, 79).
- [112] R. M. Potvliege, A. Nicolson, M. P. A. Jones and M. Spannowsky, *Deuterium spectroscopy for enhanced bounds on physics beyond the standard model*, Phys. Rev. A **108** (2023) 052825, URL: <https://doi.org/10.1103/PhysRevA.108.052825> (cit. on pp. 24, 79).
- [113] P. Campbell, J. Billowes and I. S. Grant, *The specific mass shift of the zinc atomic ground state*, J. Phys. B: At. Mol. Opt. Phys. **30** (1997) 2351, URL: <https://dx.doi.org/10.1088/0953-4075/30/10/010> (cit. on pp. 25, 30, 35, 36, 70).
- [114] R. C. Brown et al., *Quantum interference and light polarization effects in unresolvable atomic lines: Application to a precise measurement of the $^{6,7}Li D_2$ lines*, Phys. Rev. A **87** (2013) 032504, URL: <https://doi.org/10.1103/PhysRevA.87.032504> (cit. on pp. 25, 70).
- [115] T. Mukaiyama, H. Katori, T. Ido, Y. Li and M. Kuwata-Gonokami, *Recoil-Limited Laser Cooling of ^{87}Sr Atoms near the Fermi Temperature*, Phys. Rev. Lett. **90** (2003) 113002, URL: <https://doi.org/10.1103/PhysRevLett.90.113002> (cit. on pp. 29, 35).
- [116] M. M. Boyd, *High Precision Spectroscopy of Strontium in an Optical Lattice: Towards a New Standard for Frequency and Time*, PhD thesis: University of Colorado, 2002 (cit. on pp. 29, 35, 57).
- [117] M. J. Doppelbauer, *The AlF Molecule as a Candidate for Laser Cooling and Trapping*, PhD thesis: Radboud Universiteit Nijmegen, 2022 (cit. on pp. 29, 32, 33).
- [118] S. L. T. Hofsäss, *Laser Cooling of Atoms and Molecules in the Deep Ultraviolet*, PhD thesis: Radboud Universiteit Nijmegen, 2023 (cit. on pp. 29, 31, 32).
- [119] S. Truppe et al., *A buffer gas beam source for short, intense and slow molecular pulses*, J. Mod. Opt. **65** (2017) 648, URL: <https://doi.org/10.1080/09500340.2017.1384516> (cit. on p. 29).
- [120] B. Ohayon et al., *Isotope shifts in cadmium as a sensitive probe for physics beyond the standard model*, New J. Phys. **24** (2022) 123040, URL: <https://dx.doi.org/10.1088/1367-2630/acacbb> (cit. on pp. 29, 70).
- [121] S. Hofsäss et al., *High-resolution isotope-shift spectroscopy of Cd I*, Phys. Rev. Res. **5** (2023) 013043, URL: <https://doi.org/10.1103/PhysRevResearch.5.013043> (cit. on pp. 29, 31, 70).

-
- [122] X. F. Yang et al., *Isomer Shift and Magnetic Moment of the Long-Lived $1/2^+$ Isomer in $^{79}_{30}\text{Zn}_{49}$: Signature of Shape Coexistence near ^{78}Ni* , Phys. Rev. Lett. **116** (2016) 182502, URL: <https://doi.org/10.1103/PhysRevLett.116.182502> (cit. on p. 30).
- [123] C. Wraith et al., *Evolution of nuclear structure in neutron-rich odd-Zn isotopes and isomers*, Phys. Lett. B **771** (2017) 385, URL: <https://doi.org/10.1016/j.physletb.2017.05.085> (cit. on pp. 30, 70).
- [124] L. Xie et al., *Nuclear charge radii of $^{62-80}\text{Zn}$ and their dependence on cross-shell proton excitations*, Phys. Lett. B **797** (2019) 134805, URL: <https://doi.org/10.1016/j.physletb.2019.134805> (cit. on pp. 30, 70).
- [125] J. F. Barry, E. S. Shuman and D. DeMille, *A bright, slow cryogenic molecular beam source for free radicals*, Phys. Chem. Chem. Phys. **13** (2011) 18936, URL: <http://dx.doi.org/10.1039/C1CP20335E> (cit. on p. 30).
- [126] N. R. Hutzler, H.-I. Lu and J. M. Doyle, *The Buffer Gas Beam: An Intense, Cold, and Slow Source for Atoms and Molecules*, Chem. Rev. **112** (2012) 4803, URL: <https://doi.org/10.1021/cr200362u> (cit. on p. 30).
- [127] S. E. Maxwell et al., *High-Flux Beam Source for Cold, Slow Atoms or Molecules*, Phys. Rev. Lett. **95** (2005) 173201, URL: <https://doi.org/10.1103/PhysRevLett.95.173201> (cit. on p. 30).
- [128] E. D. Black, *An introduction to Pound–Drever–Hall laser frequency stabilization*, Am. J. Phys. **69** (2001) 79, URL: <https://doi.org/10.1119/1.1286663> (cit. on pp. 31, 38, 47).
- [129] J. Kowalski and F. Träger, *Hyperfine structure of the $4s4p^1P_1$ -state of ^{67}Zn by level crossing spectroscopy*, Z. Phys. A **278** (1976) 1, URL: <https://doi.org/10.1007/BF01547334> (cit. on pp. 35, 70).
- [130] P. Doidge, *A compendium and critical review of neutral atom resonance line oscillator strengths for atomic absorption analysis*, Spectrochim. Acta Part B **50** (1995) 209, URL: [https://doi.org/10.1016/0584-8547\(94\)01199-B](https://doi.org/10.1016/0584-8547(94)01199-B) (cit. on pp. 35, 70).
- [131] E. J. Salumbides et al., *High-precision frequency measurement of the 423-nm Ca I line*, Phys. Rev. A **83** (2011) 012502, URL: <https://doi.org/10.1103/PhysRevA.83.012502> (cit. on pp. 37, 38, 42, 79).
- [132] W. Nörtershäuser, N. Trautmann, K. Wendt and B. Bushaw, *Isotope shifts and hyperfine structure in the $4s^2\ ^1S_0 \rightarrow 4s4p\ ^1P_1 \rightarrow 4s4d\ ^1D_2$ transitions of stable calcium isotopes and calcium-41*, Spectrochim. Acta Part B **53** (1998) 709, URL: [https://doi.org/10.1016/S0584-8547\(98\)00108-6](https://doi.org/10.1016/S0584-8547(98)00108-6) (cit. on pp. 38, 42, 79).
- [133] A. Andl et al., *Isotope shifts and hyperfine structure of the $4s^2\ ^1S_0 - 4s4p\ ^1P_1$ transition in calcium isotopes*, Phys. Rev. C **26** (1982) 2194, URL: <https://doi.org/10.1103/PhysRevC.26.2194> (cit. on pp. 38, 79).

- [134] R. Grimm and J. Mlynek, *Observation of Light-Pressure-Induced Dispersion in Yb Vapor*, Phys. Rev. Lett. **61** (1988) 2308,
URL: <https://doi.org/10.1103/PhysRevLett.61.2308> (cit. on p. 41).
- [135] R. Grimm and J. Mlynek,
Light-pressure-induced line-shape asymmetry of the saturation dip in an atomic gas,
Phys. Rev. Lett. **63** (1989) 232,
URL: <https://dx.doi.org/10.1103/PhysRevLett.63.232> (cit. on pp. 41, 79).
- [136] R. Grimm and J. Mlynek, *The effect of resonant light pressure in saturation spectroscopy*,
Appl. Phys. B **49** (1989) 179, URL: <https://doi.org/10.1007/BF00714634>
(cit. on p. 41).
- [137] A. Kramida, Y. Ralchenko, J. Reader and NIST ASD Team,
NIST Atomic Spectra Database (ver. 5.11), 2023 (cit. on pp. 41, 57, 79).
- [138] J. L. Hall, C. J. Bordé and K. Uehara,
Direct Optical Resolution of the Recoil Effect Using Saturated Absorption Spectroscopy,
Phys. Rev. Lett. **37** (1976) 1339,
URL: <https://link.aps.org/doi/10.1103/PhysRevLett.37.1339>
(cit. on pp. 41, 79).
- [139] W. Demtröder, *Laser Spectroscopy 1: Basic Principles*, 5th Edition, Springer Nature, 2014,
ISBN: 9783642538582,
URL: <https://link.springer.com/book/10.1007/978-3-642-53859-9>
(cit. on p. 41).
- [140] W. Demtröder, *Laser Spectroscopy 2: Experimental Techniques*,
Springer Berlin Heidelberg, 2015, ISBN: 9783662446416 (cit. on pp. 41, 45, 46, 79).
- [141] W. R. Hindmarsh and J. M. Farr, *Collision broadening of spectral lines by neutral atoms*,
Prog. Quantum Electron. **2** (1973) 141,
URL: [https://doi.org/10.1016/0079-6727\(73\)90005-0](https://doi.org/10.1016/0079-6727(73)90005-0) (cit. on pp. 41, 79).
- [142] J. M. Farr and W. R. Hindmarsh,
Collision broadening in the strontium resonance line, lambda 4607 AA,
J. Phys. B: Atom. Mol. Opt. Phys. **4** (1971) 568,
URL: <https://dx.doi.org/10.1088/0022-3700/4/4/019> (cit. on pp. 41, 79).
- [143] G. Smith, *Collision broadening and shift in the resonance line of calcium*,
J. Phys. B: Atom. Mol. Phys. **5** (1972) 2310,
URL: <https://dx.doi.org/10.1088/0022-3700/5/12/024> (cit. on pp. 41, 79).
- [144] R. Ciurylo, J. Szudy and R. S. Trawifiski, *NON-ADIABATIC APPROACH TO THE ASYMMETRY OF PRESSURE BROADENED SPECTRAL LINES*,
J. Quant. Spcctrosc. Radiat. Transfer **57** (1997) 551,
URL: [https://doi.org/10.1016/S0022-4073\(96\)00139-2](https://doi.org/10.1016/S0022-4073(96)00139-2) (cit. on pp. 41, 79).
- [145] R. E. Walkup, A. Spielfiedel and D. E. Pritchard,
Observation of Non-Lorentzian Spectral Line Shapes in Na-Noble-Gas Systems,
Phys. Rev. Lett. **45** (1980) 986,
URL: <https://dx.doi.org/10.1103/PhysRevLett.45.986> (cit. on pp. 41, 79).

-
- [146] R. Walkup, B. Stewart and D. E. Pritchard, *Collisional line broadening due to van der Waals potentials*, Phys. Rev. A **29** (1984) 169, URL: <https://dx.doi.org/10.1103/PhysRevA.29.169> (cit. on pp. 41, 79).
- [147] J. F. Kielkopf, *On the precise evaluation of the complete semiclassical spectral line shape for pressure-broadened atomic spectral lines*, J. Phys. B: Atom. Mol. Phys. **9** (1976) 1601, URL: <https://dx.doi.org/10.1088/0022-3700/9/9/023> (cit. on p. 41).
- [148] M. V. Romalis, E. Miron and G. D. Cates, *Pressure broadening of Rb D_1 and D_2 lines by ^3He , ^4He , N_2 , and Xe : Line cores and near wings*, Phys. Rev. A **56** (1997) 4569, URL: <https://doi.org/10.1103/PhysRevA.56.4569> (cit. on p. 41).
- [149] S. E. Park, H. S. Lee, T. Y. Kwon and H. Cho, *Dispersion-like signals in velocity-selective saturated-absorption spectroscopy*, Opt. Commun. **192** (2001) 49, URL: [https://doi.org/10.1016/S0030-4018\(01\)01155-5](https://doi.org/10.1016/S0030-4018(01)01155-5) (cit. on pp. 42, 79).
- [150] G. Peach, "Collisional Broadening of Spectral Lines", *Springer Handbook of Atomic, Molecular, and Optical Physics*, ed. by G. Drake, Springer Science and Business Media, 2007, URL: <https://doi.org/10.1007/978-0-387-26308-3> (cit. on p. 45).
- [151] R. Saxena and G. Agarwal, *Resolution beyond natural linewidth via fluorescence in modulated beams*, Opt. Commun. **40** (1982) 357, URL: [https://doi.org/10.1016/0030-4018\(82\)90362-5](https://doi.org/10.1016/0030-4018(82)90362-5) (cit. on p. 46).
- [152] T. Legero, T. Kessler and U. Sterr, *Tuning the thermal expansion properties of optical reference cavities with fused silica mirrors*, J. Opt. Soc. Am. B **27** (2010) 914, URL: <https://doi.org/10.1364/JOSAB.27.000914> (cit. on p. 46).
- [153] Q.-F. Chen et al., *A compact, robust, and transportable ultra-stable laser with a fractional frequency instability of 1×10^{-15}* , Rev. Sci. Instrum. **85** (2014) 113107, URL: <https://doi.org/10.1063/1.4898334> (cit. on p. 46).
- [154] T. Nazarova, F. Riehle and U. Sterr, *Vibration-insensitive reference cavity for an ultra-narrow-linewidth laser*, Appl. Phys. B (2006) 531, URL: <https://doi.org/10.1007/s00340-006-2225-y> (cit. on p. 46).
- [155] D. R. Leibbrandt et al., *Spherical reference cavities for frequency stabilization of lasers in non-laboratory environments*, Opt. Express **19** (2011) 3471, URL: <https://doi.org/10.1364/OE.19.003471> (cit. on p. 46).
- [156] S. A. Webster, M. Oxborrow and P. Gill, *Vibration insensitive optical cavity*, Phys. Rev. A **75** (2007) 011801, URL: <https://doi.org/10.1103/PhysRevA.75.011801> (cit. on pp. 46, 47).
- [157] S. A. Webster, M. Oxborrow, S. Pugla, J. Millo and P. Gill, *Thermal-noise-limited optical cavity*, Phys. Rev. A **77** (2008) 033847, URL: <https://doi.org/10.1103/PhysRevA.77.033847> (cit. on p. 46).

- [158] S. Webster and P. Gill, *Force-insensitive optical cavity*, Opt. Lett. **36** (2011) 3572, URL: <https://doi.org/10.1364/OL.36.003572> (cit. on p. 46).
- [159] S. Häfner, *Ultra-stabile Lasersysteme für Weltraum- und Bodenanwendungen*, PhD thesis: Gottfried Wilhelm Leibniz Universität Hannover, 2015 (cit. on p. 46).
- [160] G. Berden, R. Peeters and G. Meijer, *Cavity ring-down spectroscopy: Experimental schemes and applications*, Int. Rev. Phys. Chem. **19** (2000) 565, URL: <https://doi.org/10.1080/014423500750040627> (cit. on p. 46).
- [161] S. A. ep Pyka, *A Long Optical Cavity For Sub-Hertz Laser Spectroscopy*, PhD thesis: Gottfried Wilhelm Leibniz Universität Hannover, 2014 (cit. on p. 47).
- [162] N. Ramsey, *Molecular Beams*, International Series of Monographs on Physics, OUP Oxford, 1956, ISBN: 9780198520214 (cit. on p. 51).
- [163] H. C. W. Beijerinck and N. F. Verster, *Velocity distribution and angular distribution of molecular beams from multichannel arrays*, J. Appl. Phys. **46** (1975) 2083, URL: <https://doi.org/10.1063/1.321845> (cit. on p. 51).
- [164] T. J. Harrison, *Measuring the Gap and Investigating Non-equilibrium in the BEC-BCS Crossover*, PhD thesis: Rheinische Friedrich-Wilhelms-Universität Bonn, 2017 (cit. on p. 54).
- [165] M. Ortner and L. G. C. Bandeira, *Magpylib: A free Python package for magnetic field computation*, SoftwareX **11** (2020) 100466, URL: <https://doi.org/10.1016/j.softx.2020.100466> (cit. on p. 54).
- [166] S. Eckel, D. S. Barker, E. B. Norrgard and J. Scherschligt, *PyLCP: A Python package for computing laser cooling physics*, Comput. Phys. Commun. **270** (2022) 108166, URL: <https://doi.org/10.1016/j.cpc.2021.108166> (cit. on p. 55).
- [167] I. Nosske et al., *Two-dimensional magneto-optical trap as a source for cold strontium atoms*, Phys. Rev. A **96** (2017) 053415, URL: <https://dx.doi.org/10.1103/PhysRevA.96.053415> (cit. on p. 55).
- [168] R. Grimm, M. Weidemüller and Y. B. Ovchinnikov, “Optical Dipole Traps for Neutral Atoms”, ed. by B. Bederson and H. Walther, vol. 42, Adv. At. Mol. Opt. Phys. Academic Press, 2000 95, URL: [https://doi.org/10.1016/S1049-250X\(08\)60186-X](https://doi.org/10.1016/S1049-250X(08)60186-X) (cit. on p. 57).
- [169] A. Ye and G. Wang, *Dipole polarizabilities of $ns^2\ ^1S_0$ and $nsnp\ ^3P_0$ states and relevant magic wavelengths of group-II B atoms*, Phys. Rev. A **78** (2008) 014502, URL: <https://doi.org/10.1103/PhysRevA.78.014502> (cit. on p. 57).
- [170] A. Derevianko and H. Katori, *Colloquium: Physics of optical lattice clocks*, Rev. Mod. Phys. **83** (2011) 331, URL: <https://doi.org/10.1103/RevModPhys.83.331> (cit. on p. 57).

-
- [171] R. Zerne, L. Caiyan, J. Zhankui, J. Larsson and S. Svanberg, *Determination of radiative lifetimes in the $3d^{10}4snp^1P_1$ sequence of neutral zinc by time-resolved VUV laser spectroscopy*, *Z. Phys. D* **32** (1994) 187, URL: <https://doi.org/10.1007/BF01437146> (cit. on p. 57).
- [172] H. Kerkhoff, M. Schmidt and P. Zimmermann, *Lifetimes and oscillator strengths in the triplet system of ZnI*, *Z. Phys. A* **298** (1980) 249, URL: <https://doi.org/10.1007/BF01425154> (cit. on p. 58).
- [173] K. B. Blagoev et al., *Radiative Lifetimes of Zn I, II Excited States*, *Phys. Scr.* **69** (2004) 433, URL: <https://dx.doi.org/10.1238/Physica.Regular.069a00433> (cit. on p. 58).
- [174] C. Froese Fischer and O. Zatsarinny, *$4p^2$ resonances in photoionization from $4s4p$ levels in neutral zinc*, *Theor. Chem. Acc.* **118** (2007) 623, URL: <https://doi.org/10.1007/s00214-007-0348-9> (cit. on p. 58).
- [175] M. G. Tarallo et al., *Test of Einstein Equivalence Principle for 0-Spin and Half-Integer-Spin Atoms: Search for Spin-Gravity Coupling Effects*, *Phys. Rev. Lett.* **113** (2014) 023005, URL: <https://doi.org/10.1103/PhysRevLett.113.023005> (cit. on p. 70).
- [176] A. J. Daley, M. M. Boyd, J. Ye and P. Zoller, *Quantum Computing with Alkaline-Earth-Metal Atoms*, *Phys. Rev. Lett.* **101** (2008) 170504, URL: <https://doi.org/10.1103/PhysRevLett.101.170504> (cit. on p. 70).
- [177] A. V. Gorshkov et al., *Alkaline-Earth-Metal Atoms as Few-Qubit Quantum Registers*, *Phys. Rev. Lett.* **102** (2009) 110503, URL: <https://doi.org/10.1103/PhysRevLett.102.110503> (cit. on p. 70).
- [178] M. Saffman, *Quantum computing with atomic qubits and Rydberg interactions: progress and challenges*, *J. Phys. B: At. Mol. Phys.* **49** (2016) 202001, URL: <https://dx.doi.org/10.1088/0953-4075/49/20/202001> (cit. on p. 70).
- [179] C. E. Simien et al., *Using Absorption Imaging to Study Ion Dynamics in an Ultracold Neutral Plasma*, *Phys. Rev. Lett.* **92** (2004) 143001, URL: <https://doi.org/10.1103/PhysRevLett.92.143001> (cit. on p. 70).
- [180] A. Browaeys and T. Lahaye, *Many-body physics with individually controlled Rydberg atoms*, *Nat. Phys.* **16** (2020) 132, URL: <https://doi.org/10.1038/s41567-019-0733-z> (cit. on p. 70).
- [181] M. Witkowski et al., *Absolute frequency and isotope shift measurements of mercury $^1S_0 - ^3P_1$ transition*, *Opt. Express* **27** (2019) 11069, URL: <https://doi.org/10.1364/OE.27.011069> (cit. on p. 70).
- [182] K. Ono et al., *Observation of Nonlinearity of Generalized King Plot in the Search for New Boson*, *Phys. Rev. X* **12** (2022) 021033, URL: <https://doi.org/10.1103/PhysRevX.12.021033> (cit. on pp. 70, 79).

- [183] L. D. Sarlo, M. Favier, R. Tyumenev and S. Bize, *A mercury optical lattice clock at LNE-SYRTE*, J. Phys.: Conf. Ser. **723** (2016) 012017, URL: <https://dx.doi.org/10.1088/1742-6596/723/1/012017> (cit. on p. 70).
- [184] R. Tyumenev et al., *Comparing a mercury optical lattice clock with microwave and optical frequency standards*, New J. Phys. **18** (2016) 113002, URL: <https://dx.doi.org/10.1088/1367-2630/18/11/113002> (cit. on p. 70).
- [185] X. Yang, T. Cocolios and S. Geldhof, *Probing the magicity and shell evolution in the vicinity of $N = 50$ with high-resolution laser spectroscopy of $^{81,82}\text{Zn}$ isotopes*, tech. rep., (unpublished): CERN, 2020, URL: <https://cds.cern.ch/record/2731961> (cit. on p. 70).
- [186] Y. Liu et al., *Collinear resonance ionization spectroscopy of stable 64, 66, 67, 68, 70 Zn isotopes*, tech. rep., ISOLDE workshop and users meeting, Contribution ID: 21 (unpublished): CERN, 2022 (cit. on p. 70).
- [187] W. Rasmussen, R. Schieder and H. Walther, *Atomic fluorescence under monochromatic excitation: A level crossing experiment on the $6s6p\ ^1P_1$ level of Ba I*, Opt. Commun. **12** (1974) 315, URL: [https://doi.org/10.1016/0030-4018\(74\)90023-6](https://doi.org/10.1016/0030-4018(74)90023-6) (cit. on p. 70).
- [188] P. E. G. Baird et al., *Optical isotope shifts and hyperfine structure in λ 553.5 nm of barium*, Proc. R. Soc. London A **365** (1979) 567, URL: <http://doi.org/10.1098/rspa.1979.0035> (cit. on p. 70).
- [189] W. Hanle, *Über den Zeemaneffekt bei der Resonanzfluoreszenz*, Naturwiss. **11** (1923) 690, URL: <https://doi.org/10.1007/BF01551296> (cit. on p. 70).
- [190] A. C. G. Mitchell and M. W. Zemansky, “Resonance Radiation and Excited Atoms”, London: Cambridge University Press, 1961, chap. V (cit. on p. 70).
- [191] K. J. R. Rosman and P. D. P. Taylor, *Isotopic compositions of the elements 1997 (Technical Report)*, Pure and Appl. Chem. **70** (1998) 217, URL: <https://doi.org/10.1351/pac199870010217> (cit. on p. 70).
- [192] B. K. Sahoo and B. Ohayon, *All-optical differential radii in zinc*, Phys. Rev. Res. **5** (2023) 043142, URL: <https://doi.org/10.1103/PhysRevResearch.5.043142> (cit. on p. 70).
- [193] P. Plattner et al., *Nuclear Charge Radius of ^{26m}Al and its Implication for V_{ud} in the Quark Mixing Matrix*, Phys. Rev. Lett. **131** (2023) 222502, URL: <https://doi.org/10.1103/PhysRevLett.131.222502> (cit. on p. 70).
- [194] P. Micke et al., *Coherent laser spectroscopy of highly charged ions using quantum logic*, Nature **578** (2020) 60, URL: <https://doi.org/10.1038/s41586-020-1959-8> (cit. on p. 79).

-
- [195] T. T. Chang, B. B. Awazi, J. C. Berengut, E. Fuchs and S. C. Doret, *Systematic-free limit on new light scalar bosons via isotope shift spectroscopy in Ca+*, 2024, arXiv: 2311.17337 [physics.atom-ph] (cit. on p. 79).
- [196] M. Door et al., *Search for new bosons with ytterbium isotope shifts*, 2024, arXiv: 2403.07792 [physics.atom-ph], URL: <https://arxiv.org/abs/2403.07792> (cit. on p. 79).
- [197] H. Nakada, *Irregularities in nuclear radii at magic numbers*, Phys. Rev. C **100** (2019) 044310, URL: <https://doi.org/10.1103/PhysRevC.100.044310> (cit. on p. 79).
- [198] A. Mortensen et al., *Isotope shifts of $4s^2\ ^1S_0 \rightarrow 4s5p\ ^1P_1$ transition and hyperfine splitting of the $4s5p\ ^1P_1$ state in calcium*, Phys. Rev. A **69** (2004) 042502, URL: <https://doi.org/10.1103/PhysRevA.69.042502> (cit. on p. 79).
- [199] C. Shi et al., *Unexpectedly large difference of the electron density at the nucleus in the $4p^2\ ^2P_{1/2,3/2}$ fine-structure doublet of Ca⁺*, Appl. Phys. B **123** (2017) 2, URL: <https://doi.org/10.1007/s00340-016-6572-z> (cit. on p. 79).
- [200] P. Müller, K. König, P. Ingram, J. Krämer and W. Nörtershäuser, *Collinear laser spectroscopy of Ca⁺: Solving the field-shift puzzle of the $4s^2S_{1/2} \rightarrow 4p^2P_{1/2,3/2}$ transitions*, Phys. Rev. Res. **2** (2020) 043351, URL: <https://doi.org/10.1103/PhysRevResearch.2.043351> (cit. on p. 79).
- [201] F. Gebert et al., *Precision Isotope Shift Measurements in Calcium Ions Using Quantum Logic Detection Schemes*, Phys. Rev. Lett. **115** (2015) 053003, URL: <https://doi.org/10.1103/PhysRevLett.115.053003> (cit. on p. 79).
- [202] A. Kramida, *Isotope shifts in neutral and singly-ionized calcium*, At. Data Nucl. Data Tables **133-134** (2020) 101322, URL: <https://doi.org/10.1016/j.adt.2019.101322> (cit. on p. 79).
- [203] C. B. Alcock, V. P. Itkin and M. K. Horrigan, *Vapour Pressure Equations for the Metallic Elements: 298–2500K*, Can. Metall. Q. **23** (1984) 309, URL: <https://doi.org/10.1179/cmqr.1984.23.3.309> (cit. on p. 79).
- [204] J. Tenenbaum et al., *Velocity changing collisions in saturation absorption of U*, J. Phys. B: Atom. Mol. Phys. **16** (1983) 4543, URL: <https://dx.doi.org/10.1088/0022-3700/16/24/011> (cit. on p. 79).
- [205] N. H. Ngo, D. Lisak, H. Tran and J.-M. Hartmann, *An isolated line-shape model to go beyond the Voigt profile in spectroscopic databases and radiative transfer codes*, J. Quant. Spectrosc. Radiat. Transfer **129** (2013) 89, URL: <https://doi.org/10.1016/j.jqsrt.2013.05.034> (cit. on p. 79).
- [206] H. Tran, N. H. Ngo and J.-M. Hartmann, *Efficient computation of some speed-dependent isolated line profiles*, J. Quant. Spectrosc. Radiat. Transfer **129** (2013) 199, URL: <https://doi.org/10.1016/j.jqsrt.2013.06.015> (cit. on p. 79).

- [207] H. Tran, N. Ngo and J.-M. Hartmann, *Erratum to “Efficient computation of some speed-dependent isolated line profiles”* [*J. Quant. Spectrosc. Radiat. Transfer* **129** (2013) 199–203], *J. Quant. Spectrosc. Radiat. Transfer* **134** (2014) 104, URL: <https://doi.org/10.1016/j.jqsrt.2013.10.015> (cit. on p. 79).
- [208] Wang Meng et al., *The AME2016 atomic mass evaluation (II). Tables, graphs and references*, *Chin. Phys. C* **41** (2017) 030003, URL: <https://dx.doi.org/10.1088/1674-1137/41/3/030003> (cit. on p. 79).
- [209] G. C. Bjorklund and E. A. Whittaker, *High Sensitivity Frequency Modulation Spectroscopy and the Path to Single Molecule Detection*, *J. Phys. Chem. A* **125** (2021) 8519, URL: <https://doi.org/10.1021/acs.jpca.1c05752> (cit. on p. 79).
- [210] A. Banerjee and V. Natarajan, *Saturated-absorption spectroscopy: eliminating crossover resonances by use of copropagating beams*, *Opt. Lett.* **28** (2003) 1912, URL: <https://doi.org/10.1364/OL.28.001912> (cit. on p. 79).

List of Figures

2.1	Level scheme for Zn. The transition wavelengths and linewidths in natural frequencies are given for the most relevant transitions [10, 34, 55]. Other transitions are used for calculating the magic wavelength (see Abschnitt 6.3).	8
2.2	Vapor pressure curve for Zn. The underlying formula is given in Ref. [10].	8
2.3	Different methods for populating the 3P_0 state in bosonic Zn isotopes. a) An external magnetic field B_{ext} is applied to couple the 3P_1 and 3P_0 states with a magnetic dipole interaction. Then the clock state might be directly excited. b) A STIRAP scheme is applied. If the Δ_p is in the vicinity of Δ_d , the population might be transferred into the 3P_0 state. c) A small portion of clock lattice light at the “magic” wavelength λ_m can be circularly polarized. This couples the 3P_1 and 3P_0 states thus allowing direct excitation of the 3P_0 state.	11
2.4	The figure demonstrates a typical example of transmission losses in optical fibers. Specifically, this loss spectrum corresponds to a fiber with low OH-concentration. The specific spectral shape of each fiber varies, as the OH-concentration might be different and impurities add further absorption peaks. The fourth and fifth harmonic of the clock transition at 310 nm falls into the regions of minimal absorption and are marked. The figure is adapted from Ref. [24].	13
2.5	Sketch of the 214 nm laser. The beam profiles have been recorded with a USB camera. The circular interference patterns are created by dust on optical attenuators that are mounted to the camera. f_h and f_v denote focal lengths of cylindrical lenses oriented horizontally or vertically, respectively. The laser’s operability is confirmed by measuring Doppler broadened absorption in a Zn vapor cell. The measurement has been conducted by Marc Vöhringer and the illustration of the beam profiles before and after the periscope is adapted from Ref. [31].	14
2.6	The figure shows a photography of the pump laser beam impinging on the second steering mirror. At this stage, the power degradation has progressed to the point where the beam hits the top of the mirror. During the system’s operation, the spot continued to rise even further. During the writing process of this thesis, the laser was sent for repair.	16
2.7	(a): Setup and beam profile of the 310 nm laser. (b): A Doppler broadened absorption profile of the 3P_1 intercombination line at 308 nm acquired by a linear spectroscopy in a Zn vapor cell. A wavemeter (High Finesse WS-8-5) served as frequency reference. The measurement data has been taken by Maya Büki. Both figures are adapted from Ref. [33].	18

4.1	(a): Sketch of the buffer gas cooled beam source. The Zn atomic beam is generated by an ablation laser pulse in the buffer gas cell and depicted in light cyan, while the laser beam is shown in red. The laser induced fluorescence (LiF) is collected with photomultipliers (PMT) in two orthogonal directions to the laser beam. (b): LiF collection apparatus including the lens systems. (c): θ denotes the angle between detection direction and laser polarization, while θ_C denotes the solid angle of LiF collection. The figures are adapted from Refs. [34, 117, 118] and Sid C. Wright.	32
4.2	Laser frequency stabilization setup. A frequency-doubled, voltage-controlled oscillator (VCO) generates the carrier shift frequency for scanning the laser with respect to the ULE cavity. A direct digital synthesis (DDS) generator provides the locking sidebands for the Pound-Drever-Hall lock. An identical generator, phase-locked to the latter one, is used for demodulation of the photo detector (PD) signal. The signal is filtered by a servo-controller and split into a fast and a slow feedback circuit, which is applied to the respective inputs of the laser controller.	33
4.3	Fluorescence measurements with the wavemeter as frequency reference. In the top row, the trace for vertical polarization is shown, while the trace for horizontal polarization is shown in the bottom row. The figure illustrates the spatial emission pattern for fermionic and bosonic isotopes. This figure is adapted from Ref. [34].	34
4.4	King plot analysis with the data reported on the intercombination line in Ref. [113]. The figure is adapted from Ref. [34].	36
5.1	(a): Frequency-doubled laser system. The length of the SHG cavity is stabilized to the laser by a Hänsch-Couillaud locking scheme. (b): Setup of the Pound-Drever-Hall lock for frequency stabilization of the laser to a ULE cavity. (c): Setup for saturated absorption spectroscopy. The figure is adapted from Ref. [35].	39
5.2	Single scans of all measured isotopes including the line fit and residuals. The figure is adapted from Ref. [35].	40
5.3	King plot with measured isotope shifts from this measurement and from Ref. [21]. The errors from Ref. [21] are too small to be visible as errorbars. The figure is adapted from Ref. [35].	43
6.1	(a): Dimensions of the ULE cavity spacer. The mirror dimensions are $\varnothing 25.4 \text{ mm} \times 6.35 \text{ mm}$. All dimensions are given in mm. (b): Simulated mirror center displacement for an automatically optimized mesh by the simulation software. Within the x and y ranges, a point grid with a spacing of 0.2 mm was simulated and linearly interpolated. (c): Definition of the reference frame for x and y . The origin of the coordinate system is located at the outermost corner of the spacer, where the x - and y -axes are intersecting. The little square shows the area shown in (b). Only a quarter of the cavity is shown in top view.	48

6.2	(a): Optimized cavity support structure withing two copper heat shields and a stainless steel vacuum system. The cavity lies on a stainless steel support structure, which is connected with a self-designed floating bearing to a glass plate. (b): Photograph of the guide rails for the glass spheres between outer and inner heat shield. While the bottom left support point constrains translational movement, the bottom right constrains rotations while leaving space for thermal expansion. The support point on the top does not constrain any movement. Due to the high surface quality, the copper is highly reflective. (c): Between support structure and glass plate, two Viton spheres are placed, which are marked in white. A screw keeps the two spheres under light pressure such that the support structure is weakly allowed to move. At the other support points, the structure lies on glass spheres, which are allowed to freely move.	49
6.3	Fluorescence spectroscopy setup.	50
6.4	Measurement chamber for atom excitation and fluorescence collection.	52
6.5	(a): CAD drawing of the entire MOT setup including the MOT coils, their watercooling system and the vacuum pumps. (b): Vacuum system used in the MOT setup. The Zn source and the dump are explicitly shown in Abb. 6.6.	53
6.6	(a): CAD drawing of the Zn source. (b): CAD drawing of the Zn dump. (c): Photograph of the joints between the reservoir tube and the CF40 tube depicted from outside of the system (top) and the inside (bottom).	55
6.7	(a): Close up drawing of the MOT coil geometry. (b): Coordinate system indicating the x and z axes, along which the magnetic field simulation and measurement is shown. (c): Simulation and measurement of the magnetic field in the horizontal axis x . A measurement along the y axis, the horizontal axis perpendicular to x , shows minimal deviation, which arise from the bars connecting both coils to the power supply. This measurement is not shown here. (d): Simulation and measurement of the magnetic field in the vertical axis z . Simulation and measurement have been performed with a current of 800 A. Generally, simulation and measurement show good agreement, as the deviation is on the percent level of the gradient itself.	56
6.8	This figure shows the AC polarizabilities for the ground state in blue and the excited state in orange. The magic wavelength is around 410 nm, as the the polarizabilities for ground and excited states are equal.	58

List of Tables

2.1	Atomic mass [49], mass excess and abundance of the different Zn isotopes [50]. The mass excess gives the difference between the actual mass of the isotope with mass number i and $i \cdot 1$ u.	6
2.2	Coefficients for magnetic field-induced spectroscopy [10].	10
2.3	Second order clock laser-induced AC Stark shift coefficient $\kappa^{(1)}(\omega_c)$, fourth order lattice laser-induced AC Stark shift coefficient $\kappa^{(2)}(\omega_m)$ [60] and the sensitivity of the Rabi frequency to the clock- and lattice laser intensity for Zn and Sr.	11
2.4	Absolute and relative Blackbody radiation shifts, $\delta\nu_{\text{BBR}}$ and $\delta\nu_{\text{BBR}}/\nu_0$ for Zn [9], Sr [63, 65, 66] and Hg [67] at a temperature 300 K. For these numbers, the temperature is considered to be error-free.	12
4.1	Results of the 214 nm spectroscopy. All values are given in MHz unless stated otherwise.	35
5.1	Natural abundances for the bosonic isotopes of Ca in % [50].	37
5.2	Measured isotope shifts for the $(4s^2)^1S_0 \rightarrow (4s4p)^1P_1$ line in Ca in comparison to previously reported values. All values are in MHz.	42
5.3	Corrections and uncertainties of the isotope shift measurement, exemplified for ^{42}Ca . All values are in kHz.	43
6.1	Transitions from the 1S_0 state involved for the calculation of the magic wavelength in Zn.	57
6.2	Transitions from the 3P_0 state involved for the calculation of the magic wavelength in Zn. Experimental values from Ref. [172] are preferred over theoretical values from Refs. [173, 174].	58

Acknowledgements

I would like to thank Prof. Dr. Simon Stellmer for the opportunity to work in his group, starting an entirely new and fascinating research project, and I would like to express my deepest appreciation to the committee.

Furthermore, there are several people, who played a decisive role during my PhD time:

Special thanks go to Hans Keßler for his excellent scientific support, strong encouragement and for many practical improvements on the experiment. Additionally, I gratefully acknowledge the help of Wolfgang Alt and Frank Vewinger, who kept supporting me with their extensive knowledge and ideas, although they are engaged in different research groups. Without them, the completion of this dissertation would not have been possible.

I am deeply grateful to Sid Wright, Eduardo Padilla, Russell Thomas, Stefan Truppe and Gerard Meijer, for the opportunity of taking measurements with the buffer gas cooled beam source at the *Fritz-Haber-Institut*. This measurement campaign was very educational, instructive and encouraging for me. Furthermore, I want to thank Russell for a large number meetings and his visit in Bonn to support us on the degrading titanium-sapphire laser.

Furthermore, I would like to thank all students working on the zinc and calcium projects, namely Maya Büki, Marc Vöhringer, Lukas Möller, Frederik Wenger, and Andreas Reuß, for their help and assistance. Many thanks also go to the office mates, Markus Kirkines, Marcel Hohn, Maya Büki, Marc Vöhringer, Alireza Aghababei, Anica Hamer, Lara Becker, Frederik Wenger, Lukas Möller, Andreas Reuß, Christoph Biesek and Katrin Schatzmayr for shared breaks, candies and a lot more. Additionally, I want to thank all other group members, especially the PhD students (who were not mentioned yet), for their support over years, namely Thorsten Groh, Quentin Lavigne, and Jannik Zenner.

Furthermore, I would like to thank the workshop teams around Rolf Paulig and Walter Honerbach for sharing their experience on electronics and the teams around Alexander Christen and Daniel Poetes at the mechanical workshops for producing parts. I am grateful to the staff of the PI, most of them Norbert Jöpen, Beate Sund and Anja Leis.

Last but not least, special thanks go to my family and friends, who kept supporting me over the whole time.

Declaration of Authorship

I hereby declare that this thesis was formulated by myself and that no sources or tools other than those cited were used.

Bonn,

Date

.....

Signature